

Light Harvesting Methods in Photovoltaic Devices with Superficial Treatments

Ph. D Thesis of

Sourav Kanti Jana

(Matricola: 725205)

Under the supervisions of

Prof. Simona Binetti: Principal Supervisor

Prof. Dario Narducci: Co-Supervisor

Dr. Alessia Le Donne: Co-Supervisor

Prof. Gian Paolo Brivio: Dean of the Doctorate



Università degli Studi di Milano–Bicocca

Dipartimento di Scienza dei Materiali

(XXIV cycle: 2008-2011)

*Dedicated to
my Parents and Grand Ma*

Acknowledgements

This dissertation is a milestone of my life but would not have been possible without the support and contribution of a large number of people. I take this opportunity to thank everyone who stood by me and helped me through ups and downs.

First and foremost, it is a great pleasure to express my deepest sense of gratitude and indebtedness to my supervisors, Prof. Simona Binetti, Prof. Dario Narducci and Dr. Alessia Le Donne for their constant supervisions, inspirations and valuable suggestions during the course of the present thesis work. Thank you for giving me an opportunity to be part of your group, for believing in me and allowing me to venture into this work.

I am especially thankful to Prof. Dario Narducci for his helpful assistance during my first phase of my research work. Also without his cooperation, I could not get the opportunity to carry out the doctorate degree in this university.

I also want to convey my sincere regards to Prof. Gian Paolo Brivio, Dean of the Doctorate board of the Department of Material Science, University of Milano-Bicocca.

I would like to render my sincere regards to Prof. Sukumar Basu, Research Advisor of the Dept. of Electronics & Telecommunication Engineering, Jadavpur University, Kolkata, India for helping me to get the opportunity for the Doctorate degree in Italy. I am also happy to find him as a guide to carry out “project work in abroad” in his laboratory for six months.

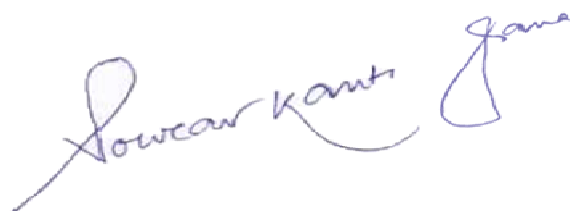
I convey my special thanks to Prof. Sangam Banerjee, Professor of Saha Institute of Nuclear Physics (SINP), Salt Lake, Kolkata, India for giving me the opportunity to access all the characterization facilities to full fill the “project work in abroad”. Also I am thankful to Bishnudas Ghosh, Research scholar of SINP for some help of experimental techniques during this period.

I take the opportunity to acknowledge Dr. Elisabetta Romano and Maurizio Crippa for giving me the preliminary idea about chemical synthesis. Also I would like to give special thanks to E. Romano for helping me to fulfill all the official formalities for settlement in Italy. I am also thankful to Prof. Maurizio Acciarri and Dr. Bruno for helping me scanning electron microscope analysis. Thanks also to the administration of our university.

I am also grateful to Pirelli Labs (CORIMOV) for their financial support.

Thanks are also due to my research colleagues, Manuel Moragno, Stefano Marchionna, Andrea Scaccabarozzi, Lorenzo Caccamo and Ekaterina Selezneva

I wish to pay my grateful respect to my beloved parents for their sacrifice, cooperation and continuous inspiration. Finally, I am thankful to my loving and caring wife Mrs. Barnita for her constant encouragement, understanding and perseverance for seeing me through this endeavour. Thank you.



*Sourav Kanti Jana
12th December, 2011
Milano, Italy*

List of Acronyms

PV	Photovoltaic
Si	Silicon
MC-Si	Multicrystalline Silicon
NP	Nanoparticle
SPRF	Surface Plasmon Resonance Frequency
PLS	Plasmonic Light Scattering
AM 1.5	Air Mass 1.5
EQE	External Quantum Efficiency
UV	Ultra Violet
NC	Nanocrystal
UV-VIS	Ultra Violet Visible Spectroscopy
SEM	Scanning Electron Microscopy
SR	Spectral Response
PL	Photoluminescence
TEM	Transmission Electron Microscopy
ARC	Anti Reflection Coating
NOARC	Without Anti Reflection Coating
CIGS	Copper Indium Gallium Selenide [Cu(In,Ga)Se ₂]
ME	Mercapto Ethanol
DMF	Dimethyl Formamide
ZnS	Zinc Sulfide
Mn	Manganese
PMMA	Poly-Methyl Methacrylate
EVA	Ethylene Vinyl Acetate

Contents

Chapter1: Introduction

<i>1.1 Alternative sources of energy</i>	15
<i>1.2 Generations of solar cells</i>	18
<i>1.2.1 First generation solar cells</i>	18
<i>1.2.2 Second generation solar cells</i>	19
<i>1.2.3 Third generation solar cells</i>	21

Chapter 2: Light harvesting methods in silicon solar devices: literature reviews

<i>2.1 Limitation of first generation PV devices</i>	25
<i>2.2 A few approaches for enhancement of solar cell efficiency</i>	25
<i>2.2.1 Surface Plasmon effect</i>	25
<i>2.2.1.1 Mechanism of light trapping inside the Si solar cell</i>	26
<i>2.2.1.2 Effect of particle size and shape on the light trapping mechanism</i>	28
<i>2.2.2 Spectrum modification method</i>	29
<i>2.2.2.1 Down-conversion and down-shifting</i>	29
<i>2.2.2.2 UP-conversion</i>	33
<i>2.2.3 Carrier multiplication method</i>	35

Chapter 3: Experimental Techniques

<i>3.1 Thermal evaporation</i>	41
<i>3.2 UV-VIS measurement</i>	42
<i>3.3 Reflectance measurement</i>	44
<i>3.4 Scanning Electron Microscope and Transmission Electron Microscope</i>	44
<i>3.5 Spectral response system</i>	45

3.6 I-V measurements of solar cell.....	47
3.7 Photoluminescence measurement.....	48

Chapter 4: Light scattering effect by metal NPs: experimental results

4.1 Introduction.....	53
4.2 Experimental.....	54
4.2.1 Deposition of silver and gold films on glass substrate by thermal evaporation and sputtering.....	54
4.2.2 Preparation of colloidal silver NPs using surfactant: Method A.....	55
4.2.2.1 Preparation of silver NPs coated substrates.....	56
4.2.2.2 Deposition process of the silver NPs (prepared with Method A) on Si solar cells.....	57
4.2.3 Preparation of silver NPs using polymer as a stabilizer: Method B.....	57
4.2.4 Gold NPs synthesis by colloidal method.....	57
4.2.5 Deposition process of colloidal silver and gold NPs (prepared by Method B) on various substrates.....	58
4.2.6 Light irradiation for removal of B-O complexes from Si solar cells.....	58
4.3 Results and discussions	
4.3.1 Results on NPs (silver and gold) prepared by physical deposition (thermal evaporation and RF sputtering) method.....	59
4.3.2 Results on colloidal silver NPs prepared with Method A	
4.3.2.1 UV-Vis study.....	62
4.3.2.1.1 Change of AgNO ₃ concentration.....	62
4.3.2.1.2 Effect of centrifugation.....	63
4.3.2.1.3 Effect of PDDA matrix.....	64

4.3.2.1.4	<i>Change in concentration of surfactant.....</i>	<i>64</i>
4.3.2.2	<i>SEM analysis of silver NPs deposited on Si substrate.....</i>	<i>65</i>
4.3.2.3	<i>Spectral Response measurements of Si solar cells with and without silver NPs prepared with Method A.....</i>	<i>66</i>
4.3.3	<i>Results on colloidal silver NPs prepared with Method B</i>	
4.3.3.1	<i>UV-VIS results of silver NPs embedded in polymer.....</i>	<i>68</i>
4.3.3.2	<i>SEM analysis of PDDA embedded colloidal silver NPs</i>	<i>69</i>
4.3.3.3	<i>Spectral response of different Si solar cells with and without silver NPs prepared with method B.....</i>	<i>70</i>
4.3.3.4	<i>I-V results of different cells with and without silver NPs prepared with Method B.....</i>	<i>71</i>
4.3.3.5	<i>Reflectance measurement of bare Si substrate coated with and without silver NPs prepared with Method B.....</i>	<i>73</i>
4.3.4	<i>Results on gold NPs prepared in colloidal solution method</i>	
4.3.4.1	<i>Transmittance measurement of colloidal gold particle solution... </i>	<i>74</i>
4.3.4.2	<i>SEM analysis of colloidal gold particle deposited on Si substrate.....</i>	<i>74</i>
4.3.4.3	<i>Spectral response analysis of NOARC cells coated with and without gold NPs.....</i>	<i>75</i>
4.3.4.4	<i>I-V measurements on NOARC cell with and without gold NPs....</i>	<i>77</i>
4.3.5	<i>Impact of oxidation on the device performance.....</i>	<i>79</i>
4.3.6	<i>Investigation of light scattering effect due to metal NPs on CIGS thin film solar cells.....</i>	<i>80</i>

4.3.6.1 Principle of operation of CIGS solar cells	80
4.3.6.2 Deposition of colloidal NPs (both silver and gold) on CIGS solar cells.....	81
4.3.6.3 Spectral response of CIGS cells with and without NPs (both silver and gold).....	82

Chapter 5: Down Shifting Effect by Semiconductor NCs on Si solar cells

5.1 Introduction.....	87
5.2 Experimental.....	88
5.2.1 Preparation method of ZnS NCs.....	89
5.2.2 Preparation method of Mn doped ZnS NCs.....	90
5.2.3 Deposition method of doped ZnS NCs on Si solar cells.....	90
5.2.4 Preparation method of NC doped polymer composite film.....	90
5.3 Results and discussion.....	91
5.3.1 UV-VIS absorption analysis of both pure and Mn doped ZnS NCs.....	91
5.3.2 TEM and EDX analysis of both pure and Mn doped ZnS NCs.....	93
5.3.3 Photoluminescence analysis of both pure and Mn doped ZnS NCs.....	98
5.3.4 Spectral response analysis of NCs coated Si solar cell.....	101
5.3.5 I-V measurements of NCs coated Si solar cell.....	104
5.3.6 Spectral response analysis of Si solar cell with pure PMMA film on top.....	105
5.3.7 Spectral response of Si solar cell with NCs doped PMMA and EVA film on top.....	106

<i>Chapter 6: Conclusions, Critical Issues and Future Work</i>	109
<i>References</i>	115
<i>List of publications</i>	120

Chapter 1

Solar Energy and Solar Devices: An overview

Introduction

1.1 Alternative Sources of Energy

Sun provides enormous amounts of energy powering oceans, atmospheric currents, and cycle of evaporation and drives river flow, hurricanes and tornadoes that destroy natural landscape. The San Francisco earthquake of 1906, with magnitude 7.8, released an estimated 10^{17} joules of energy which sun delivers in one second. Earth's resource of oil mounts up to 3 trillion barrels containing 1.7×10^{22} joules of energy that the sun supplies in 1.5 days. Humans annually use about 4.6×10^{20} joules annually which sun supplies in one hour. The sun continuously supplies about 1.2×10^{25} terawatts of energy which is very much greater than any other renewable or non renewable sources of energy can provide. This energy is much greater than the energy required by human beings which is about 13 terawatts. By covering 0.16% of Earth's land with 10% efficient solar cells would provide 20 Terawatts of energy about twice of fossil fuel consumption of the world including numerous nuclear fission reactors [1].

Nowadays, there is much talk in the popular news media as well as in technical journals about energy supply and climate change. Electricity is the most versatile form of energy we have. It is what allows citizens of the developed countries to have nearly universal lighting on demand, refrigeration, hygiene, interior climate control in their homes, businesses and schools, and widespread access to various electronic and electromagnetic media. Access to and consumption of electricity is closely correlated with quality of life. Figure 1.1 shows the Human Development Index (HDI) for over 60 countries, which includes over 90% of the Earth's population, versus the annual per capita electricity use [2]. The HDI is compiled by the United Nation and calculated on the basis of life expectancy, educational achievement, and per capita Gross Domestic Product. Improving the quality of life in many countries, as measured by their HDI, will require increasing their electricity consumption by factors of 10 or more, from a few hundred to a few thousand kilowatt-hrs (kWh) per year. How will we do it? Our choices are to continue applying the answers of the last century such as burning more fossil fuels (and releasing megatons of CO_2 , SO_2 , and NO_2) or building more nuclear plants (despite having no method of safely disposing of the high-level radioactive waste) or to apply the new millennium's answer of renewable, sustainable, nonpolluting, widely available clean energy like photovoltaics and wind. (Wind plants presently generate over a thousand times more electricity than photovoltaics but it is very site-specific, whereas photovoltaics is generally applicable to any location.)

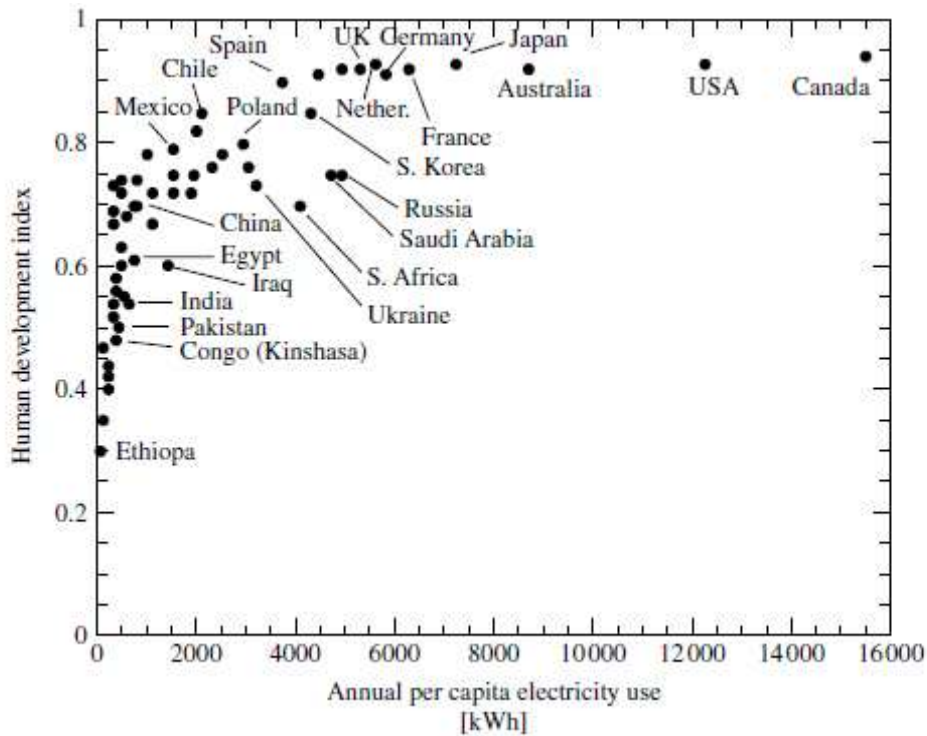


Figure 1.1: Human development index (HDI) vs. per capita kWh usage [2]

Solar energy is in abundance but up to now only a little is used for power human activities. About 80%-85% of our total energy comes from fossil fuels. These resources are non renewable, fast depleting, produce greenhouse gases and other harmful environmental pollutants [3]. Fossil fuels emit a large volume of green house gas like CO₂ into the atmosphere and disturb the ecological balance. These emissions have been increasing due to overutilization of fuels to meet the ever expanding needs of human society. The solutions for this problem are to use fossil fuels in conjunction with carbon sequestration, nuclear power and solar power. Carbon sequestration is an extremely difficult method since a large volume of space is required to store the emitted green house gases and its maintenance is a very crucial issue. Nuclear power seems to be a good option but the feasibility of deploying several thousands of 1Gigawatt power plants all over the world to meet the 10Tera watt demand of the society is sceptical. The Uranium resource for these power plants on earth also gets exhausted in coming years. On the other hand shifting the focus on renewable sources of energy is the ideal choice and solar power is by far the most prominent energy source owing to its versatility, inexhaustible and environmental friendly features [1].

Solar cells represent the fundamental power conversion unit of photovoltaic (PV) system. Up to now, many of them are made from semiconductors and for practical operation solar cells are usually assembled into modules. Many different solar cells are now available on the market, and yet more are under development. The burgeoning solar cell market is maturing to become a very profitable

investment to industries resulting in an annual growth of 41% in the last five years as shown in Figure 1.2 [4]. The range of solar cells spans different materials and different structures developed to extract maximum power from the device while keeping the cost to a minimum. The photovoltaic industry is a rapidly growing business which involves a great deal of research both in the industrial and academic level. Academic research is a key factor in developing applications for domestic enterprises, so that they would be able to compete in international markets.

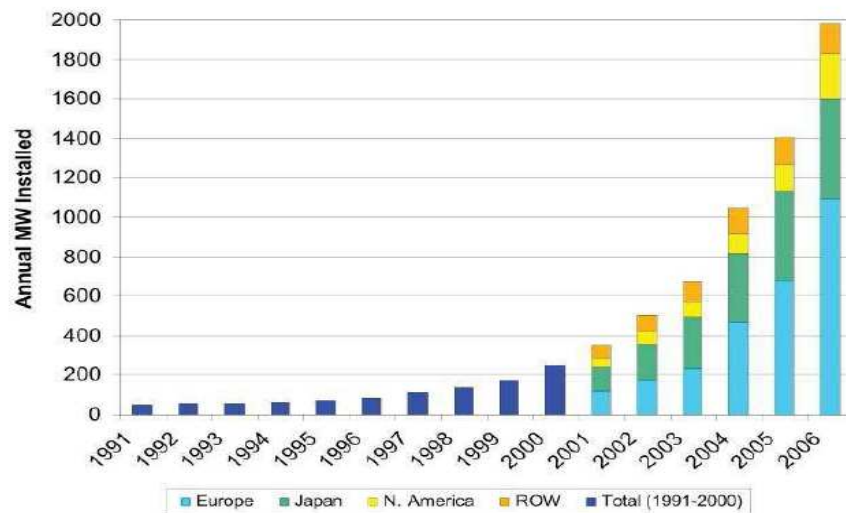


Figure 1.2 Global PV Installations by Year [5]

PVs are favoured for many applications because they are modular and can thus be deployed at arbitrarily small or large scales and in particular are well-suited to rooftop deployment (as opposed to solar thermodynamic which requires large-scale deployment), and because of their relatively high efficiency and long-term (30 year) stability (as opposed to photoelectrochemical cells which at the time of writing are limited to lower efficiencies and suffer from stability issues). The PV industry has been growing rapidly, especially in recent years, due primarily to aggressive government-fostered market growth in Japan, Germany and, more recently, Spain and Italy. PVs are nearing cost-competitiveness with other sources of electricity, [5,6] and the drive continues to reduce the cost per kilowatt-hour to increase the adoption of PVs. Silicon (Si) is by far the most popular material choice in the terrestrial PVs market at the time of writing [5,6]. There are several reasons behind it. Firstly, Si is most industrially studied material [7]. Secondly, Si is the most abundant solid element on Earth, [8] and, at least in principle, it is cheap. Thirdly, by using Si the PV industry has been able to follow in the footsteps of the microelectronics industry, exploiting the wealth of knowledge that has grown up around this element. Furthermore, Si is nontoxic. There are two broad approaches for reducing the cost per unit electrical energy generated by Si solar cell modules. Firstly, one can aim to increase the efficiency of the product, usually by pursuing new cell designs

that can take full advantage of high-quality absorber material. Secondly, one can pursue cost reductions while maintaining the efficiency of the product, often done by exploring novel manufacturing approaches but also sometimes with new cell designs and perhaps by exploiting lower-quality, cheaper materials. There is good reason to believe that the record Si cell efficiency for unconcentrated sunlight, of 24.7%, set by UNSW in 1999, [9] will not be significantly exceeded [10]. Furthermore, Sun Power Corporation has recently announced a cell produced on an industrial pilot line with an efficiency of 23.4% [9]. Thus, in the case of Si, most research efforts have fallen into the second category, i.e., pursuing designs that approach this efficiency but that are more cost-effective at the manufacturing level. To reduce the cost, these cells are now often made from multicrystalline (MC) material, rather than from the more expensive single crystals [11]. The high manufacturing costs of the single crystalline silicon solar cells prevent them from breaking through in the energy markets. The thin-film silicon solar cells [12, 13] are cheaper to manufacture, but their efficiencies are low compared to those achieved with crystalline silicon wafer based cells [14]. Therefore, the trend in the photovoltaic research is to reach for even higher efficiencies and less material consuming cell designs.

High costs and conversion efficiency have been the major bottlenecks in the potential of solar power becoming a primary source of energy. Nowadays major research done with the aim of improving the efficiency of these cells has brought this dream closer to reality. New methods of harvesting the full spectrum of the sun emission, multijunction solar cells (homojunctions and heterojunctions), and new low cost materials are the way paving way for solar power to be the emerging power resource for the world in the next future.

1.2 Generations of solar cells

Solar cells are usually classified into three generations based on the order of their prominence. Research is being conducted on all the three generations concurrently to improve their efficiencies. In Figure 1.3, the record efficiency of all types of solar cells is reported.

1.2.1 First generation solar cells

The first generation of solar cells can be considered high-cost, high-efficiency and it is based on Si. The manufacturing processes that are used to produce first generation cells are inherently expensive, meaning that these cells may take years to pay for their purchasing costs. It is not thought that first generation cells will be able to provide energy more cost effective than fossil fuel sources. Reduction in production costs of this technology is nullified owing to high energy and labour costs, material costs mostly for the silicon wafer, strengthened low-iron glass cover sheet and

costs of other encapsulant materials. Recently, there is news for further improvement of first generation solar cell's efficiency.

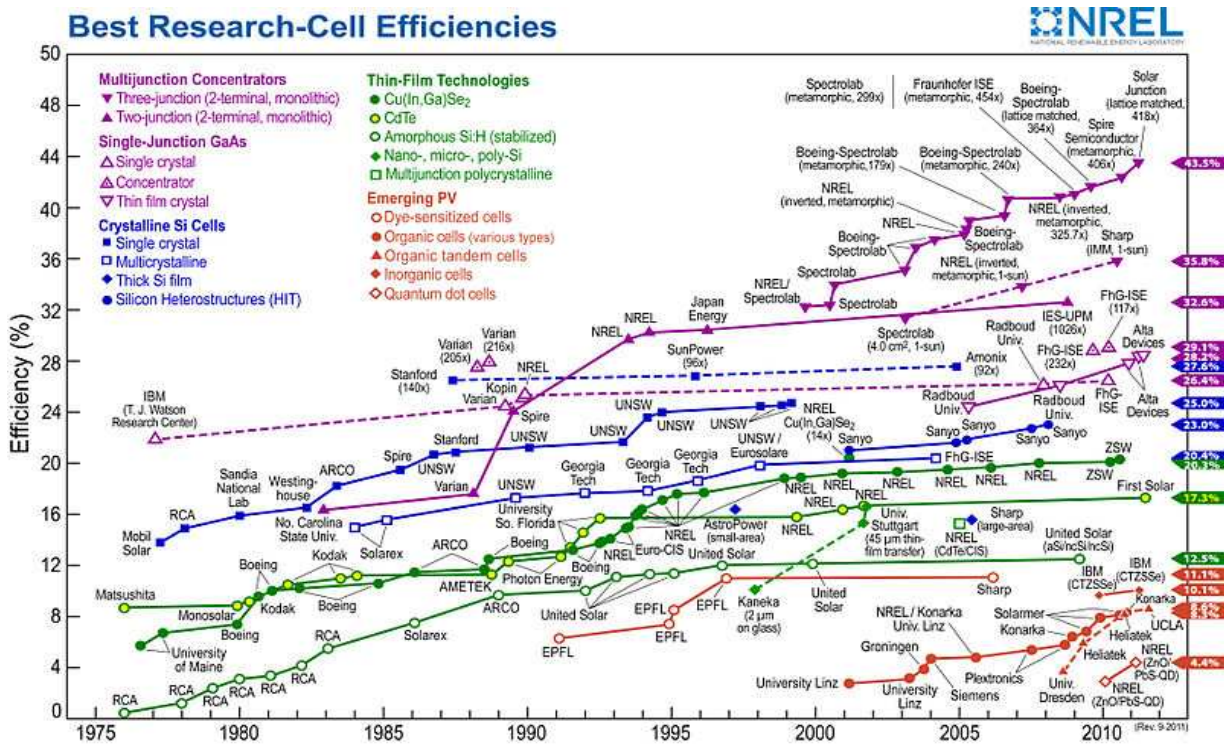


Figure 1.3: Best Research Cell Efficiencies [15]

Different industry like Sanyo tries to develop their technology for enhancement of existing efficiency of crystalline silicon (C-Si) based PV cells. Among them recently, DuPont presented its technology roadmap for PV metallization technology at the 25th European Photovoltaic Solar Energy Conference (EU PVSEC). DuPont Microcircuit Materials has developed a roadmap of proposed technology options to help enable conversion efficiency beyond 20% by 2012. Material and process technology improvements are made to the DuPont Solamet brand photovoltaic metallization pastes. Innovative PV metallization materials and new cell structures can be combined to maximize solar cell efficiency. DuPont recently introduced Solamet PV16x series front side silver paste system, which increases efficiency by up to 0.4% [16].

1.2.2 Second generation solar cells

To address the problems of energy requirements and production costs of solar cells a switch from ‘first generation’ to ‘second generation’ of thin-film cell technology has been done. By eliminating the silicon wafer a major reduction in material costs have been possible in the thin-film technology.

The second generation of solar cells, which has been under intense development for the 90s and early 2000s, are low-cost but quite lower efficiency than Si solar cell. The cell design based on thin film materials requires minimal absorber thickness and cheap manufacturing processes. The most popular materials used for second generation solar cells are amorphous silicon, cadmium telluride (CdTe), copper indium gallium selenide (CIGS), and micromorphous silicon. These types of solar cells are able to be produced at low cost by depositing the active material on low cost substrates such as glass, ceramics, metal foil, plastic etc. A trend towards shifting to second generation from first generation is showing up but the commercialization of this technology has proven to be difficult [17]. Fortunately with the development of new materials over the coming decades the future of thin-film technology seems to be promising with higher efficiency.

A comparison between the record efficiency of first and second generation of solar cells is reported in Figure 1.4. Recently, scientists (at the Centre for Solar Energy and Hydrogen Research, ZSW, Germany) have achieved a new success increasing solar cells electricity yield. The Stuttgart researchers produced thin-film solar cells with a top efficiency of 20.3% [18]. With this performance, they exceed their own world record and minimize to only 0.1 percent the advance of the MC solar cells still dominating the market. The new record-breaking solar cells from ZSW are made of extremely thin layers of copper, indium, gallium, and selenide (CIGS).

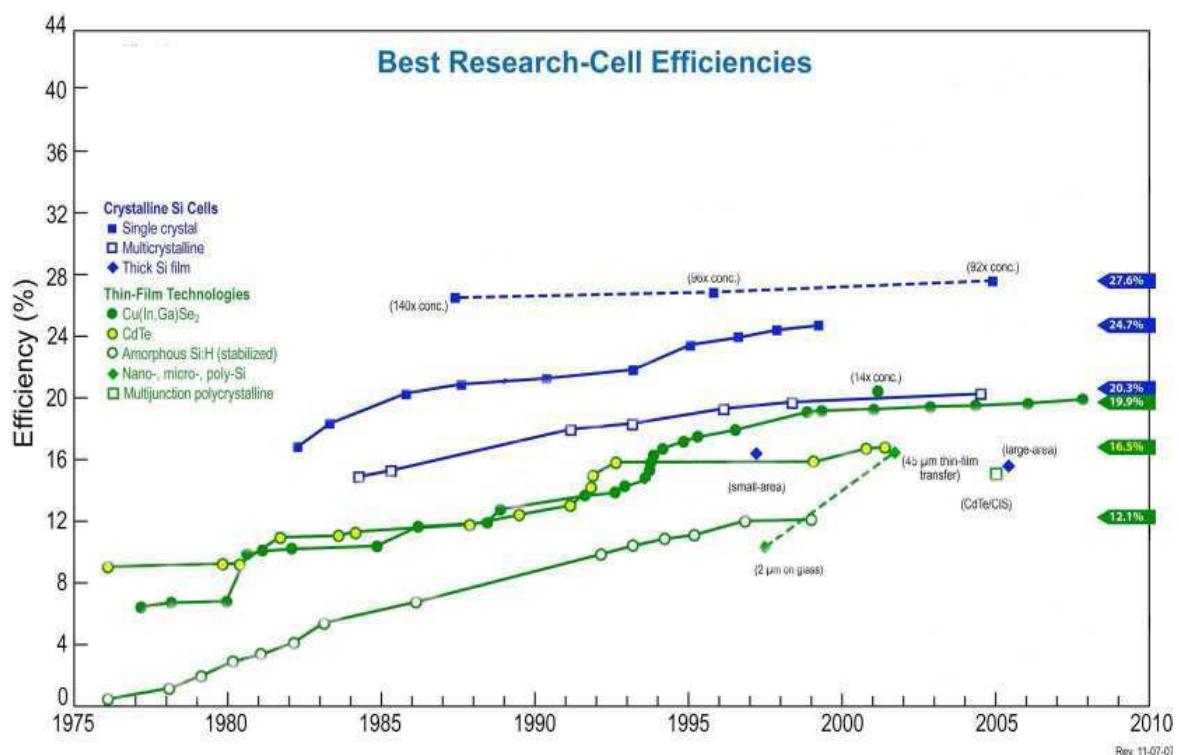


Figure 1.4: First and second generation solar cell efficiencies [16]

1.2.3 Third generation solar cells

Third generation solar cells are mostly based on the multi junction cells (MJC). The MJC allows absorption of a wider range of wavelengths in the solar spectrum by combining solar cells of varying bandgap in a series (tandem) stack. Third generation solar cells can exceed the theoretical solar conversion efficiency limit for a single energy threshold material. The threshold was calculated in 1961 by Shockley and Queisser as 31% under 1 sun illumination. The theoretical efficiency for four junctions is 71% [19].

The only high efficiency solar cell concept that has been shown experimentally to work, with a 3-junction device is based on III-V semiconductor [20]. The typical structure for such cells is a multi-layer epitaxial thin film stack grown on a germanium substrate with tunnel junctions in between to match the currents between each band gap cells. At present these cells are expensive ($> \$7W_p^{-1}$) and used in space applications, as well as terrestrial concentrator systems in solar power stations in which small cell area is sufficient [19].

The third generation is also included non-semiconductor technologies (including polymer cells), quantum dot, intermediate band solar cell [21], hot carrier solar cells, up conversion and down conversion technology, and solar thermal technologies, such as thermophotonics [22].

Chapter 2

Light Harvesting Methods in Silicon Solar Devices: Literature Reviews

2.1 Limitations of first generation PV devices

There are three losses in a silicon solar cell. The first of these is thermalization, which occurs when an electron-hole pair with energy greater than the band gap of silicon ($E=1.12$ eV, $\lambda = 1100$ nm) is created and the excess energy is lost as heat because the electron (and hole) relax to the conduction (and valence) band edges. The second loss mechanism is due to recombination which is an opposite process to carrier generation. Recombination is most common at impurities or defects of the crystal structure, or at the surface of the semiconductor where energy levels may be introduced inside the energy gap. These levels act as trapping sites for the electrons to fall back into the valence band and recombine with holes. Important sites of recombination are also ohmic metal contacts. The third loss mechanism is transmission, which occurs because photons with energy less than the band gap of silicon are not absorbed [23].

2.2 A few approaches for enhancement of solar cell efficiency

The limiting efficiency in silicon solar cell can be improved by metal nanoparticle (plasmonic effect) [24], spectrum modification [25], carrier multiplication method [26]. The details of each method are briefly discussed in the following sections.

2.2.1 Surface Plasmon effect

Light trapping is an attractive way for achieving higher efficiency in both bulk Si solar cell as well as thin film solar cell. Plasmonics is a recent approach where both absorption and scattering by metal nanoparticles (NPs) can be used to obtain light trapping in both thin film and bulk Si solar cell.

Pioneering work in the area of plasmonic enhancement of light-sensitive devices was done by Stuart and Hall, who showed that an enhancement in the photocurrent of factor 18 could be achieved for 165nm thick Silicon-on-Insulator (SOI) photo-detector at 800 nm using silver nanoparticles on the surface of the device [24]. Subsequently Schaadt et al. deposited gold nanoparticles on highly doped wafer based solar cells, obtaining enhancements of up to 80% at wavelength around 500 nm [27]. Derkacs et al. [28] used Au nanoparticles on thin film amorphous silicon solar cells to achieve an 8% relative increase in conversion efficiency. Recently, Pillai et al. deposited silver particles on 1.25 μm thick SOI structured solar cells and planar wafer based cells, and achieved relative photocurrent increases of 33% and 19 % respectively [24]. Pillai et al. [29] have reported an overall electroluminescence enhancement of a factor of 7 for thin film SOI light

emitting diodes. Surface plasmon resonance based antireflection coating on GaAs solar cells was also tested and reduction of reflection in the UV region was observed [30].

2.2.1.1 Mechanism of light trapping inside the Si solar cell

In recent years, the electromagnetic properties of metal NPs have been renewed interest in the photonic devices research and development. Localized surface plasmons are collective oscillations of the conduction electrons in metal particles. Movement of the conduction electrons upon excitation with incident light leads to build up of polarization charges on the particle surface. This acts as restoring forces, allowing a resonance to occur at a particular frequency, which is termed as Surface Plasmon Resonance Frequency (SRPF). Incident light in the region of the resonance wavelength of the particles is strongly scattered or absorbed, depending on the size of the particles. The extinction of the particles is defined as the sum of the scattering and absorption [31-34]. Two main basic mechanisms have been proposed to explain photocurrent enhancement by metal nanoparticles incorporated into or on the front surfaces of the solar cells: near field concentration of light and light scattering method. When metal NPs are excited by an electromagnetic wave (both in the visible and infrared regions), they exhibit collective oscillations of their conduction electrons. These electrons give rise to an electric field on the NP surface and the amplitude of this field is enhanced in the case of closely spaced NPs. This effect is known as near-field concentration of light and the corresponding photocurrent enhancement is more pronounced when the metal NPs are embedded inside the active layer of the device, as in the case of organic cells [34]. The near field effect is not a relevant process to the standard p-n junction Si solar cell, in which junction typically lies 0.2-1 μm below the surface.

A further mechanism which has been explored over the past few years is the light scattering by metal NPs excited at their SPRF, known as Plasmonic Light Scattering (PLS) [32-36]. Incoming light at SPRF will scatter or absorb depending upon the size of the particle and the refractive index of the surrounding medium [35]. The scattering efficiency, or radiative efficiency, [36] is defined in fact as $C_{sc}/(C_{sc} + C_{ab})$, where C_{sc} is the scattering cross-section and C_{ab} the absorption cross-section of metal particles [24]. It is therefore apparent that the scattering efficiency is strongly dependent on the particle size.

Furthermore, Kirkengen and Bergli [35] described above PLS and near field method in more detailed way. The energy of localized surface plasmons on metal NPs can create electron-hole pairs in silicon solar cells through two processes, which they called indirect absorption and direct absorption.

In indirect absorption, the energy of a Plasmon is emitted by radiative electromagnetic fields (light) in directions along the semiconductor, increasing the effective optical path of the photons and thus increasing the probability of optical absorption. This is also known as PLS method. A coupling geometry is shown in Figure 2.1.

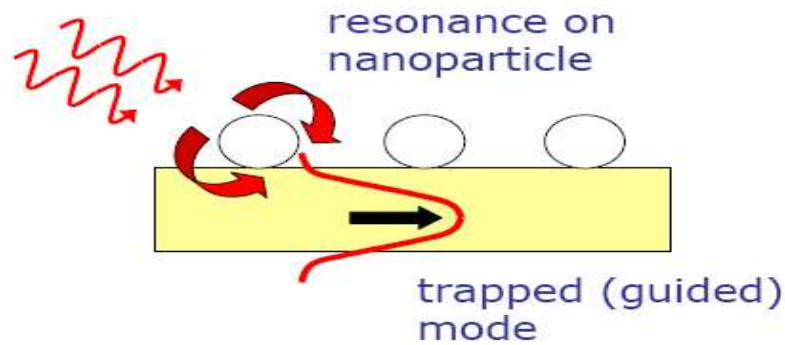


Figure 2.1: Light coupling geometry into the near waveguide due to metal NPs [36, 37]

Light trapping must be viewed as the process of coupling the incident light into view discrete waveguide modes of the structure [36-37]. In the above figure the metal NPs can be thought of as microscopic antennas, collecting the incident radiation and then transferring the energy into the nearby waveguide, where it is trapped in guided modes propagating in all directions parallel to the waveguide surface. This can lead to longer optical path lengths within the waveguide, producing enhanced absorption.

In the direct absorption the near field of the Plasmon excites electron-hole pairs into the semiconductor, and the conservation momentum is preserved through a transfer of momentum to the metal particle. The two mechanisms are depicted in Figure 2.2.

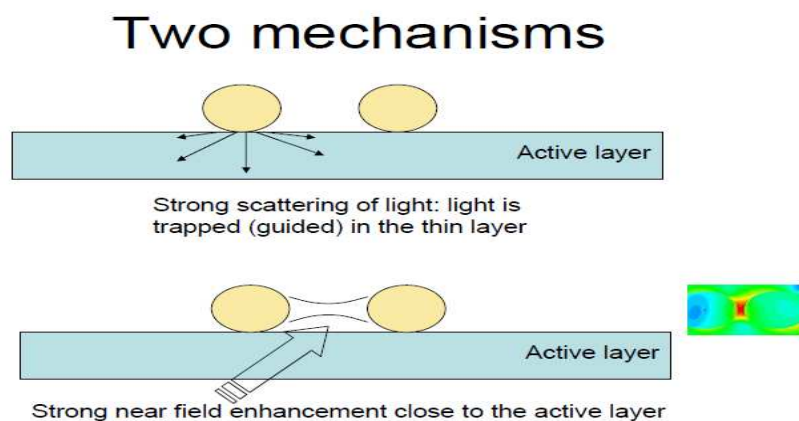


Figure 2.2: How light can couple with active layer of solar devices [34]

2.2.1.2 Effect of particle size and shape on the light trapping mechanism

Scattering and absorption depend on the size of the particles. Metallic particles that are much smaller than the wavelength of light tend to absorb more and absorption dominates over scattering. However, as the size of the particles increases, scattering process dominates and we take advantage of this property for our application of light trapping. Beyond certain limits, however, increasing the particle size leads to increased retardation effects and higher order multipole excitation modes, which decrease the efficiency of the scattering process [29]. Increasing the particle size produces an increase in the magnitude of photocurrent enhancement, even if the change in the particle size does not change the surface plasmon resonance wavelength. Intuitively, this could be explained with increasing the radiative efficiency and scattering cross sections, as particle size become larger [37]. Particle shape also plays an important role in the effect of metal NPs on a photovoltaic device. Particle shapes such as disk that have a large fraction of their volume close to the semiconductor lead to a very high fraction of light scattered into the substrate [38].

Theoretical predictions of the surface Plasmon resonance peak were made using Mie calculations. Mie theory describes the scattering of light by particles. Particles are defined in a region with refractive index (n_p) that differs from the refractive index of its surroundings (n_{med}) and n_r , mismatch between refractive indexes of particle and medium. Mie classical solution is described in terms of two parameters, n_r and x :

$$n_r = \frac{n_p}{n_{med}},$$

Surface refractive index mismatch is expressed as a size parameter x :

$$x = \frac{2\pi r n_{med}}{\lambda}$$

According to the Mie theory calculation, efficiency of scattering is expressed this way:

$$\sigma_s = Q_s A ,$$

Where, Q_s is the scattering coefficient and A is the true geometrical cross-sectional area of the spherical particle.

Scattering and extinction coefficients are expressed by:

$$Q_s = \frac{2}{x^2} \sum_{n=1}^{\infty} (2n + 1)(|a_n|^2 + |b_n|^2);$$

$$Q_{ext} = \frac{2}{x^2} \sum_{n=1}^{\infty} (2n + 1)R(a_n + b_n),$$

Where a_n and b_n are Mie coefficients, which may be complex. R is the diameter of the particles. The expressions of these coefficients are discussed further in the literature [39].

In general, light absorption dominates in the extinction (extinction = absorption + scattering) spectrum for particles relatively small radius, and light scattering becomes the dominant process for larger particles [40].

2.2.2 Spectrum modification method

Spectrum modification is a well researched topic in physics and in chemistry and has been applied to photonic devices [25]. Three losses in silicon solar cell can be reduced by spectrum conversion from higher energy to lower energy and vice versa. There are two possibilities to use the high energy part of the solar spectrum more efficiently: down-conversion, down shifting and photoluminescence.

2.2.2.1 Down-conversion and down- shifting

Thermalization losses can be reduced by using **down conversion** and **down shifting** method. The down-conversion of incident photons into two or more photons with lower energies can be achieved, in principle, with every three-level system. The absorption of a high-energy photon leads to an electronic transition from the lowest level to the highest excited level. A two-step recombination of the electron to the lowest level via the intermediate level is accompanied by the emission of two lower energy photons, if both steps are radiatively efficient. This is shown in Figure 2.3. A schematic representation of proposed system of a solar cell in combination with a down-converter is shown in Figure 2.4.

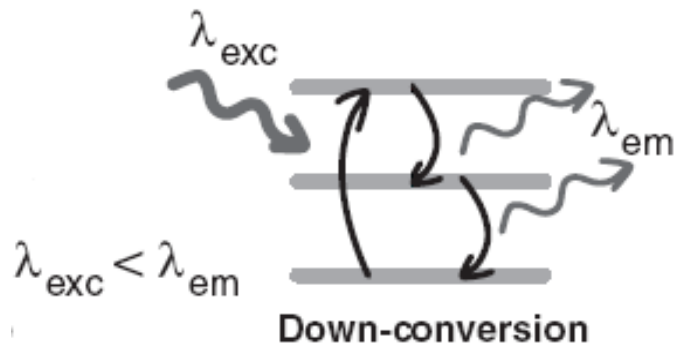


Figure 2.3: Down-conversion mechanism [25]

In the down shifting process, a single high-energy photon is converted into a single lower-energy photon. So the two techniques down conversion and down-shifting are distinguished by their quantum efficiencies. For down-shifting, the quantum efficiency is always less than or equal to one, whereas for down-conversion the quantum efficiency exceeds one (more than one photon is emitted for each incoming photon) provided non-radiative losses can be prevented [25].

A luminescence converter that, in an ideal case, converts high-energy photons into two or more lower energy photons is located on the front surface of a conventional single junction solar cell. The luminescence converter is electronically isolated from the solar cell, i.e., the coupling between the converter and the solar cell is purely radiative. The absorption of the two or more low-energy photons emitted by the converter leads to the generation of *electron-hole pairs* (e-h pair) in the solar cell, which means that more than one *e - h* pair is generated in the solar cell per incident high-energy photon.

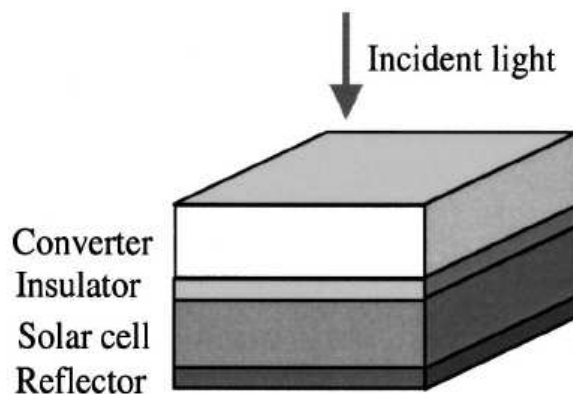


Figure 2.4: Schematic diagram of the down-conversion system. The luminescence converter is located on the front surface of a solar cell

In order to avoid the absorption of the high-energy photons and the subsequent thermalization of $e - h$ pairs inside the solar cell, a bifacial solar cell is needed and additionally the solar cell material must be transparent for high-energy photons in this geometry, a condition that rules out all semiconductor materials used for solar cells. In a different geometry the luminescence converter could also be located on the rear surface of the solar cell. An energy diagram for the down-conversion system is shown in Figure 2.5. Sunlight is incident from the left side in that representation, if the converter is located on the rear surface. If the luminescence converter is located on the rear surface, photons with energies larger than twice the band gap shall be transmitted by the solar cell and absorbed by the converter. This can be achieved by restricting the widths of the bands of the solar cell material as shown in Figure 2.5. The incident sunlight comes from the left, as shown. The down-converter consists of a material with a band gap E_g , converter that contains impurity levels (IL) with energy E_1 above the valence band edge. Radiative transitions take place between the valence band and the conduction band (solid arrow) or between one of the bands and the impurity level (dotted arrows). In an ideal case the IL lies in the center of the band gap of the converter and both intermediate transition have energy thresholds for the absorption that are equal to the band-gap energy of the solar cell, i.e., $E_1=E_2=E_g$. In the geometry with the converter on the rear surface the widths of the bands in the solar cell must be restricted to avoid the absorption of the high-energy photons with $h\nu > 2E_g$, which shall be absorbed and down converted in the luminescence converter [41]. Emission of photons with energies larger than the band gap of the solar cell via the intermediate transitions inside the luminescence converter represents an energy loss. Therefore, in an idealized case, the energy thresholds E_1 and E_2 for the two intermediate transitions both equal the band-gap energy of the solar cell, i.e., $E_1=E_2=E_g$. The intermediate level thus lies in the middle of the band gap of the converter.

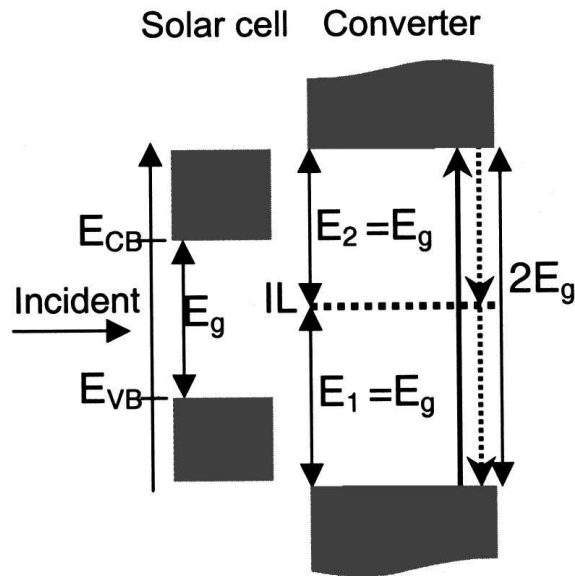


Figure 2.5: Schematic energy diagram of a solar cell in combination with a down-converter, if the converter is located on the rear surface of the solar cell [41]

In both geometries a reflector is located on the rear surface of the system. A theoretical model described [41] that the limiting efficiency was found for the geometry with the converter located on the rear surface. We only present the results of our experiments for the geometry with the converter located on the front surface. In practice, much research on luminescence down conversion with external quantum efficiency (EQE) of less than unity has been performed for shifting the shorter wavelength to longer ones. The application of down shifting layers in photovoltaic module is as luminescent solar concentrators [42-45].

Rare-earth doped luminescent materials are extensively used in the lighting industry [46]. The motivation using for using rare earths is that this family elements luminescence over a wide range, from the near- infrared, through the visible to the ultraviolet. An overview of available down converters is indicated in the literature [25, 44]. Among them rare earth organic complexes constituted by an excitation harvesting ligand attached to an emitting ion (Tb^{3+} , Eu^{3+} , Er^{3+}) have been subject of much research since the first demonstrations of their reliability as active layer in VIS and NIR organic light emitting diodes [47-48]. These molecular systems strongly absorbing in the UV and possessing a consistent Stokes shift of their emission towards the region maximum conversion efficiency of photovoltaic devices. In particular the main emission of Eu^{3+} complexes at 614nm is really close to maximum efficiency of the crystalline silicon which lies at about 600 nm. The use of Tb^{3+} complexes is more appropriate in the case of amorphous silicon cells where the maximum efficiency is about at 500 nm. Low temperature encapsulation of a solar cell with a

coating doped with light harvesting complex is supposed to allow an improvement of quantum efficiency of a commercial photovoltaic system without modification of the industrial process.

A quantum efficiency enhancement associated with the light harvesting and energy transfer properties of the $[\text{Eu}(\text{phen})_2](\text{NO}_3)_3$ complex (Europium (III)-bis-phenanthroline-tris-nitrate) was demonstrated in mono-crystalline silicon solar cell [49]. PVA was used as polymeric matrix in this case. They showed an overall increase of the delivered power 0.8-1% under AM0 (space applications) conditions. A more recent paper by McIntosh *et al.* [50] deals instead with down-shifting encapsulating layers consisting of PMMA (polymethylmethacrylate) doped with organic dyes. Previously one our group [51] used a bilayer structure consisting of poly-vinylacetate (PVA) doped with tris(dibenzoyl methane) (monophenanthroline) europium(III) and tris[3-(trifluoromethylhydroxymethylene)-d-camphorate] europium (III) on commercially available crystalline silicon solar cells. It was observed a relative enhancement of 2.8% of the total delivered power by the cells. Photoluminescence Excitation (PLE) investigations carried out on such organic complexes showed concentrations quenching effects [49, 51]. Best results were obtained in cells coated with lower concentrations (0.0015% wt) of organic complexes. Also reduction of peak wattage (W_p) price ($\text{€}/W_p$) was calculated for crystalline silicon photovoltaic modules. Industrial photovoltaic module fabrication process is based on a copolymer of vinylacetate and ethylene (EVA), whose optical properties are comparable with those of PVA. Therefore, EVA doped with proper choice of organic complex is a good candidate of polymeric matrix on silicon cell in such down- shifting process. It should be remarked that such a doping procedure of the encapsulating matrix does not affect the industrial process leading to the fabrication of the standard commercial PV module. In recent work [52], EVA doped with $\text{Eu}(\text{tfc})_3$ (tris[3-(trifluoromethylhydroxymethylene)-d-camphorate] europium (III)) and 4,4'-bis(diethylamino) benzophenone (or EABP) was deposited on silicon cells and obtained 3% relative enhancement of the maximum delivered power in lab PV module. Such complex is able to absorb Ultra Violet (UV) as well as visible light due to the presence of a new absorption band probably related to a bathochromic shift of the first singlet–singlet transition of EABP occurring upon complexation.

2.2.2.2 UP-conversion

For a solar cell, photons with energy less than the band gap are not absorbed (all are transmitted). Transmission losses can be reduced by using up conversion (combining low energy photons to one high energy photon). This low energy part of the spectrum can be accessed by using up-conversion process. The improved photovoltaic system involving an up-converter is shown schematically in Figure 2.6. It is based on a conventional bifacial single-junction solar cell made of a material with

band gap E_g . The second main element of the system is the *up-converter*, which partially transforms the sub-band-gap photons transmitted by the solar cell into high-energy photons. In our theoretical treatment we assume that the up-converter is electronically isolated from the solar cell and located behind it. A perfect reflector is located at the rear surface of the up-converter. The main mechanisms by which incident photons can be transformed to photons with higher energies are second harmonic generation, simultaneous two-photon absorption.

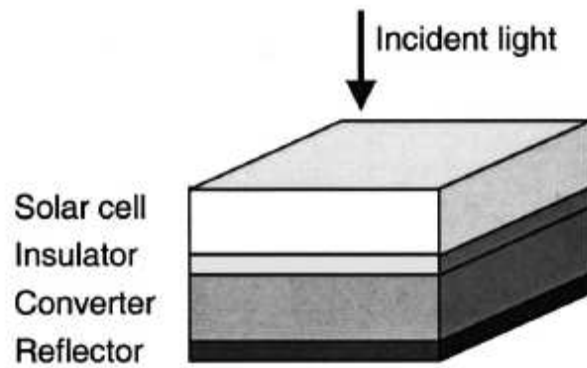


Figure 2.6: Up-conversion system of solar cell

Up-conversion involves a sequential excitation of electrons into an excited state via a real, lower-lying metastable excited state. The up-conversion processes are subdivided into three classes, namely, sequential ground state absorption/excited state absorption (GSA/ESA), energy transfer up-conversion, and photon avalanche [53]. In the literature [54], the up-conversion via GSA/ESA has so far been discussed for resonant excitation with one or two different wavelengths only, due to the fact that most of the research in this field is stimulated by commercial applications for short wavelength solid-state lasers, e.g., in telecommunication or for data storage. The necessity to use more than one wavelength is regarded as a disadvantage for these applications. However, the up-conversion is interested for photovoltaic applications involve the sequential absorption. A schematic energy-level diagram of such a broadband up-converter is shown in Figure 2.7. The up-converter consists of a material with a band gap that ideally equals the band-gap energy of the solar cell E_g and contains intermediate levels (IL) with an energy E_1 above the valence band edge (the terms valence band and conduction band will be used for the lower and the upper electronic band, respectively). The absorption of sub-band-gap photons in the up-converter leads to the generation of electron-hole pairs i.e. of electrons in the conduction band and of holes in the valence band via two sequential transitions from the valence band into the IL and from the IL into the conduction band. These transitions are symbolized by dotted arrows in Figure 2.7. A fraction of the excess electron-hole pairs are generated inside the up-converter recombines via radiative band-to-band transitions.

A solid arrow, in Figure 2.7 indicates the emission of photons with energies above the band gap. These up-converted photons can be absorbed by the solar cell, which leads to an additional generation of electron-hole pairs [55].

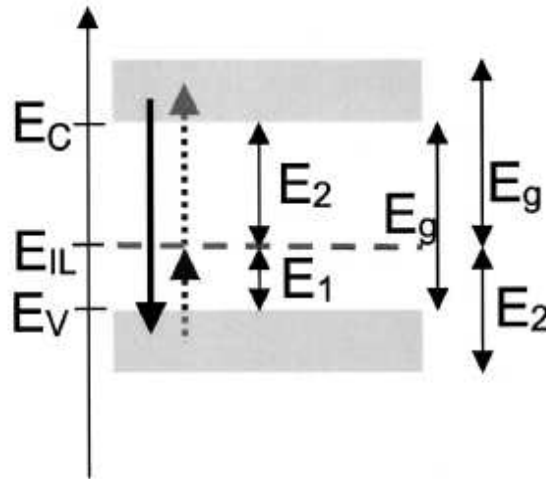


Figure 2.7: Energy levels in the up-converter [55]

One advantage of this system is that no additional recombination channel is introduced into the active solar cell material, as the up-converter is electronically isolated from the solar cell. Recombination of electrons and holes via the intermediate level is therefore possible only inside the up-converter. Another advantage is that in this system the materials of the up-converter and of the solar cell can be optimized independently. An optimized up-converter might be stacked behind any existing bifacial solar cell, potentially increasing its efficiency. A disadvantage of the up-conversion system is that, as the up-converter is electronically isolated; all $e-h$ pairs generated inside it will eventually recombine. Promising initial experimental results on silicon solar cells in combination with $\text{NaYF}_4:\text{Er}^{3+}$ up-converter (UC) which gave an EQE close to 1% at 1550 nm [55]. Significant improvements in the up-conversion efficiency of UC that convert from the IR into the VIS spectral range by co-activation with Yb, were discussed in the same literature.

2.2.3 Carrier multiplication method

A carrier multiplication (CM) process where an electron with sufficiently high kinetic energy can generate one or more additional electron-hole pairs through a scattering process is known as impact ionization. Impact ionization does not occur in conventional PV devices. Such type of process occurs in semiconductor nanocrystals (NCs) less than 10 nm in size [56]. The unique optical properties of quantum-confined semiconductor NCs, including atomic-like electronic structure and size-dependent bandgap energies, make them interesting materials for potential application in

optoelectronic devices such as solar cells. Figure 2.8 demonstrates a schematic diagram where semiconductor NC can help to improve the solar cell efficiency. When an electron in a semiconductor absorbs light with more energy than its band gap (E_g), it is excited to a higher energy level. Conventionally (top panel), any extra energy above E_g is given off as waste heat (phonons), and the result is still a single electron-hole pair. NCs (bottom panel) can demonstrate CM, in which, if the energy is high enough ($>2E_g$), it can be given to second electron instead, creating two electron-hole pairs. This would result in twice the current per high-energy photon compared to a bulk material at the same voltage [57].

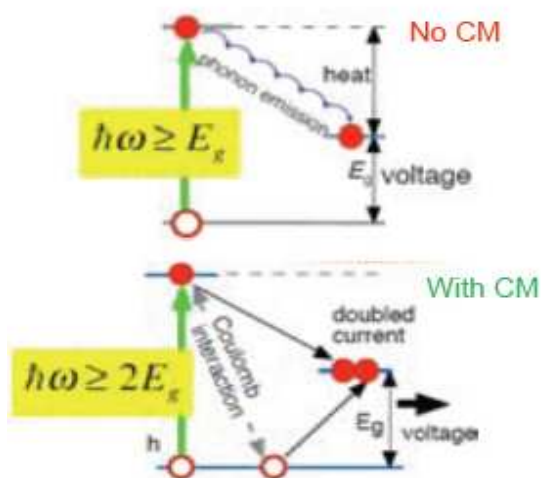


Figure 2.8: Carrier multiplication method occurs in semiconductor NC [57].

In addition, spatial confinement results in strong carrier-carrier interactions within NCs (an electron-hole pair confined to a NC is typically referred to as an exciton). Observations of photoluminescence (PL) blinking in single-NC measurements [57] were ascribed to the process of Auger ionization [58-59] in which exciton-exciton annihilation (Auger recombination) ejects an electron out of the NC core, resulting in a charged NC for which emission is quenched. The strong Coulomb interactions correlate with the prominent role played by Auger recombination within NCs occupied by more than one exciton. The PL blinking effect, together with the prospect of a phonon bottleneck to slow carrier cooling, led Nozik to propose that the inverse of Auger recombination, impact ionization, may occur with higher efficiency in semiconductor NCs [60]. Subsequent to Nozik's prediction of enhanced impact ionization in quantum-confined semiconductor NCs, experimental measurements on colloidal solutions of PbSe, PbS, and PbTe NCs revealed evidence of the single-photon generation of multiple excitons following pulsed excitation at high photon energy and low intensity, as evidenced by the signature of Auger recombination within the exciton population decay traces [61-63]. These measurements represented the first observations of multiple exciton generation in NCs. Analysis of the data indicated that single photon generation of multiple

excitons occurs on a very short time scale following photon absorption, with an efficiency that increases with the energy of the photon. Because of the very high observed efficiency of multiple exciton production, the process has been referred to as multiple exciton generation (MEG), or carrier multiplication, to differentiate it from the impact ionization (I.I.) occurring in bulk semiconductors. Subsequent measurements led to the report of as many as seven excitons per photon for large PbSe NCs photoexcited at $h\nu = 7.8E_g$ for $E_g = 0.636$ eV [64]. The effect of small-band emission spectra of NCs on solar cell performance parameters was reported by W.G.J.H.M. Van Sark *et al* [65] and they showed the potential benefits of NC use. Recently, a 6% relative increase in conversion efficiency was reported for coating a multi-crystalline silicon solar cell with a converter layer [66]. As NCs have much broader absorption bands than the species used in Ref. [66], the deployment of NCs in planar converters could lead to relative efficiency increases of 20-30%. Also, spectral down conversion employing NCs in a polymer matrix has been demonstrated in a light emitting diode (LED), where a GaN LED was used as an excitation source (425 nm) for NCs emitting at 590 nm [67]. Recently, Evren Mutlugun *et al.* [68] demonstrated semiconductor nanocrystal based photovoltaic scintillators integrated on solar cells to enhance photovoltaic device parameters including spectral responsivity, open circuit voltage, short circuit current, fill factor, and solar conversion efficiency in the ultraviolet. Hybridizing (CdSe)ZnS core-shell quantum dots of 2.4 nm in diameter on multi-crystalline Si solar cells for the first time, they showed that the solar conversion efficiency is enhanced 2 folds under white light illumination similar to the solar spectrum. Such NC scintillators provide the ability to extend the photovoltaic activity towards UV.

Chapter 3

Experimental Techniques

3. Experimental techniques

The results described in this thesis have been obtained using different experimental techniques. The details of these experimental techniques are expressed in this chapter.

3.1 Thermal evaporation

Resistive thermal evaporation is one of the most commonly used metal deposition techniques. It consists of vaporizing a solid material (pure metal, eutectic or compound) by heating it to sufficiently high temperatures and recondensing it onto a cooler substrate to form a thin film. As the name implies, the heating is carried out by passing a large current through a filament container (usually in the shape of a basket, boat or crucible) which has a finite electrical resistance. The choice of this filament material is dictated by the evaporation temperature and its inertness to alloying/chemical reaction with the evaporant. This technique is also known as "indirect" thermal evaporation since a supporting material is used to hold the evaporant. Usually low pressures are used, about 10^{-6} or 10^{-5} Torr, to avoid reaction between the vapor and atmosphere. At these low pressures, the mean free path of vapor atoms is the same order as the vacuum chamber dimension, so these particles travel in straight lines from the evaporation source towards the substrate. This originates 'shadowing' phenomena with 3D objects, especially in those regions not directly accessible from the evaporation source (crucible). Besides, in thermal evaporation techniques the average energy of vapor atoms reaching the substrate surface is generally low (order of kT , i.e. tenths of eV). This affects seriously the morphology of the films, often resulting in a porous and little adherent material. Our laboratory system is based on resistance heating (Joule effect). A schematic diagram of one such system is shown in Figure 3.1. These systems are fitted with an acoustic crystal monitor which is connected to film thickness monitor for controlling the amount of metal deposit. All filament boats used are of tungsten material.

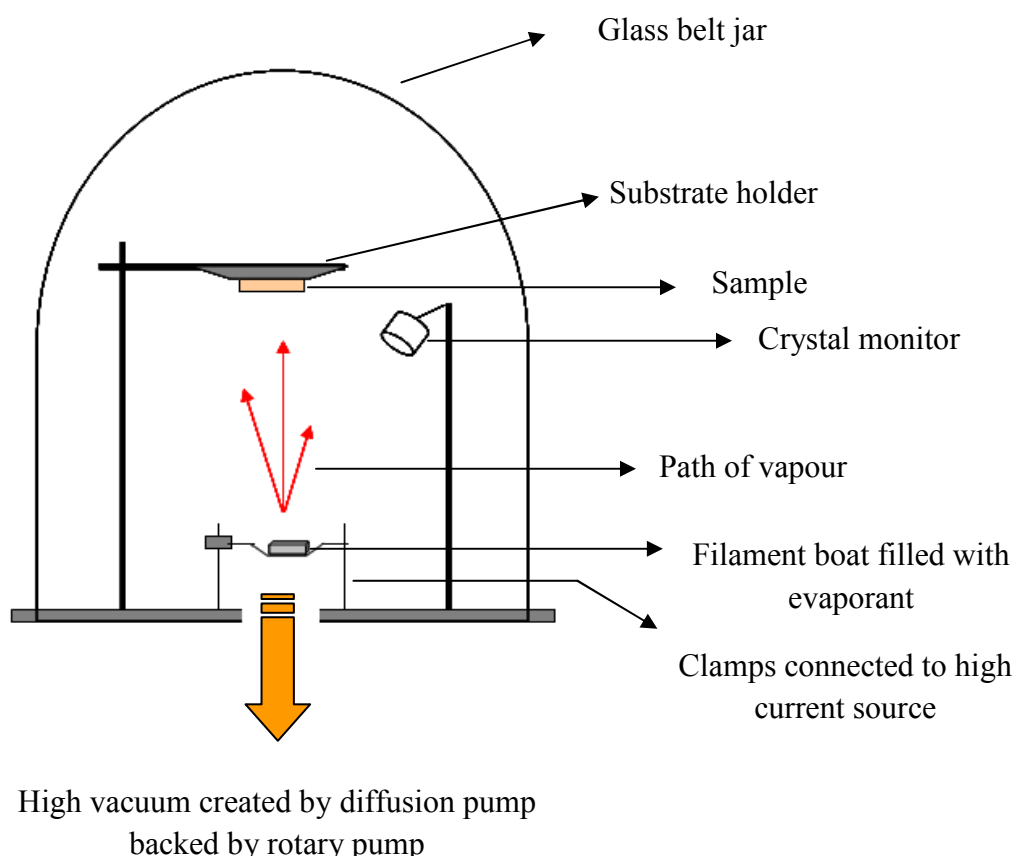


Figure 3.1: Schematic diagram of resistive thermal evaporation system used

3.2 UV-VIS measurement

Absorption as well as transmittance spectra were measured by JASCO UV-VIS spectrometer [JASCO V570] in double beam configuration as shown in Figure 3.2 and Figure 3.3. For absorption spectra measurements, the liquid or colloidal samples are put into a sample tube (called a “cuvette”), while a proper holder was used for thin film sample. The resulting data was recorded through interfaced PC with SPECTRA MANAGER software. Before measuring absorption spectrum of liquid sample, the base line was corrected using the DI water which is used as a solvent during the preparation of the colloidal sample while base line was corrected by properly cleaned glass substrate in case of thin film samples. For transmittance measurement of thin film, a sample deposited glass substrate is used in the place of sample position and another cleaned glass substrate is used in the reference position of Figure 3.3.

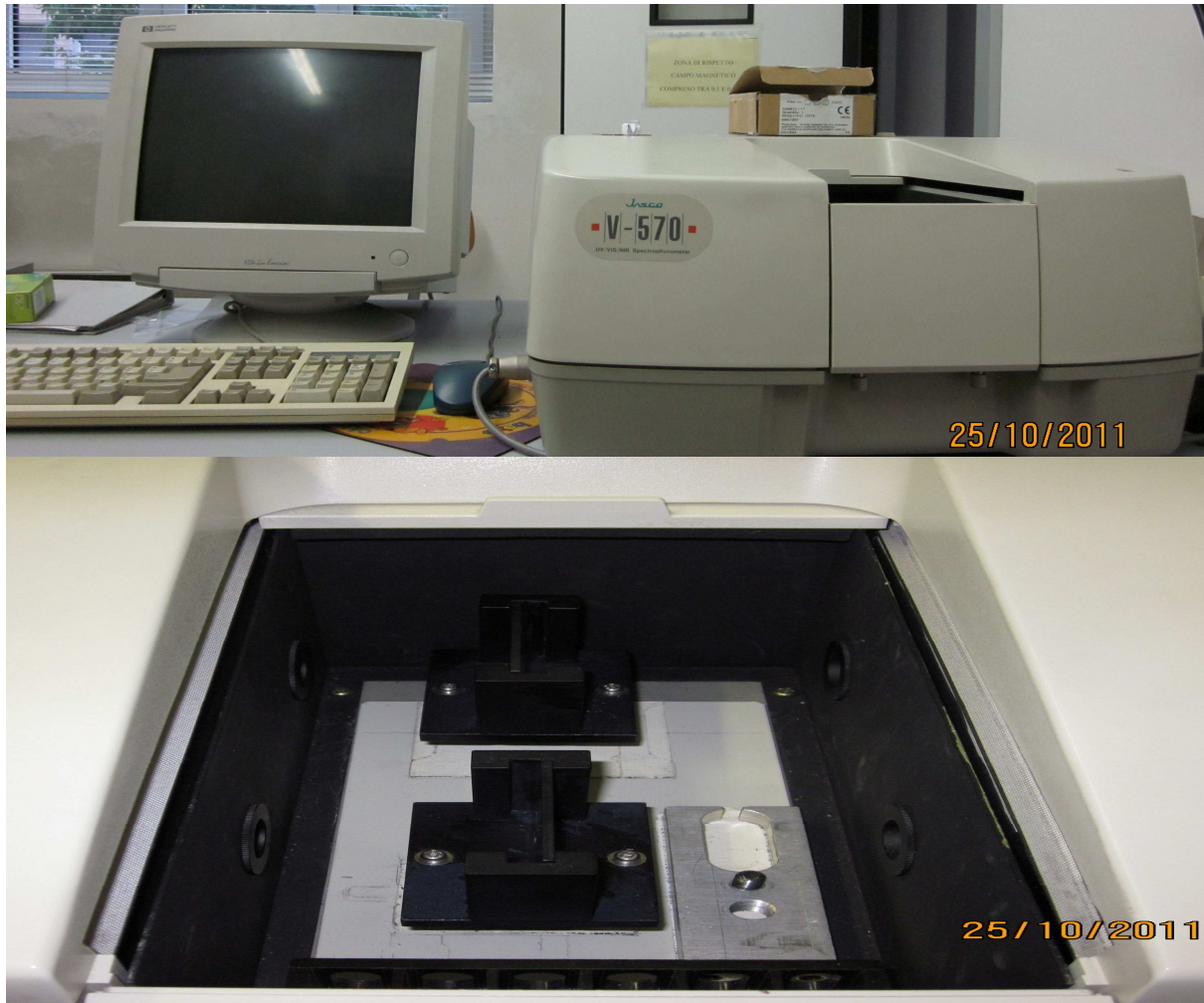


Figure 3.2: UV-VIS instrument set up

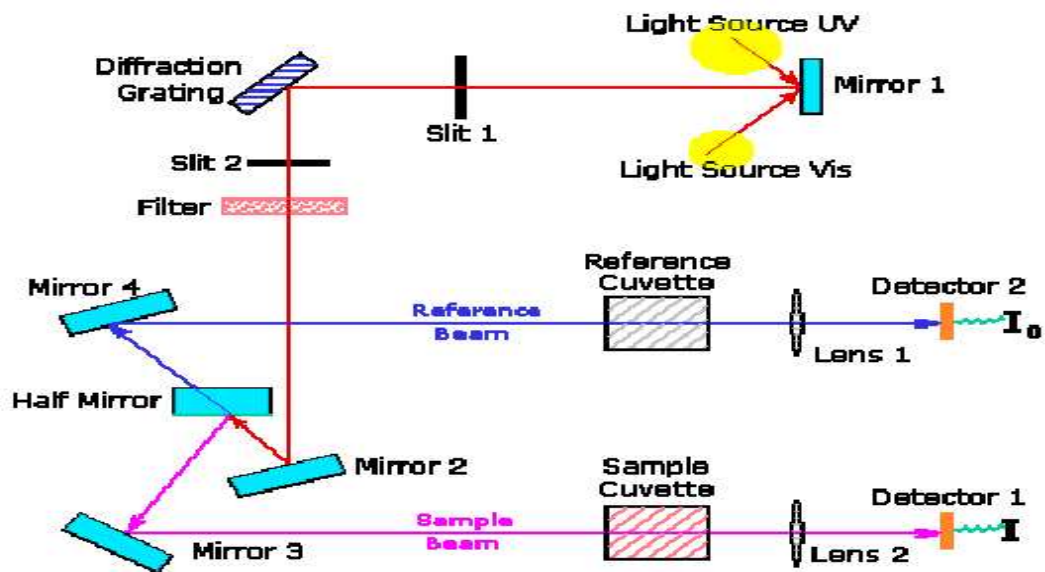


Figure 3.3: Scheme of UV-VIS spectrometer

3.3 Reflectance measurement

Reflectance measurements were carried out in CARRY UV-VIS BIO Spectrophotometer within 300 nm to 900 nm in 'VW' configuration. A dual 'VW' configuration is shown Figure 3.4.

The setup is with one spherical mirror, and two toroidal mirrors per beam. The movable mounting of the spherical mirrors allows them to be used for both calibration and sample measurement. Hence, the same optical components are in the light path during both calibration and measurement. When a sample is mounted, the only change in the system is due to the reflectivity of the sample, and absolute value of the reflectance is obtained.

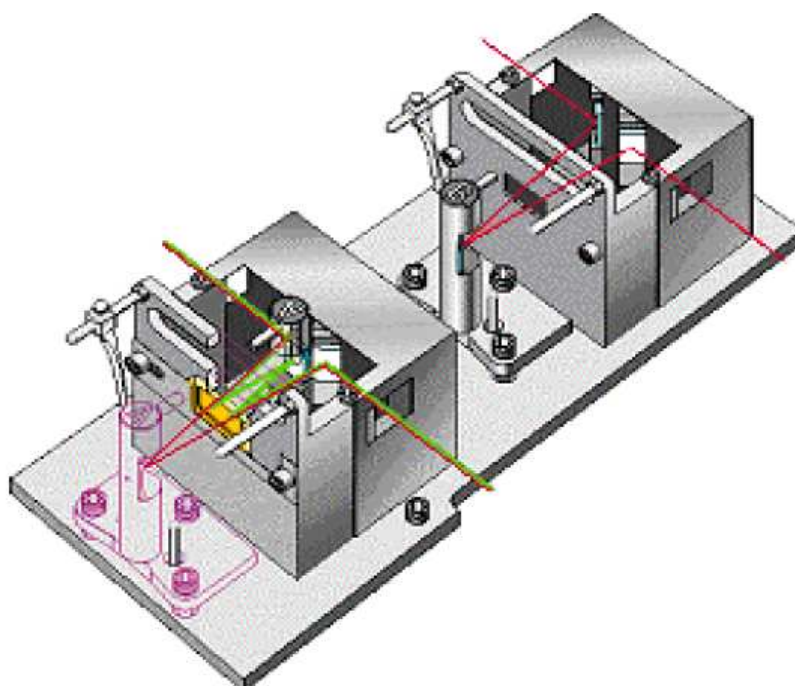


Figure 3.4: Optical diagram of the Cary 'VW' configuration.

3.4 Scanning Electron Microscope and Transmission Electron Microscope

Metal NPs sizes and distribution on substrates were measured by Tescan VEGA TS5136XM Scanning Electron Microscope (SEM) micrographs.

For SEM measurement we used Si substrate upon which the aqueous solutions were deposited by dip coating followed by drying different medium (air and hot furnace). Detail of different drying process is described in the following chapter 4. Energy Dispersive X-ray Spectroscopy or EDX can

provide quantitative analysis of elemental composition. X-rays may also be used to form maps or line profiles, showing the elemental distribution in a sample surface.

A high resolution transmission electron microscope (HRTEM; Model Tecnai S-twin) was used to observe the morphology of the nanocrystals. The photograph of this instrument is shown in Figure 3.5.

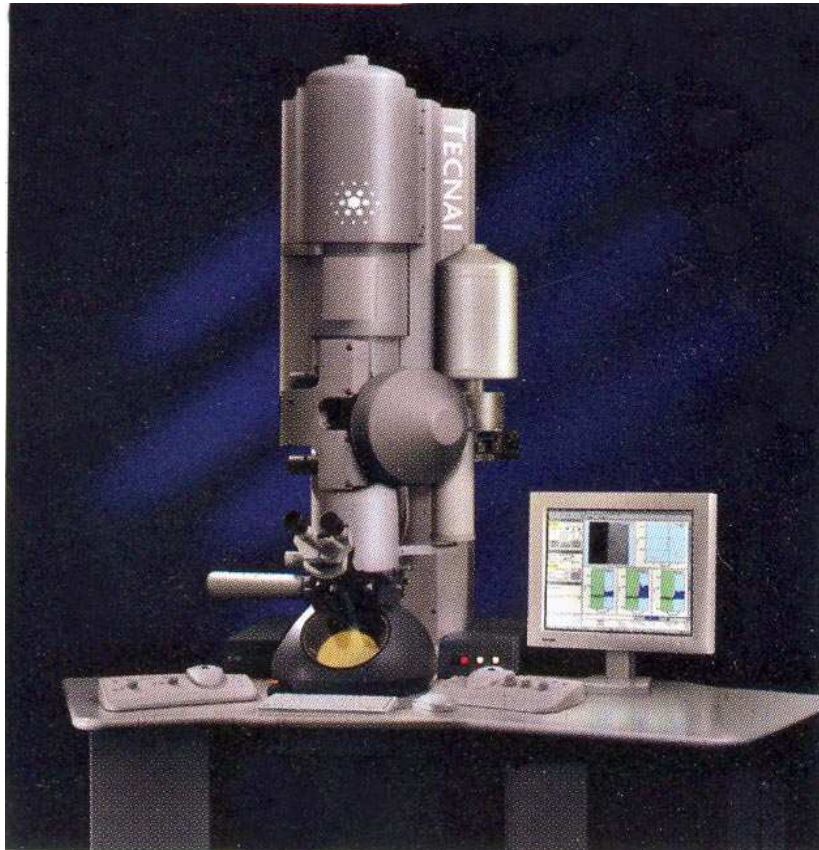


Figure 3.5: Photograph of the TEM used in our experiments

Before starting the TEM measurements, the samples were diluted twenty times using ethanol and finely dispersed in ethanol using a horn type ultrasonicator. Then four drops of the diluted solution was placed on copper grids of 2.5 mm diameter using a micro tip. Finally the copper grids were left to dry before transferring into the TEM sample chamber.

3.5 Spectral response system

The spectral response describes the sensitivity of the solar cells to optical radiation of different wavelengths.

All sections of the spectral response setup used in this work is depicted in Figure 3.6(a) and block diagram of the complete setup is shown in Figure 3.6(b). The SR apparatus includes a 450 W Xenon light source coupled with a double grating monochromator, whose slit width for these measurements is 2 mm (corresponding to a bandpass around 4.2 nm). Light coming from the monochromator through the optical fibre falls on the cell which is mounted on the sample holder. The cells are illuminated by a monochromatic beam with a diameter around 3 mm. The photogenerated current from the cell passes through an amplifier whose gain is set at 10^4 V/A and the corresponding voltage produced at each wavelength of the monochromatic light is measured by a Keithley 2400 sourcemeter monitored via PC. The SR measurements were taken from 300 nm to 1100 nm with a 2.5 nm wavelength increment. The EQE (EQE being defined as the number of charge carriers generated by the cell to the number of incident photons at each wavelength falling on the cell) spectrum is then calculated as the ratio between such SR data and the incident light spectrum, obtained by a reference photodiode (Hamamatsu S1336BQ). For each sample, at least six EQE measurements were performed by varying the spot position on the front surface of the cell. The standard deviation of such measurements is 1.27% in the range between 300 and 450 nm and 4.94% between 450 and 1100 nm.

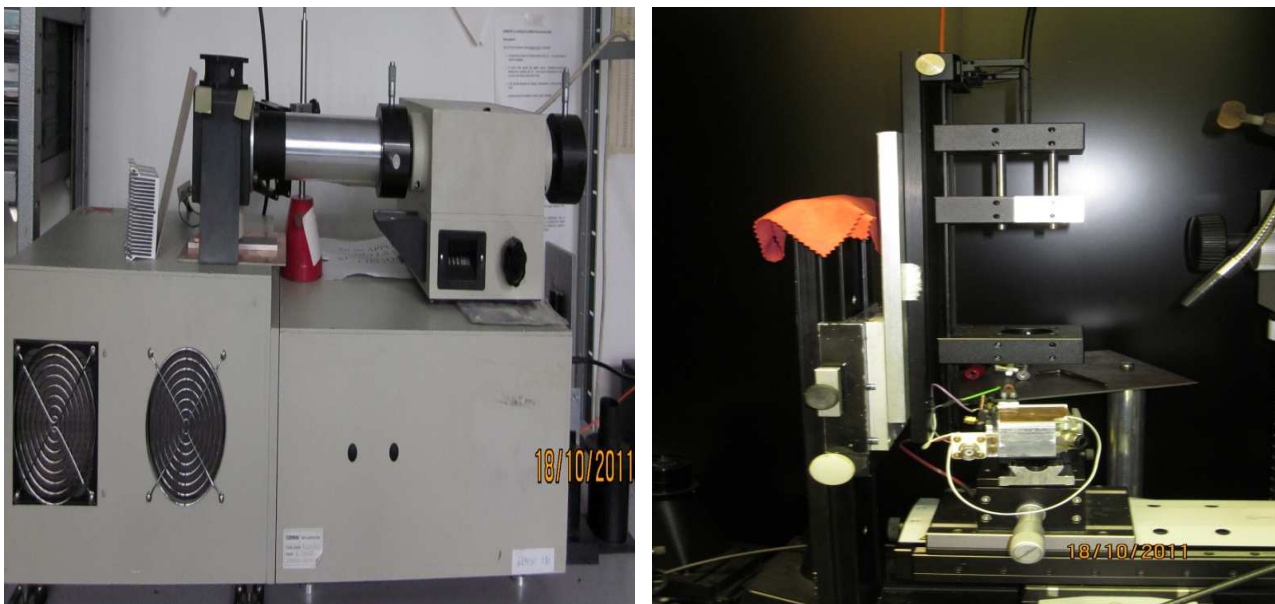


Figure 3.6(a): Different sections of spectral response setup

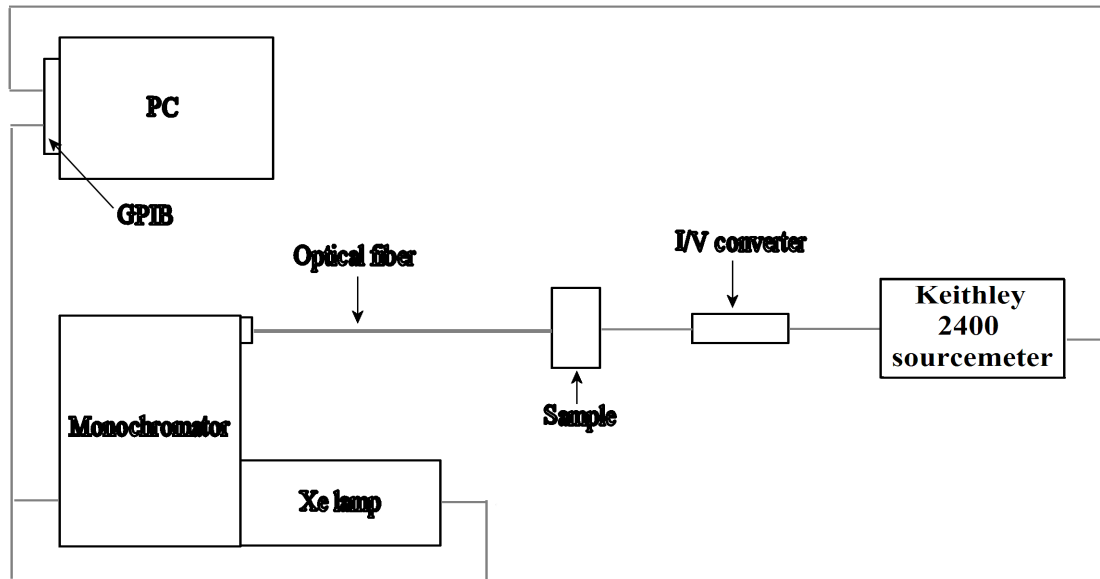


Figure 3.6 (b): Block diagram of complete spectral response setup

3.6 I-V measurements of solar cells

I-V measurements were performed in Air Mass 1.5 conditions (simulating terrestrial applications) by using Thermo Oriel Solar simulator with constant incident power density of 1 Sun (100 mW/cm^2) and a Keithley 2400 sourcemeter. The complete setup of solar simulator is used in this work shown in Figure 3.7. Solar simulator produces a highly collimated, very uniform output beam in various sizes from 2 x 2 to 10 x 10 inches. This system includes the light source, the measurement electronics, computer, and software needed to measure solar cell I-V curves. Solar simulator illuminates the test device and measures light and dark I-V characteristics by automatic solar simulator shutter control. I-V measurements were done by using 4-wire configuration with test device mounted in proper position under the light source. The back contact of the test device could be fixed with base of solar simulator by creating the local vacuum zone under the device. The solar simulator power density was monitored by a Si photodiode and maintained constant during all measurements.

The system's computer gathers data, calculates solar cell parameters like open circuit voltage (V_{oc}), short circuit current (I_{sc}), short circuit current density (J_{sc}), maximum delivered power (P_{max}) and cell efficiency (η), generates printable test reports, and saves test data in text files. In our experiments we are interested mainly about the parameters like η , I_{sc} , and P_{max} .

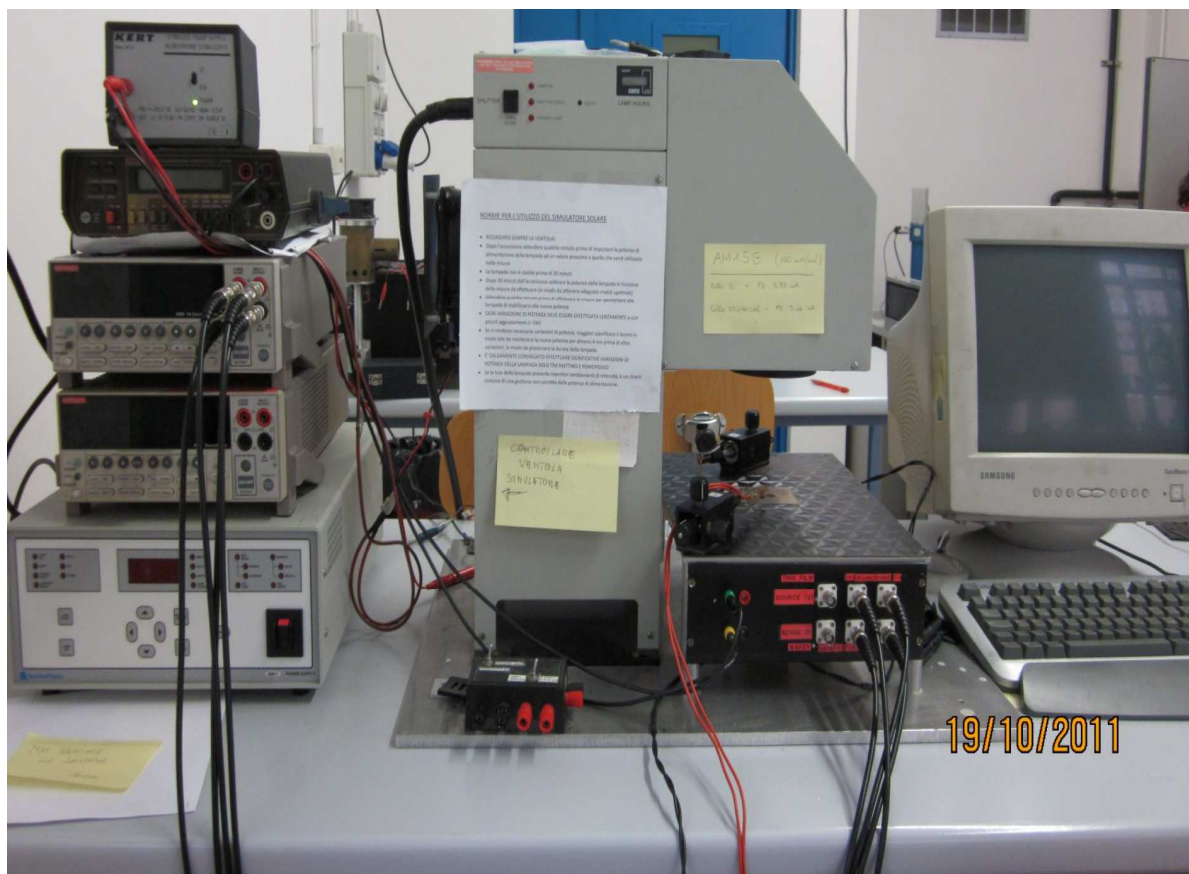


Figure 3.7: Sun simulator set up

3.7 Photoluminescence measurement

Photoluminescence (PL) measurements were carried out in JASCO FP-6300 spectrofluorometer depicted in Figure 3.8. The PL measurements were carried out at room temperature. PL excitation was performed by 150 watt Xenon lamp source. Spectral band width of the excitation and emission monochromator was set 5 nm and wavelength scanning speed was set at 100 nm/min.

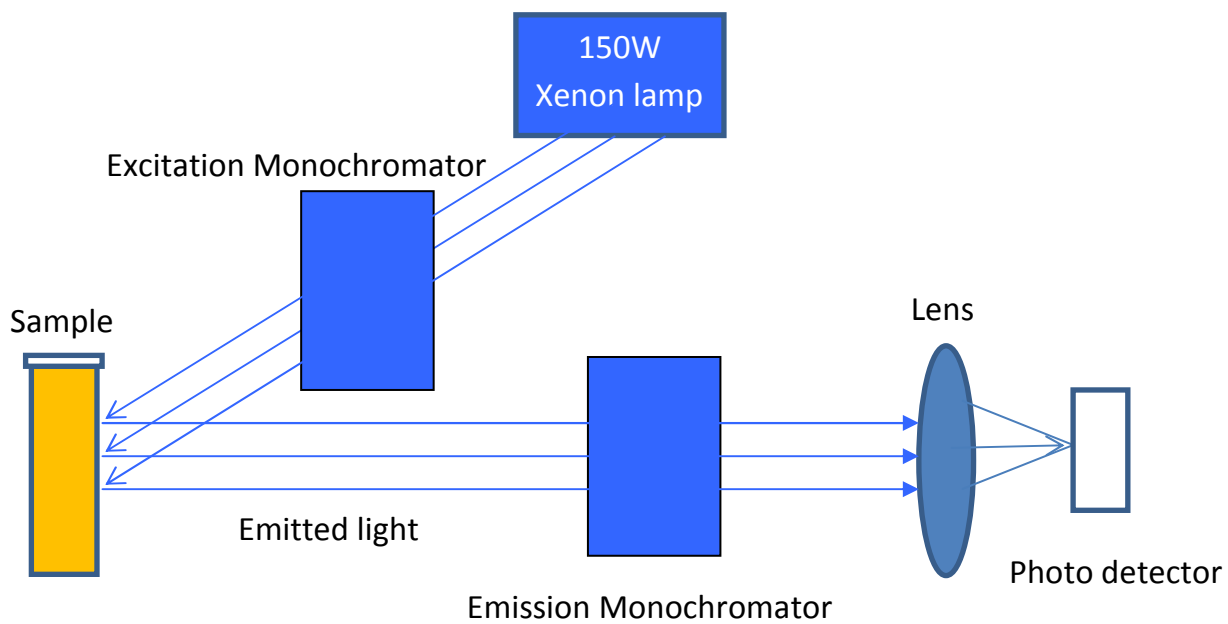


Figure 3.8: Typical diagram of PL measurement setup

Chapter 4

Light Scattering Effect by Metal Nanoparticles: Experimental Results

4.1 Introduction

In recent years, electromagnetic properties of metal NPs are increasing attention of scientists because of their various potential applications in advanced optics, electronics, sensors and catalysis etc [69]. There is currently a great deal of interest in surface plasmons on metal surfaces and metal NPs, and the often surprising optical properties associated with them. The effect of Surface Plasmon on Si solar cell has been already described briefly in the section (2.2.1) of chapter 2. The aim of this chapter is to describe the various synthesis process of different metal NPs and then deposition methods on substrates followed by different measurements on them. Finally, different photovoltaic devices will be tested with the metal NPs synthesized with colloidal technique.

So selection of particular metal among the many is mandatory first.

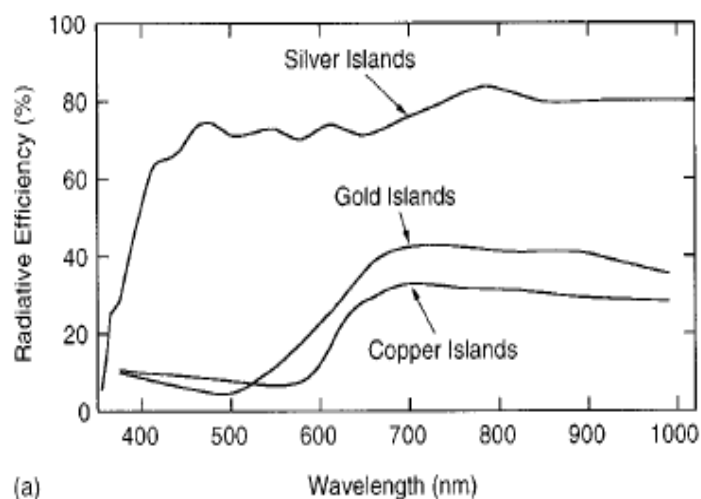


Figure 4.1: Radiative efficiency of different metal NPs [35]

It should also be remarked in Figure 4.1 that different metal NPs show different radiative or scattering efficiency, and it has been shown [33] that silver particles have higher radiative efficiency with respect to other metal NPs, such as gold and copper. Silver is therefore the best choice among other metal NPs for the design of light trapping strategies aimed to increase the conversion efficiency of PV devices.

There are varieties of methods for the preparation of metal NPs, such as physical deposition method (vacuum evaporation and sputtering), electrochemical deposition, the Langmuir-Blodgett technique and the layer by layer (LBL) assembly method. In addition, several methods for the fabrication of patterned NP have been developed, such as lithography, microcontact printing.

So far the effect of surface plasmons on Si PV devices has been studied mostly on silver NPs deposited by means of thermal evaporation technique [24, 32-34, 70], but the application of

plasmonic coupling effects in large-area PV module production requires new inexpensive and scalable techniques for fabricating metal NPs in a controlled way. To this purpose, colloidal synthesis should be an attractive solution for producing metal NPs with the desired optical properties. The colloidal approach presents in fact the advantage of being easily scalable for relatively inexpensive large production [71], and can be introduced in the present Si PV device production lines without strong modifications of the industrial process for the PV module fabrication. Moreover, the synthesis of metal NPs via colloidal technique has been demonstrated to be a very effective, reliable and versatile route for their production in a variety of compositions, shapes and sizes [72].

In the present work we want to deposit the metal NPs on bulk silicon solar cells by colloidal technique in order to enhance their photovoltaic conversion efficiency by means of their Plasmonic Light Scattering. We tested for the first time the deposition by colloidal method of silver NPs on multicrystalline silicon (mc-Si) solar cells to enhance their performances. In spite of the higher scattering efficiency, the possible oxidation of silver NPs could affect their plasmonic properties. Therefore, in order to obtain a further confirmation of the PLS effect due to colloidal gold NPs on mc-Si have been also studied.

Before starting the colloidal deposition, we used to deposit silver and gold NPs by thermal evaporation and sputtering respectively on glass substrate in order to do preliminary investigation of plasmonic effect and make comparison with the literature data. In the second part, we will concentrate on colloidal solution technique.

4.2 Experimental

In experimental section, different process for the preparation of different metal NPs followed by their deposition methods on the substrates and solar cells will be discussed

4.2.1 Deposition of silver and gold films on glass substrate by thermal evaporation and sputtering

First we used evaporation technique to deposit silver and RF sputtering to deposit gold on glass substrate. We followed the methodology reported in the reference [24]. We deposited various thickness of silver on cleaned glass substrates by evaporation technique under high vacuum (2×10^{-6} torr) condition. The thickness of silver film was about 3nm, 8nm and 10 nm respectively and then the samples were annealed at 200°C within hot furnace in N₂ environment for 50 mins. We followed the same procedure for depositing different thickness (3nm, 6nm and 10nm) gold on glass

substrate by sputtering method for 15s, 30s and 45s respectively at deposition rate ~15 nm/min and then samples were heat treated at 300°C for 2 hrs in N₂ ambient condition.

Then we measured the UV-VIS spectroscopy measurement both before and after annealed condition and also performed SEM measurement to observe the surface morphology of the samples.

Colloidal method

In colloidal method, metal NPs can be synthesized by using different capping or stabilizing reagents [73]. In this present work we first used micelle (which is formed by surfactant dissolve in different solvent) for producing metal NPs. Also polymer was used as a stabilizer for the synthesis of metal NPs.

4.2.2 Preparation of colloidal silver NPs using surfactant: Method A

A **micelle** is formed when a variety of surfactant molecules including soaps and detergents are added to water. The molecule may be a fatty acid, a salt of a fatty acid (soap), phospholipids, or other similar molecules. A typical micelle is shown in Figure 4.2.

The molecule must have a strongly polar "head" and a non-polar hydrocarbon chain "tail". When this type of molecule is added to water, the non-polar tails of the molecules clump into the center of a ball like structure called a micelle, because they are hydrophobic or "water hating" [74]. The polar head of the molecule presents itself for interaction with the water molecules on the outside of the micelle.

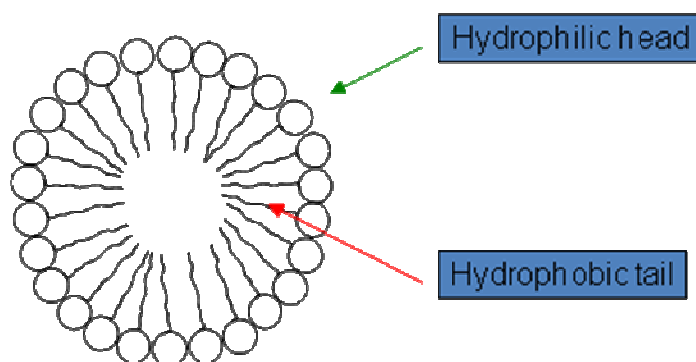


Figure 4.2: Structure of a general Micelle on aqueous solvent

The shape and size of a micelle is a function of the molecular geometry of its surfactant molecules

and solution conditions such as surfactant concentration, temperature, pH and ionic strength. The particles can be formed inside the micelle. So the particle size depends on the surfactant concentration.

Silver nitrate (AgNO_3), sodium borohydride (NaBH_4) and Sodium dodecyl sulfate (SDS) are required for synthesis of the silver NP. Pure de-ionized (DI) water was used as a solvent during the synthesis process. The chemical structure of SDS is shown in Figure 4.3.

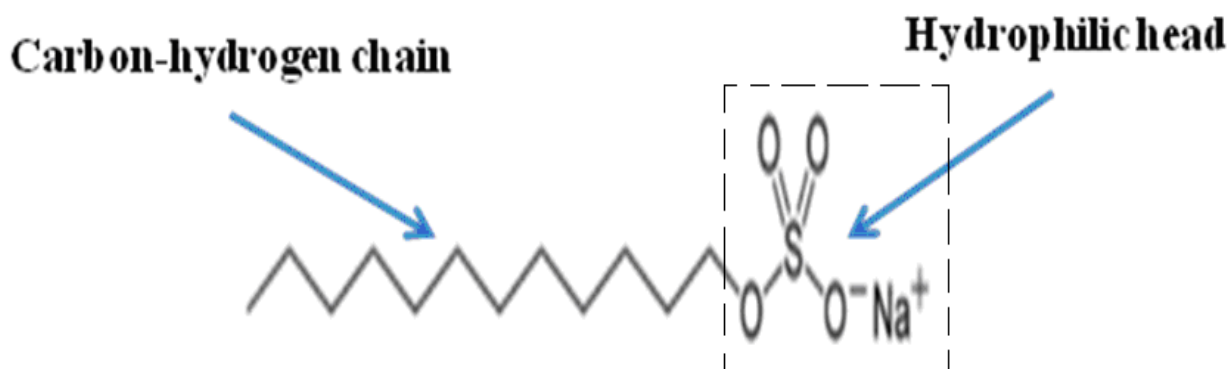


Figure 4.3: chemical structure of SDS [Dashed part of this structure is the hydrophilic head and remaining part (carbon hydrogen) chain is the hydrophobic part. Both the hydrophilic and hydrophobic part of the SDS structure forms the same shape as shown in Figure 4.2]

For colloidal synthesis of silver particle, we used different concentration of AgNO_3 solution and solution of reducing agent NaBH_4 making constant of SDS concentration of 10^{-3}M . 25ml of AgNO_3 solution was added with 25ml of aqueous surfactant (SDS) medium in a chemical reactor with rapid stirring on a hot water bath at temperature of 80°C . After 15 min NaBH_4 solution was added dropwise into the mixed solution under the same condition for another 10 min. After few moments, it was observed that various colour of the resulting solution depending upon the concentration of both AgNO_3 and NaBH_4 solution and the solution was kept to cool down at room temperature. During all the above courses, light was kept away from all the reactants. After completion of the synthesis process, the resulting solutions were centrifuged (2500 r.p.m) followed by washed in DI water. Thus freshly prepared colloidal silver NPs solution will be used for further steps of experimental procedure.

4.2.2.1 Preparation of silver NPs coated substrates

Typical Layer by Layer (LBL) [69] process was carried out for the fabrication of Ag/PDDA film on glass substrate. A cleaned substrate of glass and silicon slide was dipped only once into 1% of Poly

Diallyl Dimethyl Ammonium chloride (PDDA) for 30 min. After being rinsed with water, both the substrates were immersed for 15 min in colloidal solution and followed by drying in air. Optical absorption spectroscopy was performed on both colloidal solutions as well as NPs coated glass substrate whereas, for SEM analysis we used Si substrate with silver NPs.

4.2.2 Deposition process of the silver NPs (prepared with method A) on Si solar cells

Firstly, Si solar cells were masked in small portion in order to avoid contact related problems during electrical measurements on the same cells. After that, Si solar cell was dipped into PDDA solution for 30 min followed by drying in air. Then these PDDA coated cells were dipped into aqueous colloidal solution followed by drying same in air.

4.2.3 Preparation of silver NPs using polymer as a stabilizer: Method B

A different preparation method of silver NPs via chemical reduction method, silver nitrate (AgNO_3), PolyDiallylDimethylAmmoniumchlorides (PDDA), and sodium borohydrate (NaBH_4) were used. Pure DI water was used as solvent during the whole preparation. Silver NPs were prepared according to the following procedure: first of all, 10 ml of 0.0011 M AgNO_3 aqueous solution and 50 ml of 11.1 wt% PDDA aqueous solution were mixed in a reactor. The reactor was then placed in a cold water bath at 7°C in continuous stirring condition. After 10 minutes, 5 ml of 8×10^{-4} M NaBH_4 were added dropwise (1 drop per second) to the solution maintaining the same conditions. Faint yellow colour appeared within 1 minute. With the progress of the reaction time, the colour of the solution changed from faint yellow to orange. After the addition of the whole NaBH_4 solution, the reaction process went on for further 10 minutes. Then the reaction vessel was removed from the heating element and kept in stirring until cooling to room temperature.

4.2.4 Gold NPs synthesis by colloidal method

The chemicals required for the preparation of gold colloidal solution are instead gold chloride (HAuCl_4) and trisodium citrate ($\text{C}_6\text{H}_5\text{O}_7\text{Na}_3$). The whole synthesis was carried out in aqueous medium. The gold colloid was prepared by using a chemical reduction method according to the description of Lee et al. [75]. All solutions of reacting materials were prepared in DI water. The reaction vessel was placed in hot water bath (temperature around 90°C), and 10 ml HAuCl_4 (0.001 M) mixed with 20 ml DI water were placed into the vessel and heated to boiling under magnetic stirring condition. Then 10 ml of trisodium citrate (0.01 M) was added and vigorously mixed while maintaining the same temperature and stirring condition. Mixture solution was heated until colour change to red was evident. Then, as in the case of the silver NPs synthesis previously described, the

reaction vessel was removed from the heating element and kept in stirring until cooling to room temperature.

In synthesis procedure we reduced the amount of citrate solution maintaining the volume ratio between HAuCl_4 and citrate solution as (A) 3:1, (B) 5:1 and (C) 7.5:1

In our results and discussion section we will use different solution name as Solution A, Solution B and Solution C according to the change of the volume ratio of salt and reducing reagent respectively.

4.2.5 Deposition process of colloidal silver and gold NPs (prepared by Method B) on various substrates

A properly cleaned glass slide was dipped into the resulting silver colloidal solution for 2 minutes followed by hot furnace drying at 200°C under N_2 flowing for 15 minutes. The same procedure was carried out for gold NPs. Absorption spectra were then performed on such samples by a dual beam UV-VIS spectrophotometer (JASCO V570) over the wavelength range 300-1100 nm.

In order to measure the particle size and their distribution, a small portion of a Si wafer previously etched with dilute hydrofluoric acid (HF) was dipped into the colloidal silver solution followed by the above mentioned hot furnace drying and examined by a Tescan VEGA TS5136XM Scanning Electron Microscope (SEM). A drop of colloidal gold solution was placed on etched Si slices for the same kind of measurements.

The same dipping and drying procedure was carried out for the deposition of colloidal particles on mc-Si solar cells both with (ARC cell) and without anti-reflection coating (NOARC cell). Before the deposition, the cell metal grids were masked in order to avoid any contact related problems during subsequent electrical characterization. After the contact masking removal, all the electrical and optical characterizations on both ARC and NOARC cells were carried out before and after metal NPs deposition.

4.2.6 Light irradiation for removal of Boron-Oxygen complexes from Si solar cells

It should also be remarked that, before any deposition and analysis, the mc-Si solar cells have been irradiated with a 450 W lamp for 4 hours in order to obtain a constant concentration of Boron-Oxygen (BO) complexes in the Si matrix. In fact, it is widely known in the literature [76-77] that the high Oxygen content coming from the silica crucible together with the p-type Boron doping is responsible both in crystalline and multicrystalline Si cells for the formation of BO complexes under illumination. This effect gives rise to a decrease of the open circuit voltage value during I-V

measurements under simulated solar conditions, therefore affecting the reliability of such electrical characterization. Since the concentration of BO complexes reaches the maximum value after few hours under illumination, the above mentioned irradiation treatment allows the determination of reliable values of the solar cell performances.

4.3 Results and discussions

Before going into the plasmonic effect on solar cells, we tried to optimize the NP synthesis in different approach (although, the main attention is on colloidal metal NPs) and studied the effect of particle size on optical absorption or transmittance property.

4.3.1 Results on NPs (silver and gold) prepared by physical deposition (thermal evaporation and RF sputtering) method

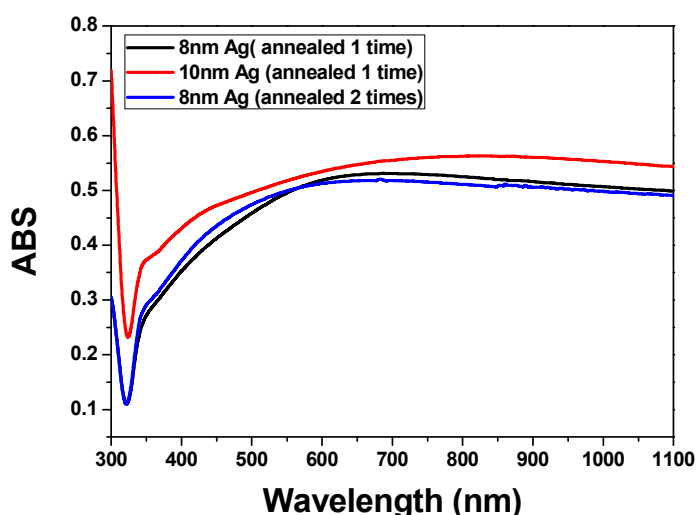


Figure 4.4 Absorption spectra of silver particles grown with different silver thin film thickness. The measurements were done after the heat treatment at 200°C in N₂ environment

The spectrum depicted in Figure 4.4 does not show the absorption peak in visible range. This might be due to high mass thickness of the silver film and SEM picture (Figure 4.5) also shows that there is no particle formation on the glass substrate. Probably the temperature used is not sufficient to form the NP after thermal treatment or the film thickens was too high. But silver NPs formed by film thickness of 3 nm (after heat treatment) has the prominent absorption peak at visible range (Figure 4.6). Also the transmittance plot (Figure 4.7) of this particular sample shows same agreement with that of literature [24]. The SEM picture of 3 nm thickness of silver after annealed

condition is shown in Figure 4.8 and it confirms that particles are formed and homogeneously distributed throughout the sample. The average particle size is about 15nm. In both Figure 4.6 and Figure 4.7 silver NPs show the Surface Plasmon Resonance Frequency (SPRF) is around 450 nm and also exhibits high transmittance above this wavelength. In Figure 4.9, gold particles show same behavior of silver particles but resonance condition is around 580 nm in agreement with the result of D.G.Hall et.al. [36]. But different gold thickness shows different results (Figure 4.9). The same trend has been observed in the case of silver NPs. After heat treatment, the higher thickness of gold sample loses their transmittance property.

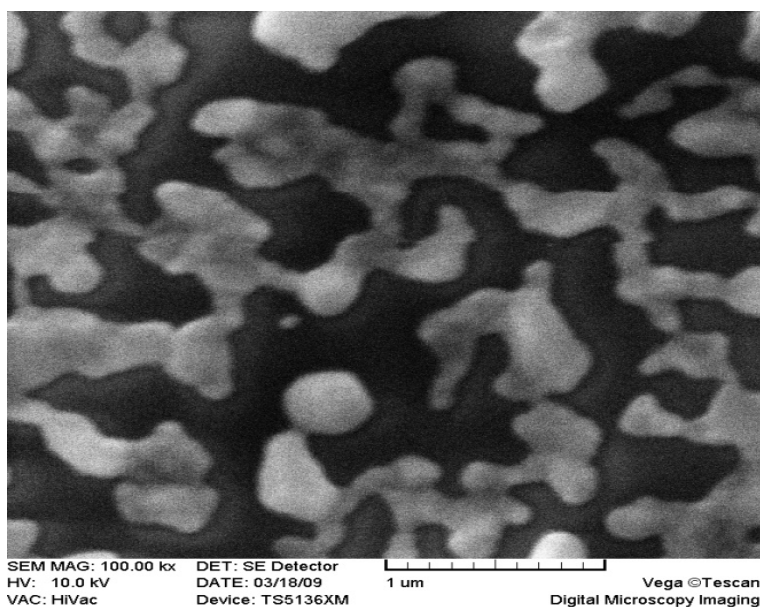


Figure 4.5: SEM image of silver film with thickness ~10 nm after heat treatment

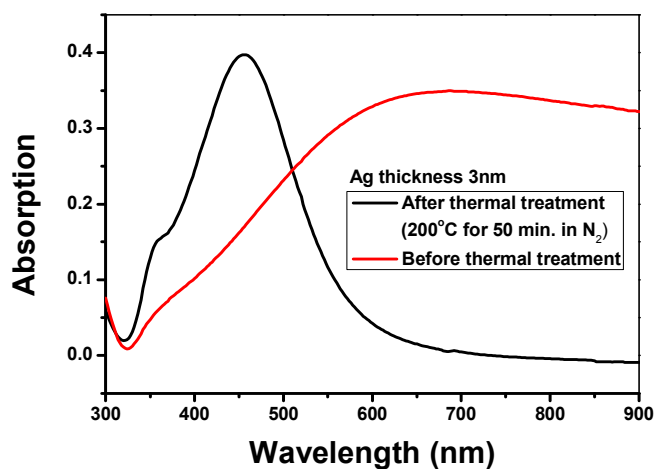


Figure 4.6: Absorption spectra of 3 nm thickness of silver film (before and after heat treatment)

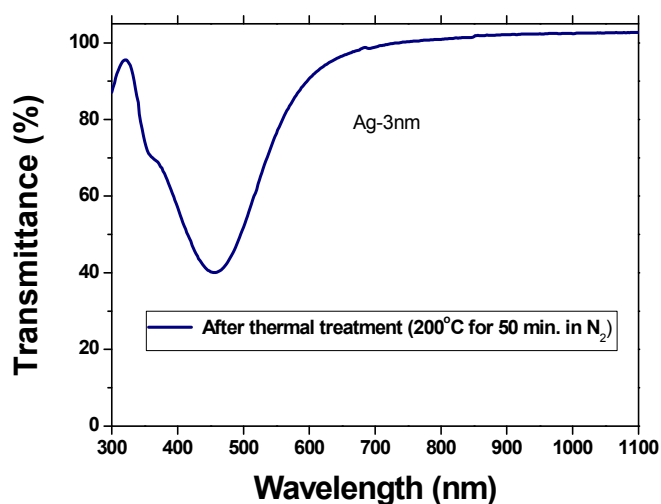


Figure 4.7: Transmittance spectra of 3 nm thickness of silver (after heat treatment)

Also SPRF peaks become broader with the increase of mass thickness. It can be explained by considering that the heat treatment might be insufficient to convert higher mass thickness metal to dispersed NPs (metal islands). UV-Vis results of both silver and gold NPs confirm that lower mass thickness is the best way to obtain the desired NPs which are much responsible for plasmonic effect.

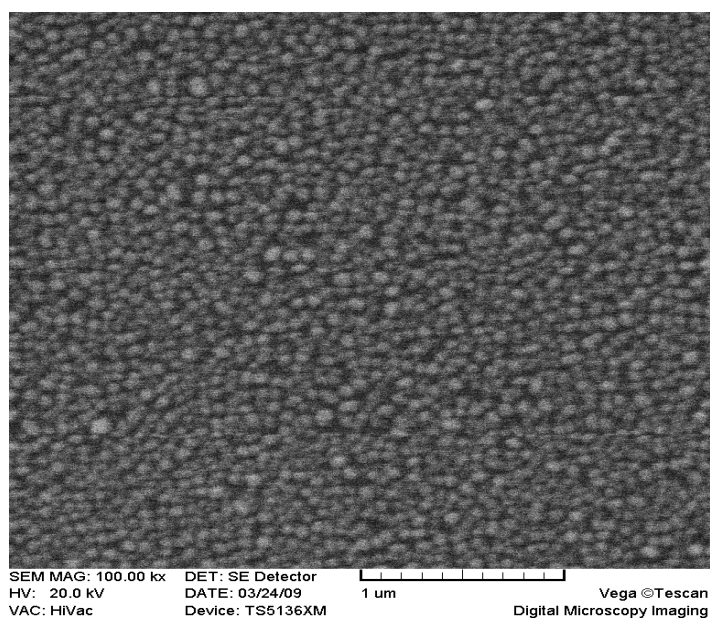


Figure 4.8 SEM image of silver NPs formed by film of 3 nm thickness

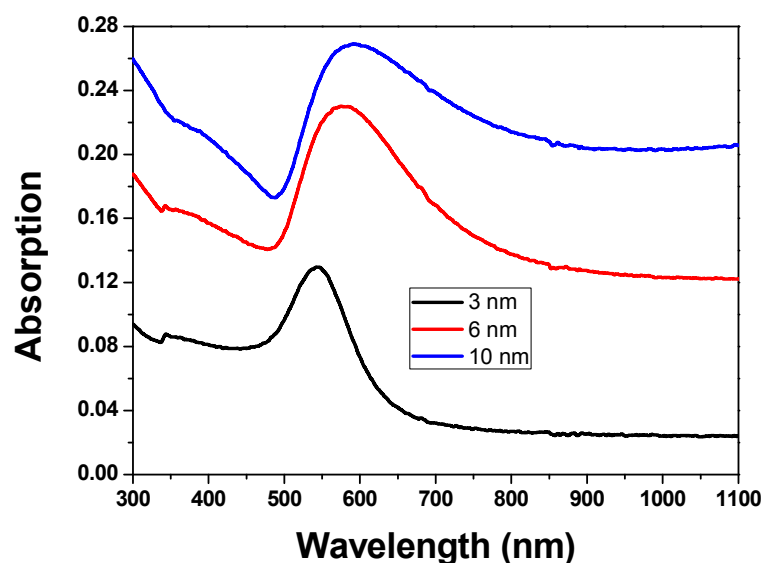


Figure 4.9: Absorption spectra of gold particles with various mass thickness on glass substrates

4.3.2 Results on colloidal silver NPs prepared with Method A

4.3.2.1 UV-Vis study

The effect of different parameters on SPRF has been monitored by UV-Vis spectrum of silver NPs solution synthesized using Sodium Dodecyl Sulfate (SDS) as a surfactant.

4.3.2.1.1 Change of $AgNO_3$ concentration

Absorption spectra of different silver colloidal solutions obtained using different concentrations of silver nitrate salts are shown in Figure 4.10. There is no such change of plasmon absorption peak using same concentration of surfactant. The peak position of SRPF is around 414 nm for three colloidal solutions. But maximum of plasmon absorption peak increases with the increase of concentration of silver salt solution. With increasing the silver nitrate concentration, the intensity of the maximum plasmon peak increased, indicating that higher concentrations of silver NPs were formed. The particle sizes do not change with the using same concentration of SDS. The narrower of absorption peak is treated to the better degree of dispersion of NPs in colloids. The broadening of the absorption peak indicates the aggregation of silver NPs [78].

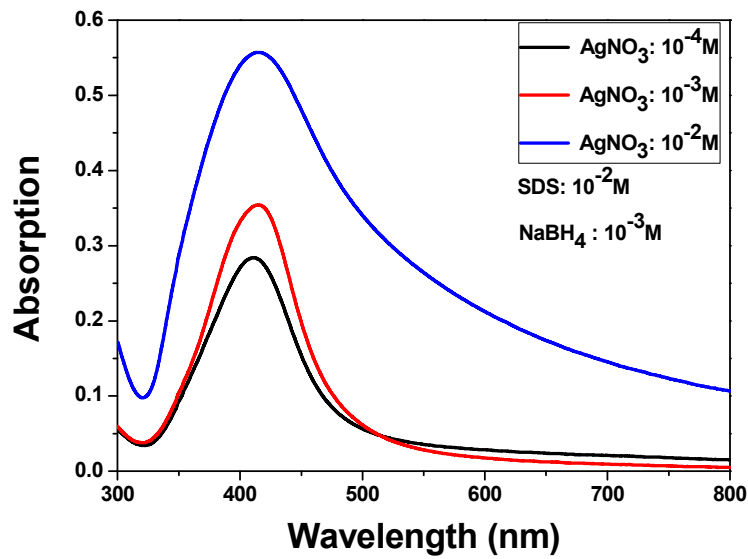


Figure 4.10: Absorption spectra (water used as reference solution) of different colloidal solution

4.3.2.1.2 Effect of centrifugation

Figure 4.11 shows the effect of centrifugation on the absorption property of the colloidal solution. After centrifugation, neither SRPF peak position nor the amplitude has changed. But the shape of the curve has changed due to removal of some waste part of chemical species used during synthesis.

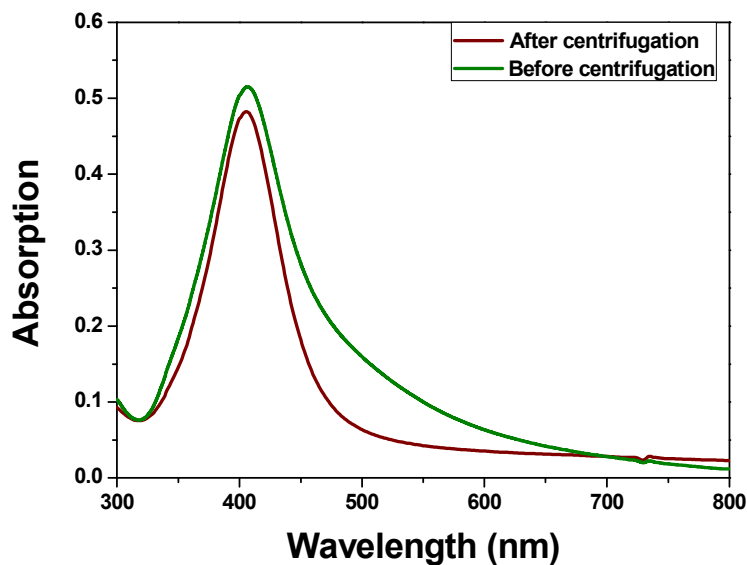


Figure 4.11: Effect of centrifugation on absorption spectrum of colloidal silver NPs

4.3.2.1.3 Effect of PDDA matrix

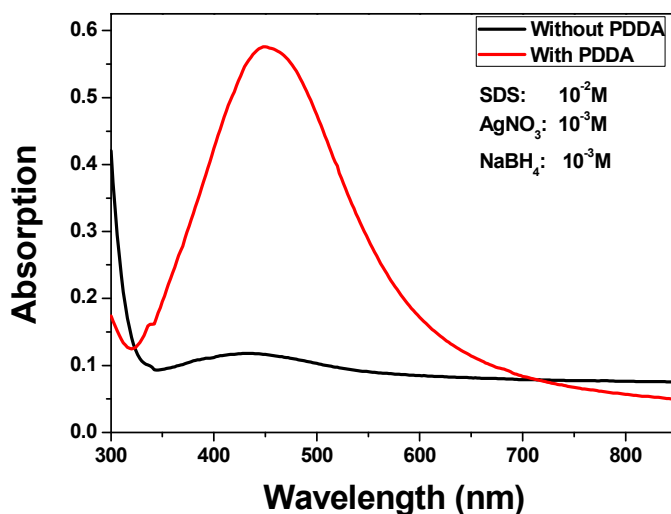


Figure 4.12: Absorption spectra of silver NPs on both without and with PDDA deposited glass substrate

Figure 4.12 indicates that the absorption spectra of silver particle deposited on with and without PDDA coated glass substrate. From this figure it is attributed that silver particles deposited on cleaned glass substrate show lower peak compared with peak obtained from silver particles on the PDDA coated glass substrate. This indicates that better distribution and more number of silver NPs on PDDA coated glass substrate. Higher absorption peak might be also minimization of interparticle distance. Possible explanation should be some agglomeration of particles on PDDA surface. In Figure 4.12 it is clearly visible that there is red shift of SRPF peak of about 22 nm (427 nm of black line to 449 nm of red line). According to [70], the possible explanation could be due to the different refractive index of underlying layer of NPs. In our case refractive index is different between clean glass substrate and PDDA deposited glass substrate (1.5 for glass & 1.41 for PDDA). The red shift of the SPRF is interesting for light trapping in Si solar cells.

4.3.2.1.4 Change in concentration of surfactant

Figure 4.13 shows UV-VIS absorption study of different colloidal silver NPs synthesized using different SDS concentration. The graph was obtained from different colloidal particles on PDDA coated glass substrate. Lower concentration of aqueous SDS solutions makes larger micelle core so as to larger silver particle. So red shift of resonance peak is related with increasing the particle size.

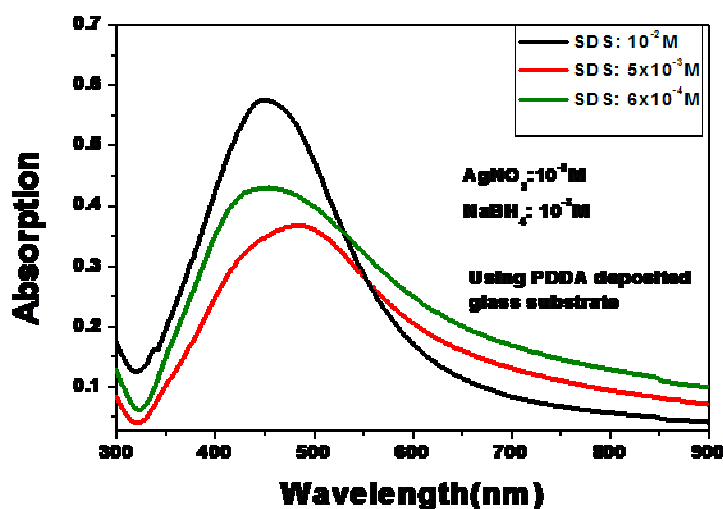


Figure 4.13: Absorption spectra of silver particle with variation of SDS concentration

Henceforth, the particle sizes can be tuned by varying the micelle concentration. But blue shift of resonance peak of silver NPs synthesized using lowest SDS concentration could not clear. However the NPs obtained from the optimum SDS concentration ($5 \times 10^{-3} \text{M}$) will be used for further experimental measurements. Because silver NPs synthesized using this SDS concentration ($5 \times 10^{-3} \text{M}$) shows maximum redshift of the SPRF.

4.3.2.2 SEM analysis of silver NPs deposited on Si substrate

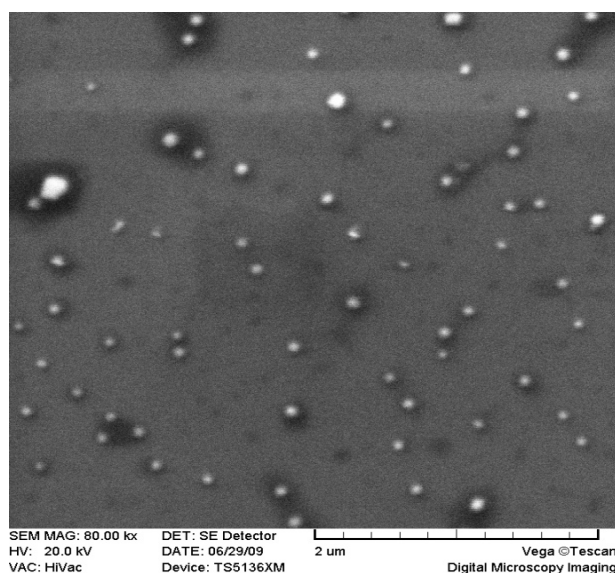


Figure 4.14: SEM picture of colloidal silver NPs (prepared with method A) on Si substrate

SEM image of silver NPs prepared with optimum SDS concentration is shown in Figure 4.14. The particle sizes of the colloidal silver are almost same around 50 to 60 nm. Only few big particles are

observed. This could be due to some agglomeration of few smaller particles on PDDA surface.

4.3.2.3 Spectral Response measurements of Si solar cells with and without silver NPs prepared with method A

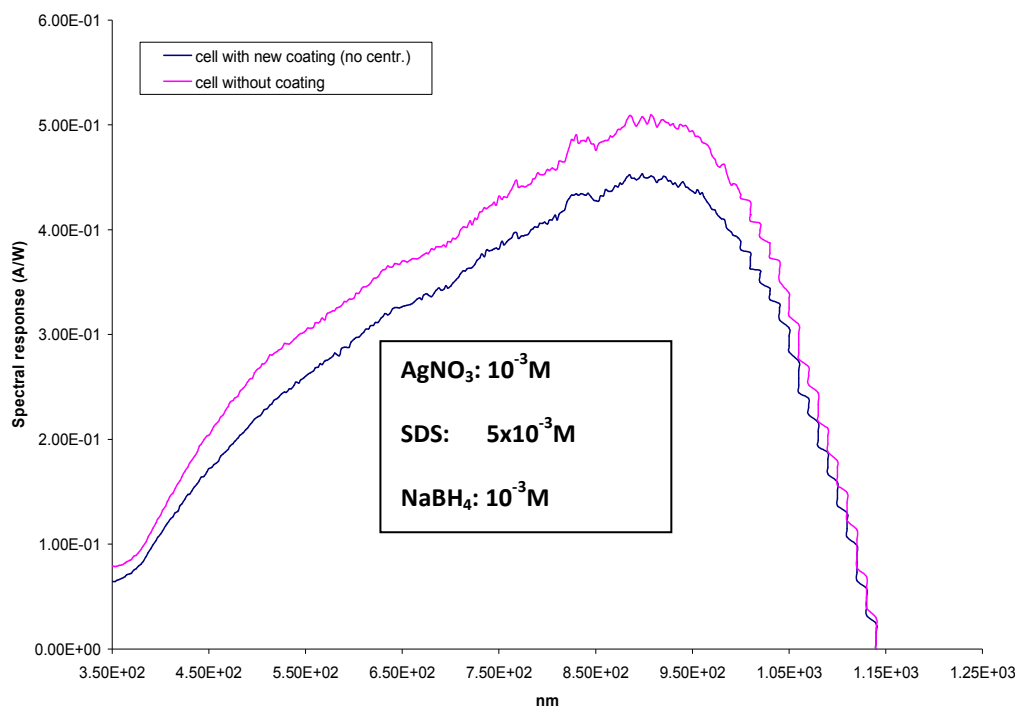


Figure 4.15: spectral response measurements of Si solar cell coated with silver NPs (here freshly prepared colloidal NPs solution was used. But solution was not washed with centrifugation process)

Figure 4.15 shows the spectral response of mc-Si solar cell with and without silver NPs coating. It is clearly monitored that there is a strong decrease of spectral response throughout whole wavelength region after coating of silver NPs. In this case we used the colloidal NPs without centrifugation. There might be some waste chemical species which disturbs the light transmittance to the active cell surface. The spectral response of the cell with aqueous NPs centrifuged one time is depicted in Figure 4.16. It is attributed that there is some improvement of spectral response, although overall decrease of spectral response is also observed in this case.

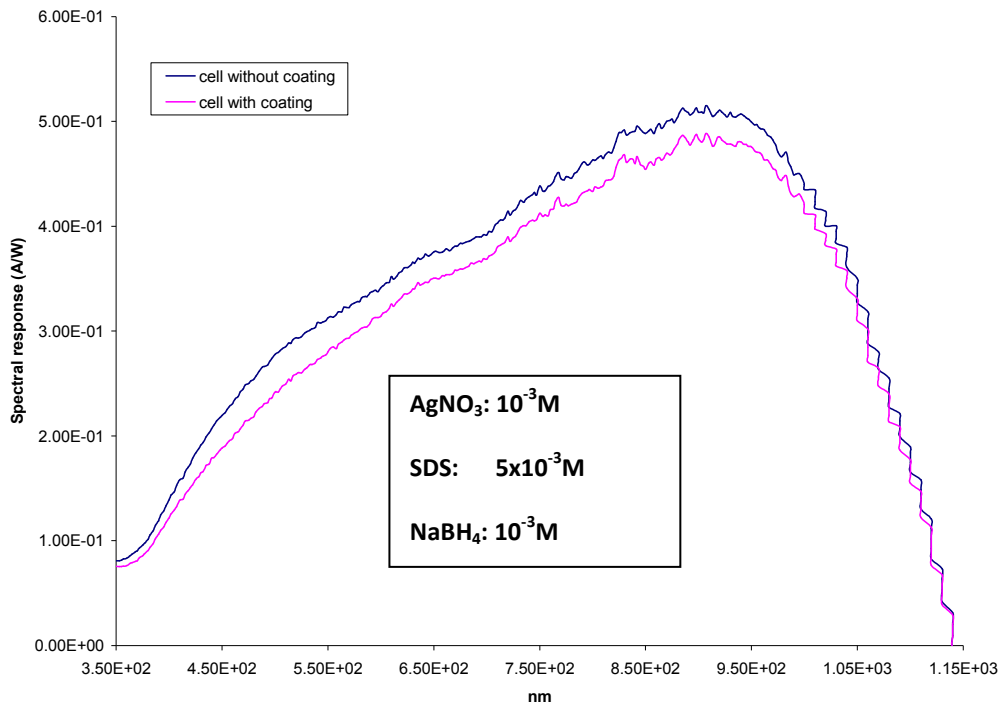


Figure 4.16: spectral response measurements of Si solar cell coated with silver NPs (here NPs were used after centrifugation of one time)

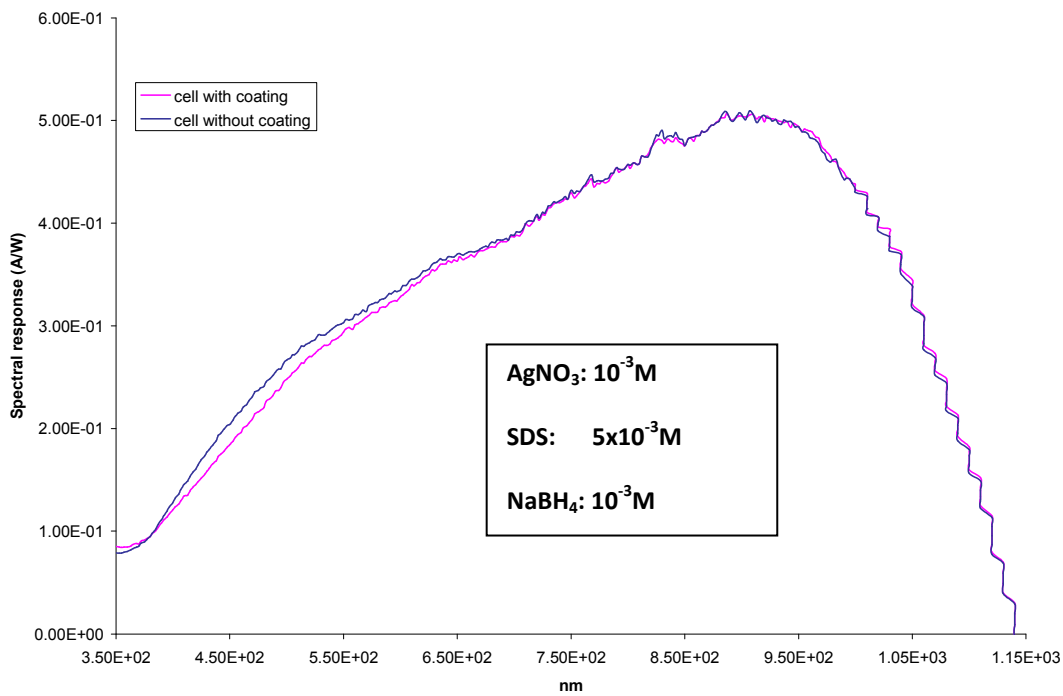


Figure 4.17: spectral response measurements of Si solar cell coated with silver NPs (here NPs were used after centrifugation of three times)

Spectral response of the same cell using NPs centrifuged three times is reported in Figure 4.17. There is only slight decrease of spectral response in SPRF and vicinity of SPRF where NPs absorb light well. The SPRF (red profile which is corresponding to the NPs used on cell) of NPs is about 480 nm. The absorption of light by the NPs dominates on the scattering which is much expected in our application. Also the size of the NPs is an important factor for PLS process. The particles sizes are 50-60 nm obtained from the SEM image shown in Figure 4.14. The particle dimensions obtained might be not sufficient to take part the PLS process. The typical sizes should be around 100 nm for best scattering efficiency by the silver metal NPs.

It is clear that the method used to prepare silver NPs is not effective for our aim. Thus we followed another method for the preparation of colloidal solution. The details of new method are discussed in the following sections.

4.3.3 Results on colloidal silver NPs prepared with Method B

As we did not observe any enhancement of spectral response of Si solar cells due to silver NPs synthesized by means of above described process, we followed new preparation method using polymer as a stabilizing agent for the synthesis of silver NPs. Polymer itself acts as an embedded matrix as well as capping agent of NPs. Polymer capping could be also a way to avoid oxidation problem of silver NP.

4.3.3.1 UV-VIS results of silver NPs embedded in polymer

The deep yellow color of the colloidal solutions is the preliminary indication for the formation of silver NPs, respectively. The transmission spectra of silver particles deposited on glass substrates followed by drying in hot furnace reported in Figure 4.18 provide further evidences of the formation silver NPs [79] NPs. Plasmon resonance is observed with peak resonance wavelength of 418 nm for silver particles. Substrate dried in hot furnace shows better transmittance than the substrate dried in air. This can be explained by possible polymer shrinkage during thermal treatment which causes a decrease of average spacing between silver particles.

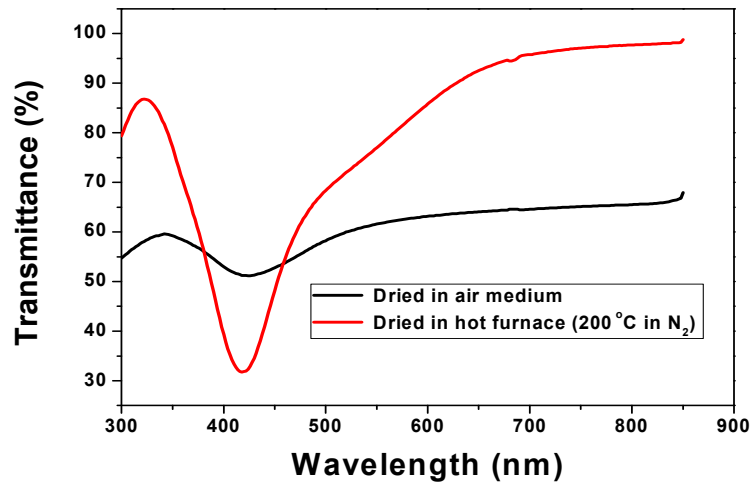


Figure 4.18: Transmittance profile of PDDA protected silver NPs dried in air and in hot furnace

4.3.3.2 SEM analysis of PDDA embedded colloidal silver NPs

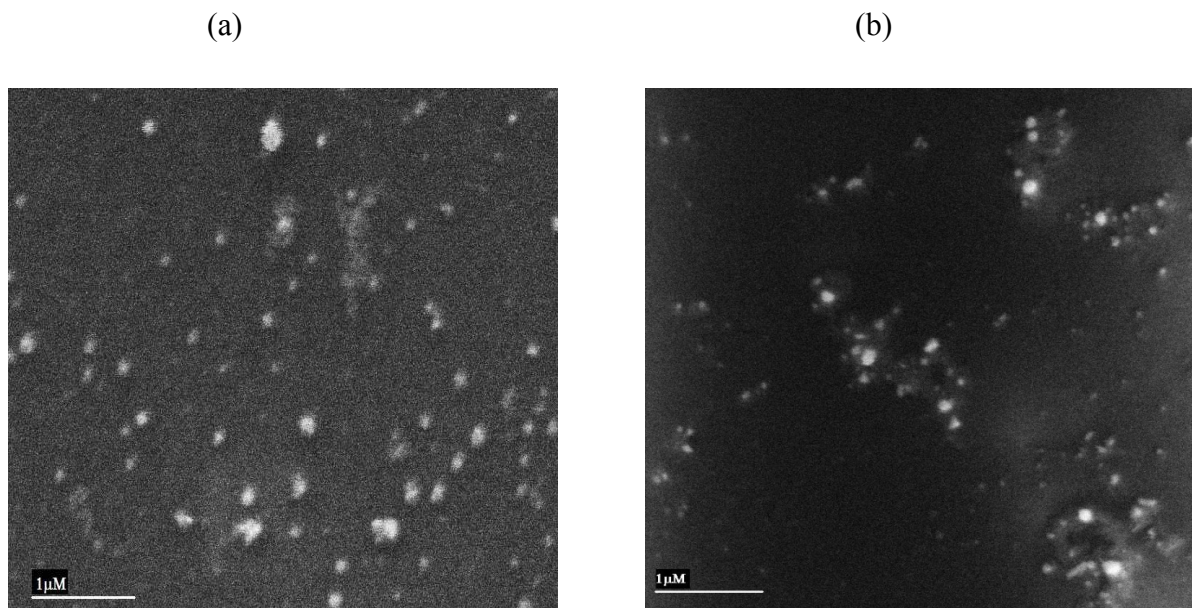


Figure 4.19 SEM image of silver particle dried in (a) air medium (b) hot furnace

SEM images of silver NPs on Si dried in different medium are shown in Figure 4.19 (a) and Figure 4.19 (b), respectively. It is apparent that silver NPs on the substrate surface are not homogeneously distributed and different particle sizes (70-140 nm) are observed. But substrate dried in hot furnace shows some aggregation of particles. This is probably related to PDDA shrinkage with the temperature. However the particle dimension is in the range suitable for reaching maximum radiative efficiency [37].

4.3.3.3 Spectral response of different Si solar cells with and without silver NPs prepared with method B

Spectral responses in terms of EQE of the different Si solar cell coated with silver NPs are shown in Figure 4.20. External Quantum Efficiency (EQE) measurements were carried out by the spectral response (SR) technique described in section 3.5 of chapter. Figure 4.20a and Figure 4.20b show EQE curves of both NOARC and ARC cell coated with silver NPs. An overall significant increase in EQE throughout the visible to near-IR region is observed for both cells. From Figure 4.20 it could be also observed that the enhancement is minimum around the resonance wavelength called SPRF (418 nm shown in Figure 4.18), in good agreement with the literature [29]. At this wavelength, absorption of light dominates over scattering and no enhancement is observed since absorption cross-sections of metal NPs are larger than scattering cross-sections. At higher wavelength this enhancement is significant due to dominance of scattering over absorption of light.

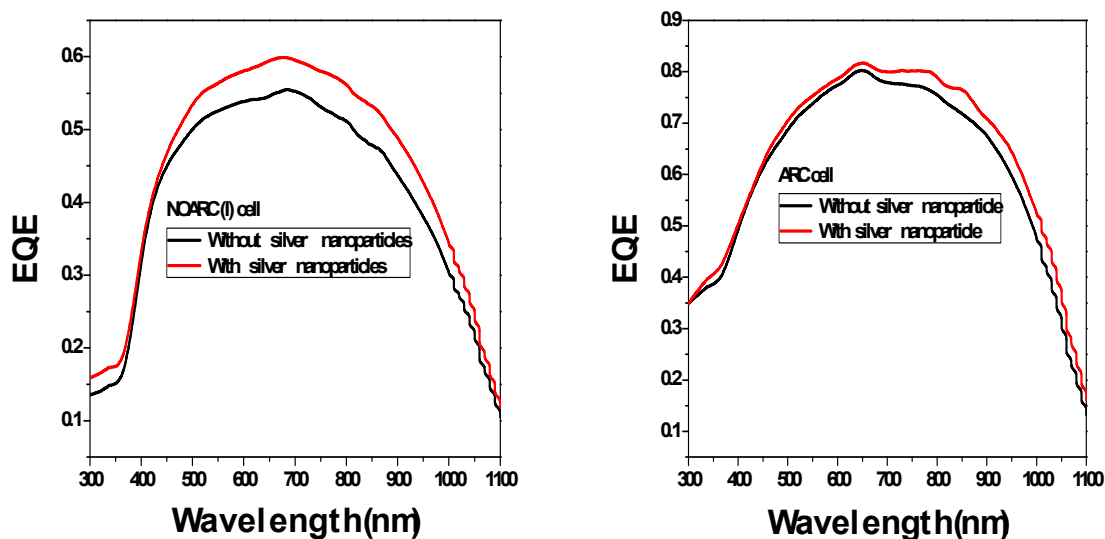


Figure 4.20: Spectral response of (a) ARC (b) NOARC cell both without and with silver NPs prepared by Method B (For each sample, at least ten EQE measurements were performed by varying the spot position on the front surface of the cell. The standard deviation of such measurements is 1.3% in the range between 300 and 450 nm and 5% between 450 and 1100 nm.)

Above the resonance wavelength [37], scattering efficiency of silver NPs reaches the maximum and then shows an almost constant value as shown in Figure 4.20. From literature [24] survey we found the enhancement of photocurrent of Si solar cell is possible due both light scattering and near field enhancement by metal NPs. As Near field enhancement is possible for minimum interparticle

separation [80] and SEM images [Figure 4.19(b)] showed that that silver NPs on the device surface are not homogeneously distributed we can deduce that for silver NPs the enhancement can be ascribed to light scattering of the NPs.

4.3.3.4 I-V results of different NOARC cells with and without silver NPs prepared with method B

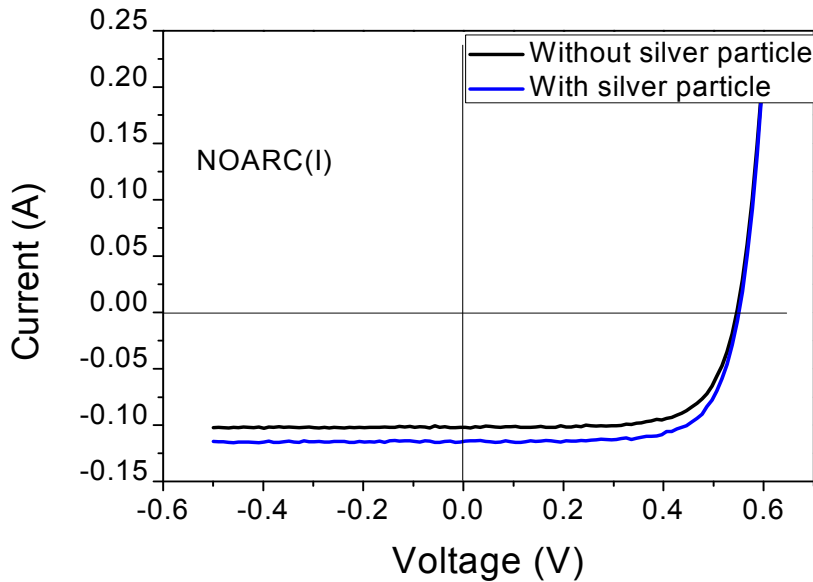


Figure 4.21: I-V measurement of NOARC cell before and after deposition of silver NPs prepared by Method B

Figure 4.21 shows I-V curve measured under A.M. 1.5 irradiation on NOARC cells covered with silver NPs. A clear increase of the short circuit current (I_{sc}) is attributed in the presence of silver NPs on NOARC cells. Table (4.2) shows different parameters of Si solar cell obtained from I-V measurements. The parameters of Si solar cells were obtained before and after deposition of silver NPs on the respective cells. The mean value and experimental errors of parameters obtained from twenty I-V measurements of each cell are also included with this table.

Table (4.2): Change in parameters obtained from I-V measurements of different cells with and without silver NPs

Sample_NOARC 1						
	Efficiency		Relative Enhancement (%)	Max delivered power (P_{max})		Relative Enhancement (%)
	Without silver NPs	With silver NPs		Without silver NPs	With silver NPs	
Mean	8.5	9.1	7±0.3	38	40.9	7.6±0.3
Sample_NOARC 2						
	Efficiency		Relative Enhancement (%)	Max delivered power (P_{max})		Relative Enhancement (%)
	Without silver NPs	With silver NPs		Without silver NPs	With silver NPs	
Mean	8.2	8.9	8.5±0.3	37.5	40.4	7.7±0.3
Sample_ARC S2						
	Efficiency		Relative Enhancement (%)	Max delivered power (P_{max})		Relative Enhancement (%)
	Without silver NPs	With silver NPs		Without silver NPs	With silver NPs	
Mean	13.4	13.7	2.3±0.3	68.3	68.8	0.7±0.3
Sample_ARC S5						
	Efficiency		Relative Enhancement (%)	Max delivered power (P_{max})		Relative Enhancement (%)
	Without silver NPs	With silver NPs		Without silver NPs	With silver NPs	
Mean	13.5	13.7	1.5±0.3	68	68.8	1.2±0.3
Sample_ARC S14						
	Efficiency		Relative Enhancement (%)	Max delivered power (P_{max})		Relative Enhancement (%)
	Without silver NPs	With silver NPs		Without silver NPs	With silver NPs	
Mean	13.7	13.8	0.7±0.3	68.8	69.2	0.6±0.3

In agreement with EQE results, I-V measurements under A.M.1.5 irradiation showed a strong relative enhancement of overall efficiency (around 8.5%) for NOARC cells, while in ARC cells this value is around 2.3%. This can be explained taking into account that in NOARC cells the silver particles scatter light directly in proximity of Si resulting in more efficient light coupling into the substrate. According to Ref. [38], the fraction of scattered light by the metal NPs into the substrate varies for different particle shapes and efficient light coupling into the substrate is possible for decreasing average separation between the particles and substrate. For NPs on Si without SiN_x , the

energy from the excited resonance is directed preferentially towards the high refractive index surface, which confines the light into the Si layer [81]. This increases the path length of light in Si and hence the probability of absorption. The lower EQE enhancement in the ARC cell might also be attributed to interference effect between light that is transmitted through anti-reflection coating (SiN_x) to the textured Si interface and light that is scattered by the NPs [70].

4.3.3.5 Reflectance measurement of bare Si substrate coated with and without silver NPs prepared with method B

A clear experimental evidence of the effect of metal NPs on reflectance of bare Si substrate is shown in Figure 4.22. The reflectance spectrum of bare Si without metal NPs is in agreement with that reported in literature [82], while a strong reduction of reflectance in the whole wavelength range after deposition of metal NPs on the properly cleaned silicon substrate was observed. The reduction of reflectance is due to combination of forward scattering and absorption by metal NPs. The large reduction of reflectance is observed in the region where metal NPs absorb the light very well.

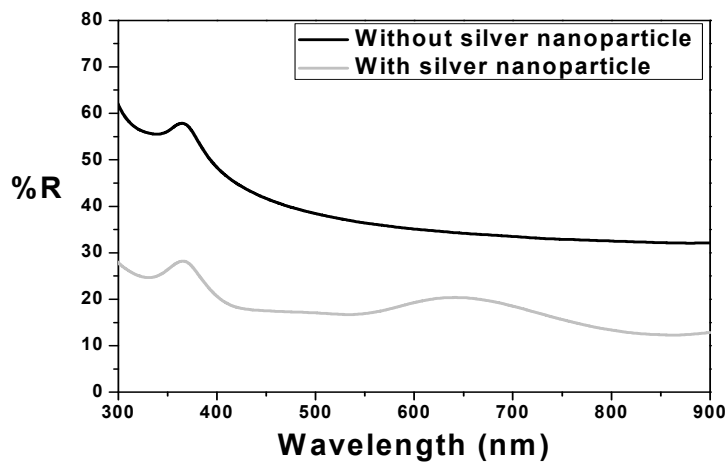


Figure 4.22: Reflectance measurement of bare Si substrate with and without silver NPs

4.3.4 Results on gold NPs prepared with colloidal solution method

4.3.4.1 Transmittance measurement of colloidal gold particle solution

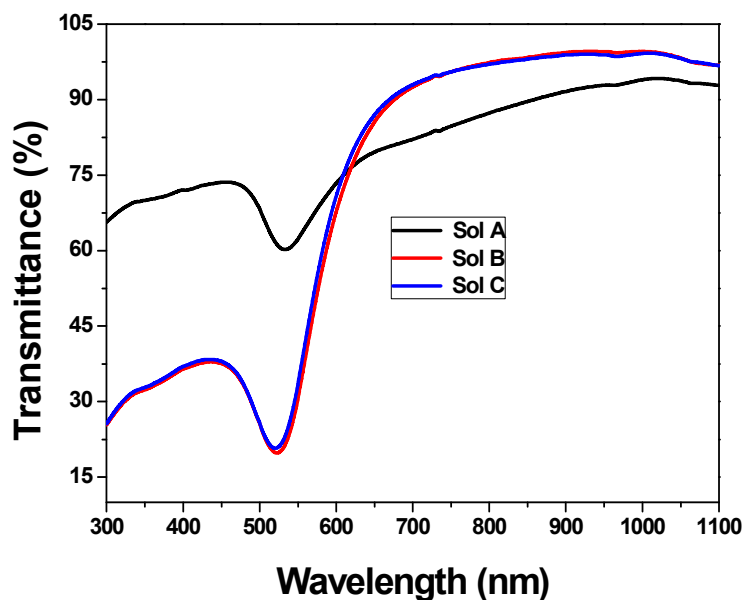


Figure 4.23: Transmittance profile of different gold NPs solution

Transmittance profile of different gold solutions is depicted as in Figure 4.23. The difference between various solutions of gold NPs is described in the section 4.2.4. It is apparent that there is no such change of transmittance behavior between gold particle solutions B and C. But there is significant difference of transmittance profile between solution A with other solutions (solution B & solution C). Also the red shift of Plasmon Resonance peak of solution A is ascribed. The peak resonance wavelength of solution A is monitored at 532 nm whereas; the same is monitored at 521 nm for other two solutions. Surface Plasmon resonance wavelength is decreased of with reducing the amount of citrate solution.

4.3.4.2 SEM analysis of colloidal gold particles deposited on Si substrate

Typical SEM images of the gold NPs prepared with different amount of trisodium citrate solution are shown in Figure 4.24. Figure 4.24(a) shows that gold particles are homogeneously distributed with particle diameter around 70 nm while in Figure 4.24(b) particles are smaller size (~ 47 nm) with little agglomeration. Figure 4.24(a) corresponds to the gold NPs prepared with highest amount (10 ml) of citrate solution while Figure 4.24(b) is related with the gold NPs synthesized with 6ml citrate solution. However it is fact that particles sizes are of different dimension in the two figures. From the two figures one can see that with increasing particle sizes with increasing the amount of

the reducing reagent. Thus the amount of citrate solution determines the size of the NPs. The faster the capping of the gold NPs by the citrate in hot aqueous solution is resulting smaller the NPs shown in SEM images of Figure 4.24.

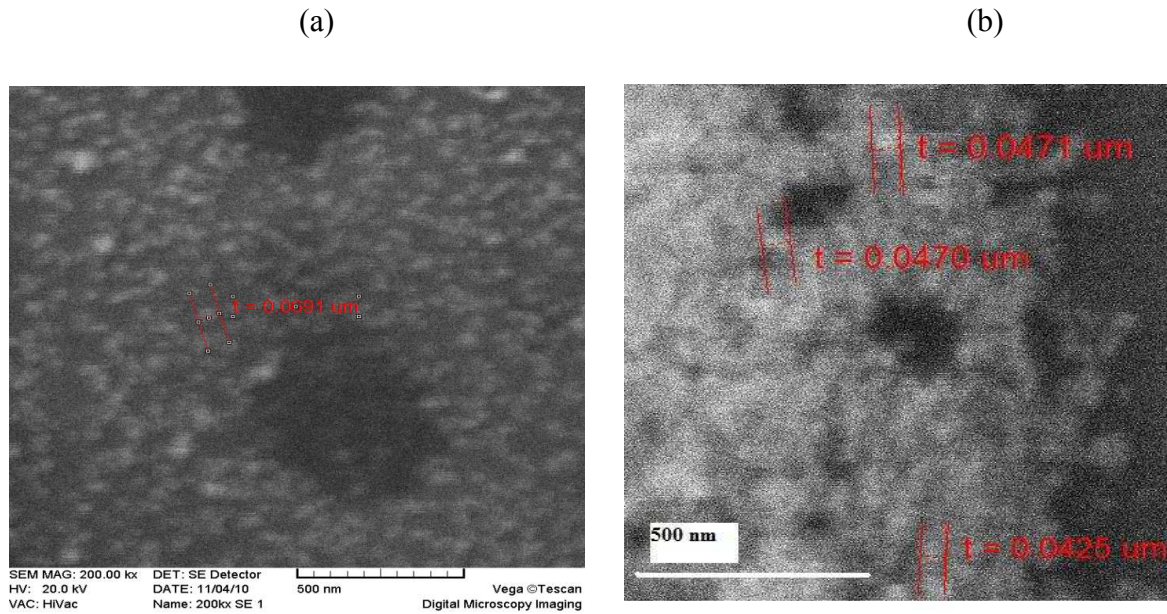
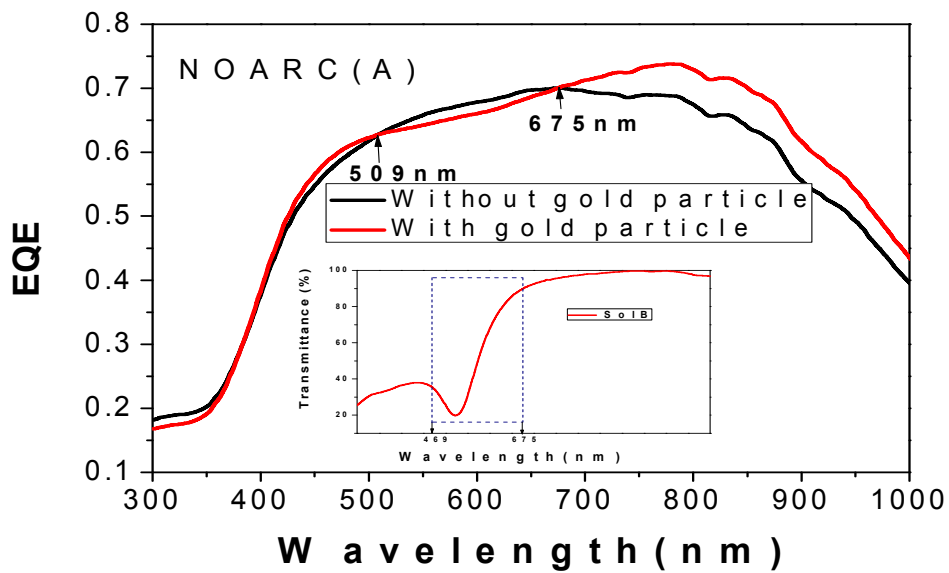
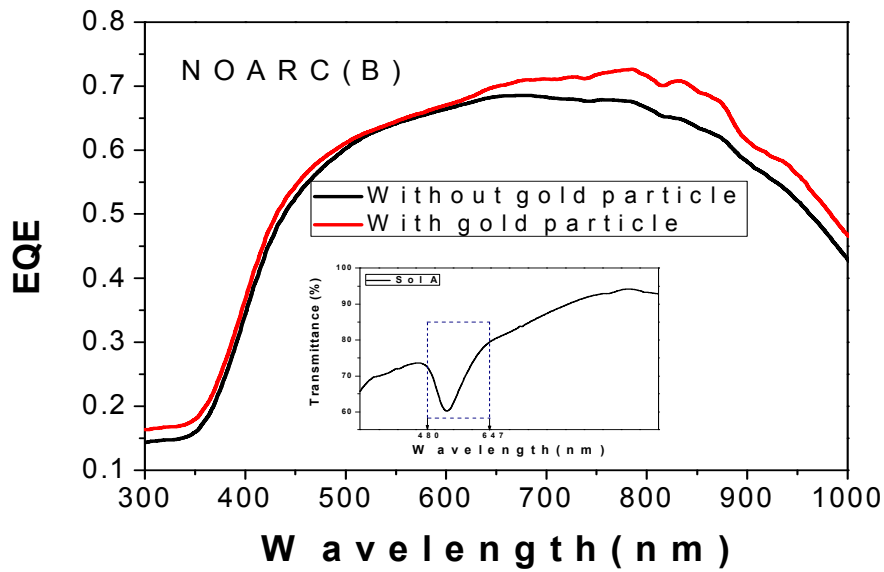


Figure 4.24: SEM image of gold NPs of (a) solution A (b) solution B

4.3.4.3 Spectral response analysis of NOARC cells coated with and without gold NPs



(a)



(b)

Figure 4.25 EQE curves of NOARC cells using gold NPs of (a) solution B (b) solution A (For each sample, at least ten EQE measurements were performed by varying the spot position on the front surface of the cell. The standard deviation of such measurements is 1.3% in the range between 300 and 450 nm and 5% between 450 and 1100 nm.)

EQE measurements are depicted of different NOARC cells coated with gold NPs shown in Figure 4.25a and Figure 4.25b. In both the figures, there is also clear enhancement of EQE monitored above the peak resonance wavelength (521 nm) of gold NPs. Below this resonance wavelength practically no enhancement is observed due to the lower radiative efficiency by the gold NPs as per Figure 4.1 shown in the introduction section. Lower radiative efficiency can be due to the fact of lower scattering efficiency by the NPs in this region. The absorption by NPs dominates over scattering in this region. There is a slight decrease of EQE around the resonance wavelength (from 509 nm to 675 nm) of NOARC (A). For better clarification we put the transmittance plot in the inset of Figure 4.25. Dashed portion of the two figures shows the maximum absorption by the metal NPs respectively. The decrease of the EQE (marked region of Figure 4.25) due to the metal NPs is consistent with the dashed region of the transmittance profile [shown in the inset of Figure 4.25].

In Figure 4.26, there is a strong decrease of EQE observed in ARC cell coated with gold NPs. A strong decrease of EQE, around the resonance wavelength of gold NP could be due to an interference effect between light that is transmitted through anti-reflection coating (SiN_x) to the textured Si interface and light that is scattered by the NPs [70]. But it is known [37] that silver particle has higher scattering efficiency than the gold particle. Hence, less light scattering (by the gold NPs) is also lost due to interference effect. We observed a lower EQE enhancement of on

ARC cell coated with silver NPs whereas a strong decrease of EQE observed in the ARC cell coated with gold NPs. Gold NP has lower radiative efficiency than silver NPs, so there effects on ARC cell are different. This the reason for the decrease of EQE in the visible region on ARC cells due to gold NPs.

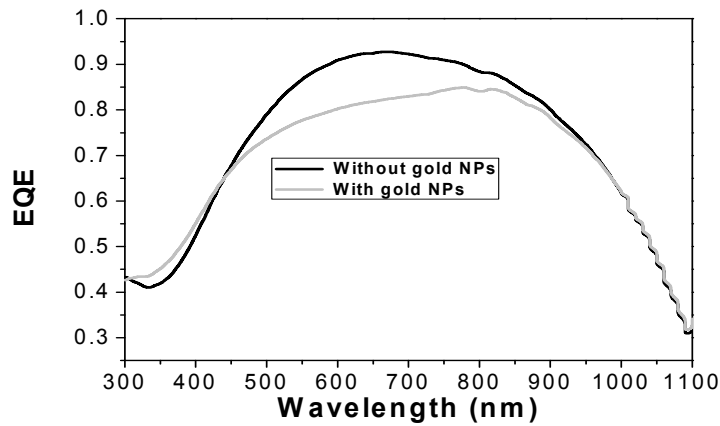


Figure 4.26: EQE curve of ARC cell without and with gold NPs coating

4.3.4.4 I-V measurements on NOARC cell with and without gold NPs

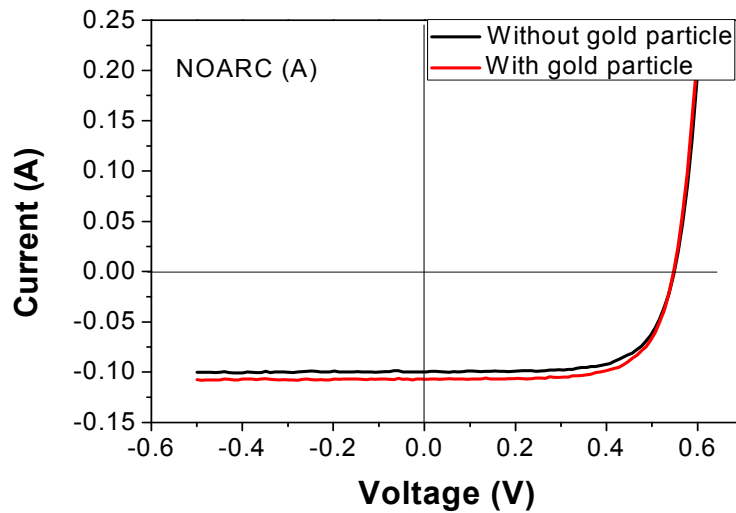


Figure 4.27: I-V measurements of NOARC cell coated with gold NPs

I-V measurements on NOARC cells coated with gold NPs (Figure 4.27) showing a relative I_{sc} enhancement around 6.1%, Table (4.3) demonstrates the enhancement of the important parameters of different solar cells coated with gold NPs. Standard deviations along with the measurements errors are also included with this table. From the same table it is observed maximum relative

enhancement around 7.6% after one time deposition of colloidal gold solution on the NOARC cells. It was also monitored of device performance with LBL deposition (more than one time deposition on same cell) on NOARC cells. The enhancement of each step is shown in table [4.4(a)] and table [4.4(b)]. The maximum enhancement is observed after two times deposition of gold NPs on NOARC cell. It could be expected better surface coverage of NPs after multi-deposition of NPs on the same cell.

Table (4.3): Change in parameters obtained from I-V measurements of different cells with and without gold NPs

Sample_NOARC_2						
	Efficiency		Relative Enhancement (%)	Max delivered power (P_{max})		Relative Enhancement (%)
	Without gold NPs	With gold NPs		Without gold NPs	With gold NPs	
Mean	8.6	8.7	1.2±0.3	34.5	34.8	0.9±0.3
Sample_NOARC_A						
	Efficiency		Relative Enhancement (%)	Max delivered power (P_{max})		Relative Enhancement (%)
	Without gold NPs	With gold NPs		Without gold NPs	With gold NPs	
Mean	10.5	11.2	6.6±0.4	37.1	39.4	6.2±0.4
Sample_NOARC_B						
	Efficiency		Relative Enhancement (%)	Max delivered power (P_{max})		Relative Enhancement (%)
	Without gold NPs	With gold NPs		Without gold NPs	With gold NPs	
Mean	9.2	9.9	7.6±0.4	42.6	46.4	8.8±0.4

Table [4.4(A)]

Sample_NOARC_5							
Efficiency							
	Without gold NPs	With gold NPs (1time)	Relative Enhancement (%)	With gold NPs (2 time)	Relative Enhancement (%)	With gold NPs (3 time)	Relative Enhancement (%)
Mean	8.6	9.2	6.9±0.4	9.3	8.1±0.4	9.2	7.7±0.4

Table [4.4(B)]

Sample_NOARC_5							
Maximum delivered power (P_{max})							
	Without gold NPs	With gold NPs (1time)	Relative Enhancement (%)	With gold NPs (2 time)	Relative Enhancement (%)	With gold NPs (3 time)	Relative Enhancement (%)
Mean	39.7	42.1	6±0.4	42.2	6.3±0.4	42.3	6.5±0.4

4.3.5 Impact of oxidation on the device performance

As we know silver is best choice in the PLS process among the other metal NPs due to its higher scattering efficiency. It is well known that silver NPs oxidize readily when they come into contact with air or moisture and that the oxidation process can affect the enhancement of PV properties. The possible oxidation of silver NPs could affect the enhancement of PV properties. Since we have no experimental evidences to support such hypothesis on the oxidation effect, hence we repeated the same experiments with noble metal NPs like gold and compare it with silver NPs results obtained. Therefore we synthesized gold NPs in colloidal method followed by deposition of such colloidal NPs on both MC-Si cells. But it has been observed that EQE enhancement on Si cells due to gold NPs is closed to the enhancement due to silver NPs, even if silver showed the best scattering efficiency. So most probably some oxidation of silver NPs can affect on the EQE enhancement on both Si cells coated with them.

4.3.6 Investigation of light scattering effect due to metal NPs on CIGS thin film solar cells

We observed that light scattering due to both metal NPs (silver and gold) works on Si solar cell very well. Although, the effect of both NPs on the NOARC is better than ARC cells observed. Also better device performance was ascribed due to silver metal NPs. Now we want to investigate the effect of same NPs on the most popular thin film solar cells like CuInGaSe₂ (CIGS).

Before describing the experimental work related to the light scattering effect of metal NPs on CIGS thin film solar cells, it should be convenient to discuss the fundamentals of the CIGS solar cells.

4.3.6.1 Principle of operation of CIGS solar cells

The basic component of CIGS solar cells is the Cu(In,Ga)Se₂ absorber layer, where the band gap can be varied by varying the [Ga]/ [In] concentration ratio. The theoretical maximum efficiencies for single junction cells can be achieved with band gaps between 1.1 and 1.5 eV for AM1.5 global irradiation [83]. For thin film cells, polycrystalline, slightly Cu deficient, extrinsic p-type doping is obtained. An n-type semiconductor film, called “buffer” layer on the top of the CIGS absorber is required to establish an electric field at the p-n junction (depletion or space-charge region). When electrons are photoexcited within the space charge region, they are transported to the n-side owing to the electric field and thus generate an electric current. When photon absorption takes place in the quasi-neutral region of the absorber, the photoexcited electrons diffuse and may arrive at the space charge region at some stage, whereupon they are again swept across the p-n junction. Of course, some of the photoexcited electrons will be lost for the current generation owing to recombination in the space-charge or in the quasi neutral region, especially if the photoexcitation takes place far away from the junction. Ideally buffer layer exhibits a much higher carrier density than the absorber, such that most of the space charge region extends into the absorber and thus carrier collection is improved. In addition, the band gap of the buffer layer should be wide, such that most of the incoming radiation can be transmitted to the absorber. Owing to the exponential decrease in light intensity caused by absorption, the incident photons are then absorbed predominantly in the front part of the absorber, ideally within the depletion region.

The schematic representation of a CIGS solar cell structure is depicted in Figure 4.28. the CIGS layer was grown by a hybrid-sputtering growth process. A detail about the growth process and cell preparation was reported in [84]

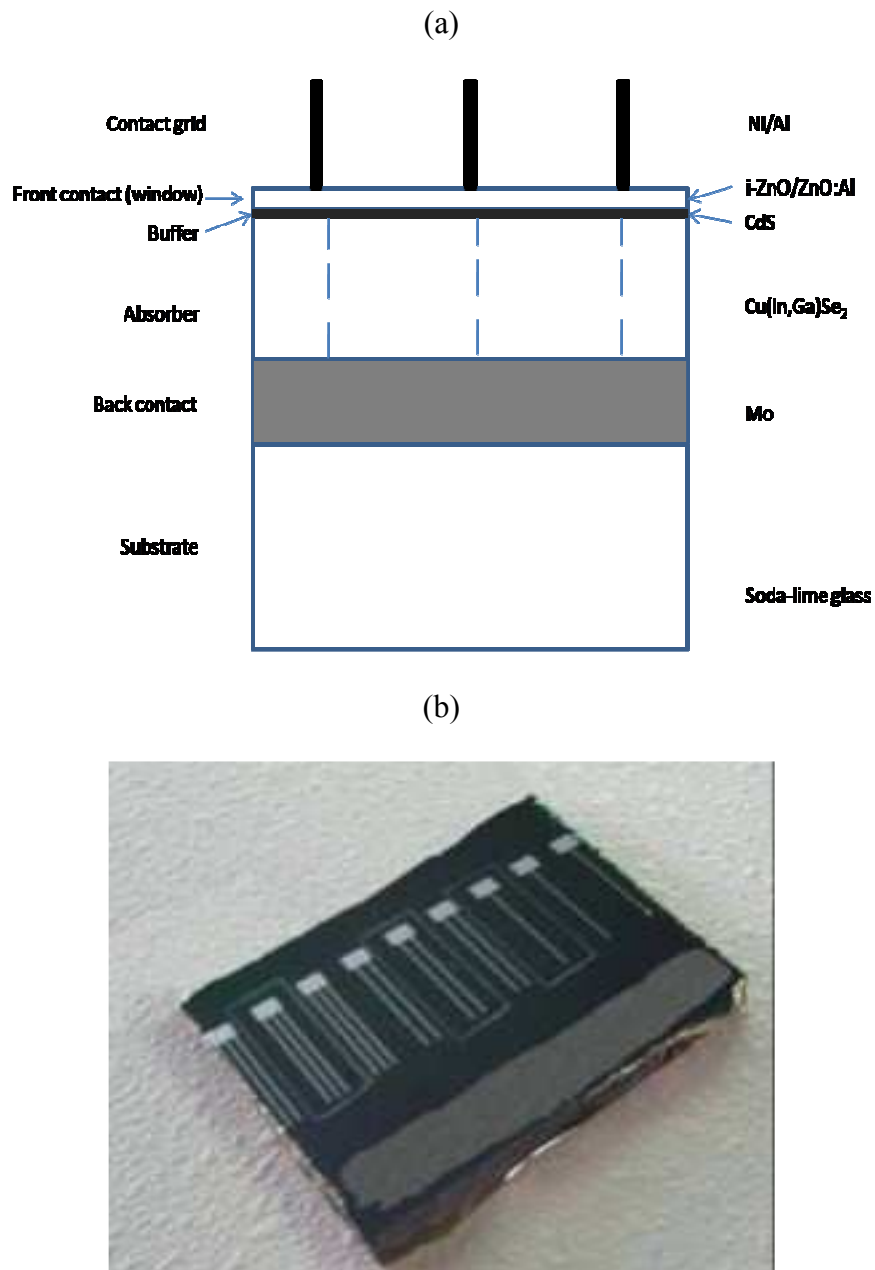


Figure 4.28: (a) Schematic representation of a CIGS solar cell structure (b) CIGS cells used in our experiments

4.3.6.2 Deposition of colloidal NPs (both silver and gold) on CIGS solar cells

Before deposition of colloidal NPs, CIGS cells were masked very well in order to avoid contact related problem during the electrical measurements. Colloidal NPs was deposited by putting a drop of colloidal solution in small area of the cell (as shown in Figure 4.28(b)). The typical cell area is 1.7 cm^2 . The drying procedure of the NPs coated CIGS cells was followed same as described in the case of Si solar cells.

4.3.6.3 Spectral response of CIGS cells with and without NPs (both silver and gold)

The possible effect on the spectral response due to silver and gold NPs has been investigated on CIGS cells. We have also further investigated of PLS on CIGS cells due to metal NPs. The spectral response of CIGS cells are shown in the Figure 4.29 and Figure 4.30. A better spectral response can be achieved due to PLS and that can be verified by the spectral response of CIGS coated with metal NPs. The improvement of spectral response of CIGS cells are shown in the red line of both Figure 4.29 and Figure 4.30.

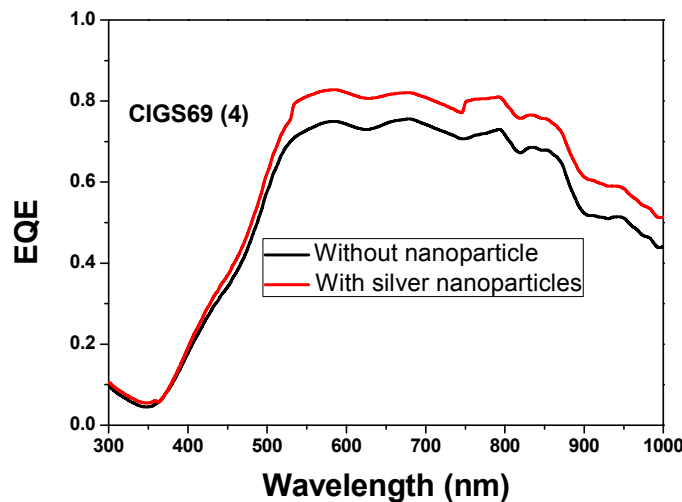


Figure 4.29: Spectral response of CIGS cells coated without and with silver NPs (*For each sample, at least three EQE measurements were performed by varying the spot position on the front surface of the cell. The measurements error is 1.51% in the range between 300 and 450 nm and 2.66% between 450 and 1100 nm*)

From the above figures (Figures 4.29 and Figure 4.30), it is clearly observed the enhancement of EQE due to both silver and gold NPs. Also it is cleared that the enhancement due to silver NPs is much better than that of gold NPs and in agreement with that obtained in Si solar cells.

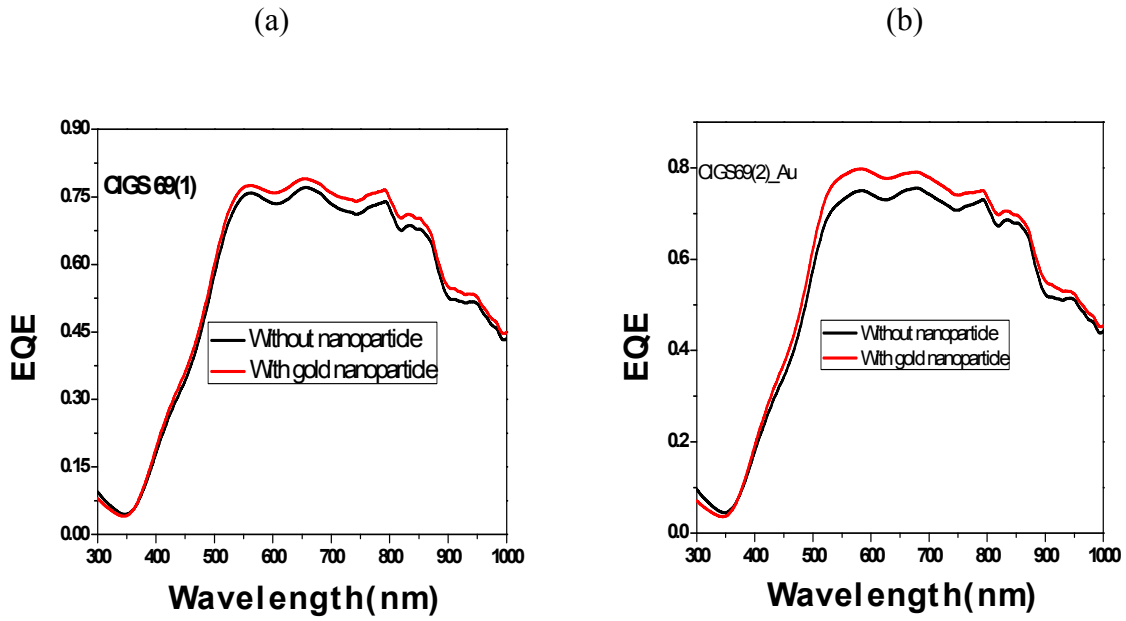


Figure 4.30 (a) & (b): EQE measurements of CIGS cells coated without and with gold NPs (*For each sample, at least three EQE measurements were performed by varying the spot position on the front surface of the cell. The measurements error is 1.58% in the range between 300 and 450 nm and 2.47% between 450 and 1100 nm*)

Chapter 5

*Down-Shifting Effect by Semiconductor
Nanocrystals on Si solar cells*

5.1 Introduction

Colloidal semiconductor nanocrystals (NCs) or quantum dots (QDs) have attracted much attention with their unique properties such as their size tunable emission, their continuous absorption in UV region. The optical properties of NCs evolve dramatically with their size, an effect known as quantum confinement. Figure 5.1 illustrates the effect of quantum confinement effect on electronic states going from 3D bulk materials from 0D QDs. As the size of the QDs smaller than material's Bohr exciton radius, the continuous density of states in the bulk collapse into discrete electronic states. QDs are considered "artificial atoms" for precisely this reason. After series of approximations, the quantum dot problem can be reduced to "Particle-In-a-Box" model. From this model, it is easy to deduce that the carriers are confined leading to the higher band gap energy and correspondingly the blue shift of photoluminescence.

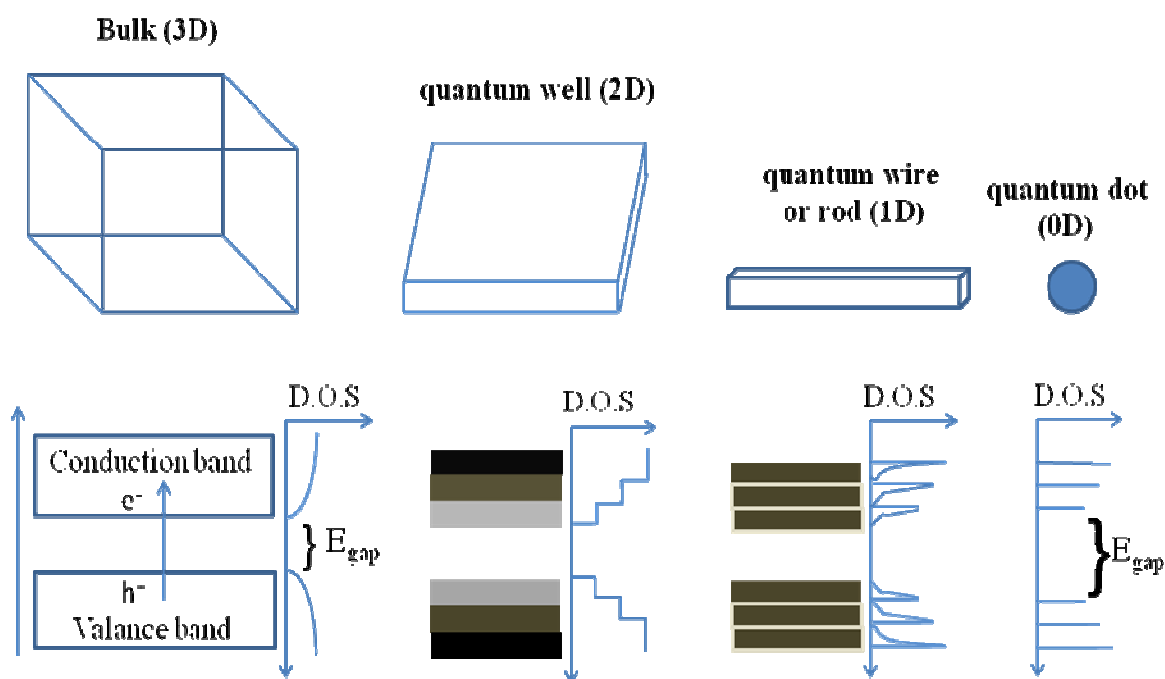


Figure 5.1: Illustration of quantum confinement going from 3D bulk semiconductor to 2D quantum wells to 1D quantum wires and finally to 0D quantum dots.

Such NCs have great interest in recent times because of their new and unusual structural, electronic and optical properties. Size dependent luminescent semiconducting NCs (or nanophosphors) have attracted much attention due to their practical applications: optical coatings, field effect transistors, photoconductors, optical sensors, electroluminescent materials and other light emitting materials [85-87]. NCs based on different metal chalcogenides such as ZnS, CdS, (CdSe)ZnS core shell

structures and their doped system have shown interesting phenomenon such as size induced visible light emission, photo-blinking effects, electroluminescence, and efficient low voltage cathode luminescence. These properties have opened up number of new areas of applications for these materials such as DNA markers, bio sensors, light emitting diodes, lasers. Among these new class of luminescent materials, ZnS:Mn NCs have been extensively studied particularly for their radiative lifetime shortening and enhanced emission efficiencies [88]. Furthermore ZnS is non toxic among the other available NCs. Doping ion acts as recombination centers for the excited electron-hole pairs and result in strong and characteristic luminescence. In doped NCs, the luminescence quantum efficiency is expected to increase as a result of a greater overlap between the electron and the hole of the host semiconductor material with the localized dopant levels. Another advantage is that the band gap of the semiconductor NCs can be tuned easily with respect to the bulk band gap [89]. This allows tuning of the excitation energy given to the host semiconductor to emit through the dopant levels. Also, it is possible to change the dopant-emission wavelength by changing the size of the NCs as discussed in the case of $Zn_{1-x}Eu_xS$ [90]. The greater overlap between the host and dopant wave functions in a NC compared to the bulk material leads to an enhancement in the luminescence intensity due to an enhanced transfer between the host and dopant levels.

Synthesis of NCs can be possible by different methods such as physical methods and chemical methods etc. Physical methods like molecular beam epitaxy, ionised cluster beam, liquid metal ion source, consolidation, and sputtering are much sophisticated and costly. Chemical precipitation in presence of capping agents, reaction in micro emulsion technique, sol gel reaction and autocombustion are commonly used techniques for synthesis of NCs [91]. Also size and shape of the NCs can be easily tuned in chemical methods with low cost compared to physical methods.

In this chapter we shall concentrate on the synthesis and characterization of Mn^{2+} doped ZnS NCs using chemical capping method. Also we want to investigate the effect doping concentration on the band gap as well as on luminescence property. At last, we would like to illustrate the down shifting concept due to Mn^{2+} doped ZnS NCs on Si solar cell. In this concept, both emission wavelength and maximum emission intensity of NCs will play an important role for the device performance

5.2 Experimental

In this section it will be illustrated the synthesis procedure of both undoped and doped ZnS NCs. Furthermore, it will also be described the cleaning procedure of NCs followed by the deposition procedure of NCs on Si solar cells.

In the typical synthesis procedure [92] of ZnS NCs several steps was carried out in the whole process. The conventional setup used for the synthesis of NCs is shown in Figure 5.2.

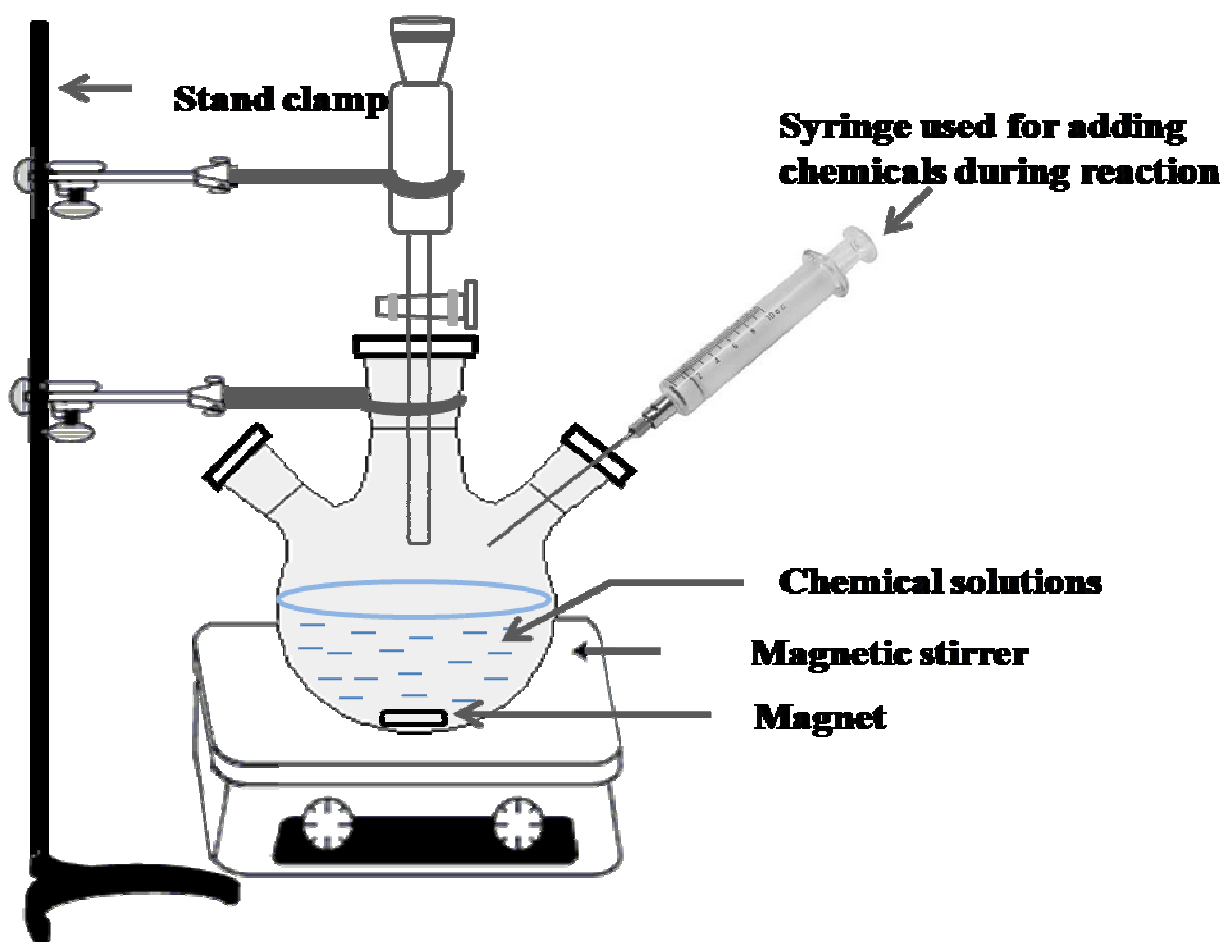


Figure 5.2: Setup for the synthesis of NCs

Chemicals: Mercapto Ethanol (ME) [C₂H₅OSH], zinc chloride [ZnCl₂], manganese chloride [MnCl₂], sodium sulphide [Na₂S·9H₂O] and dimethyl formamide (DMF), were supplied by Sigma-Aldrich.

5.2.1 Preparation method of ZnS NCs

In the first step, 5 mM of ZnCl₂ was dissolved in 40 ml of DMF and continuously stirred with a magnetic stirrer for 10 min. In the second step, 10 mM of ME in 5ml of DI water was added to the previous mixture under stirring condition in air. This mixture was kept under same stirring condition for another 10 min. In the third step, 4.2 mM of aqueous solution of Na₂S (3.8 ml) was slowly added drop wise into the above solution under stirring. Once added, the color of the above

solution turned white immediately. Then, the reaction was carried out for 8 hours at room temperature under same condition.

5.2.2 Preparation method of Mn doped ZnS NCs

In the typical procedure, 5 mM of ZnCl₂ in 56 ml of DMF and 2 mM of MnCl₂ in 5 ml of deionised (DI) water (20.3MΩ-cm) was continuously stirred for 10 min. In the second step, 10 mM of ME in 5ml of DI water was added to the previous mixture under stirring condition in air. In the third step, 4.2 mM of Na₂S which was dissolved in 3.8 ml DI water, was slowly added drop wise into the above solution under same condition. The molar ratio between the total amount of salt and sulphur was controlled to be 10:4 and the weight ratio between DMF and water was maintained as 70:17. Once added, the color of the above solution turned white immediately. Then, the reaction was carried out for 8 hours at room temperature.

Finally ZnS and doped ZnS NCs were ultrasonicated for half an hour followed by centrifugation with 10000 r.p.m. Then the resulting solutions were washed with several times with DI water. Then the resulting solutions were diluted twenty times with DI water for further measurements. Powder samples were thus prepared by drying in air after centrifugation of aqueous samples.

5.2.3 Deposition method of doped ZnS NCs on Si solar cells

We performed different deposition method of NCs on solar cell in order to investigate the down shifting effect on the same cells. NCs are first deposited on different cells by putting some drops on it and keep it some hours for drying in air medium. Spectral response and I-V measurements were done on such NCs coated cells.

5.2.4 Preparation method of NC doped polymer composite film

NCs-polymer composite film has been deposited to the cell surface to obtain better device performance. To this purpose, 1.5% (wt) Poly-Methayl Methacrylate (PMMA) solutions were prepared in toluene and 2mg of dried (powder) samples were dissolved into the resulting PMMA solution under ultrasonication. We also prepared NCs doped Ethylene Vinyl Acetate (EVA) composite in same way. Dichloromethane was used as the solvent for 1.5% (wt) of EVA dissolved. Thin layer of polymer-NCs solutions were deposited on properly cleaned quartz substrates by a spin coater with constant speed of 1000 r.p.m for 25 seconds. Then this substrate was put on the cell like a sandwich structure as shown in Figure 5.3. The reason to use this configuration was to analyse the results of the same cell without and with NCs in polymeric matrix.

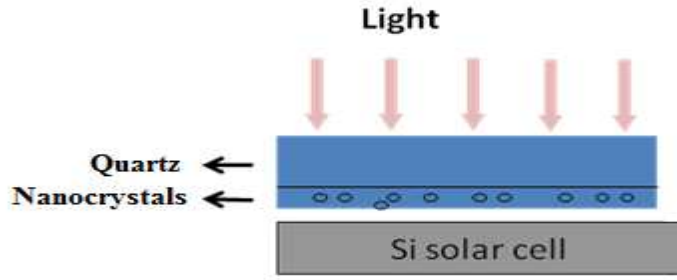


Figure 5.3: NCs- PMMA composite film on Si solar cell

Spectral response measurements as well as I-V measurements were done on this sandwiched structure before and after deposition of NCs.

5.3 Results and discussion

5.3.1 UV-VIS absorption analysis of both pure and Mn doped ZnS NCs

We measured UV-Vis absorption spectrum of pure ZnS and $Zn_{1-x}Mn_xS$ NCs see in Figure 5.4.

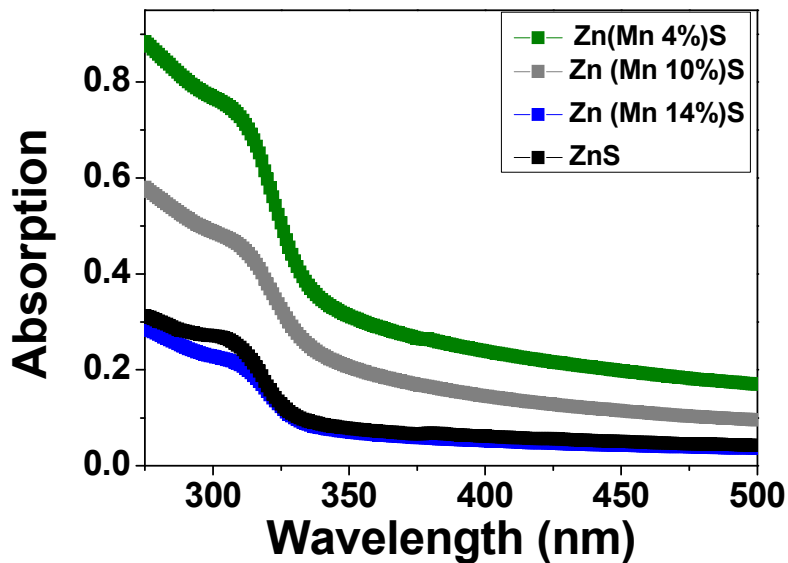


Figure 5.4: UV-Vis absorption spectra (carried out on solution) of pure and doped ZnS NCs with different Mn concentration

An intense peak is noticed at 305 nm for ZnS whereas; this value moves from 307 to 310 nm for $Zn_{1-x}Mn_xS$ depending upon the doping concentration, while absorption characteristic peak of ZnS bulk material appears at 340 nm [92]. The blue shift of the absorption peak of the NCs from that of bulk is due to the quantum confinement effect of the small sized NCs. The band gap of NCs were estimated NCs through absorption spectrum of it. Direct band gap of the samples is evaluated by

plotting $(\alpha h\nu)^2$ against $h\nu$ [93] shown in Figure 5.5. The detail of the band gap estimation of these NCs is described in [93]. The obtained band gap of the samples is blue shifted in compared to the band gap (3.67 eV) of bulk ZnS due to their quantum confinement effect [8]. The band gap energy of the ZnS and Zn_{1-x}Mn_xS NCs is found (A) 3.74 eV (B) 3.69 eV (Mn: 4%) (C) 3.7 eV (Mn: 10%) & (D) 3.76 eV (Mn: 14%) respectively. For our explanation we will use the name of the samples (A), (B), (C), & (D) respectively accordingly as mentioned in above.

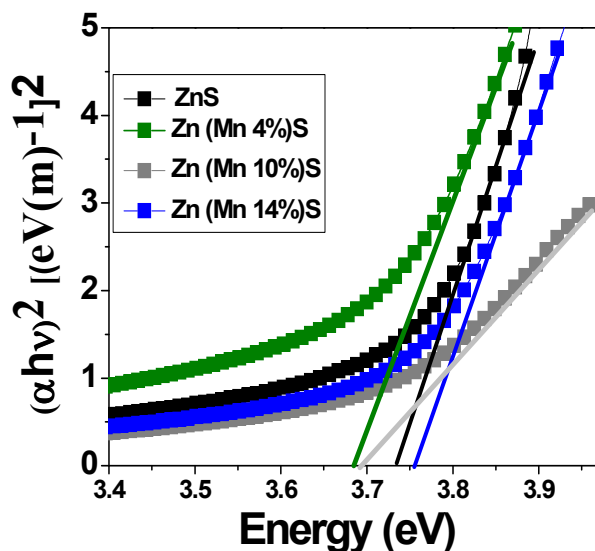


Figure 5.5: The plots of $(\alpha h\nu)^2$ versus $h\nu$ for the pure ZnS and the Mn-doped ZnS NCs

The mean value of the band gap estimated from each fitting as function of concentration of Mn is shown in Figure 5.6. The standard deviation was calculated 0.4 to 0.7% for each fitting for the band gap measurement. In this figure, it is shown that at lower percent of doping of ZnS shows lower band gap compared to pure ZnS NCs but its band gap value increases with doping concentration.

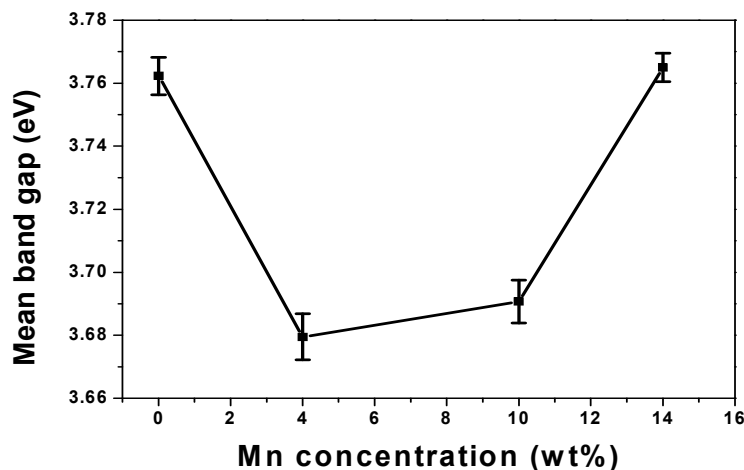


Figure 5.6: The variation of mean band gap as a function of Mn concentration.

It has been reported [94] in the case of ZnO that upon Mn doping in ZnO the band gap reduces for the lower concentration of doping and for higher concentration of doping band gap increases, which is similar to our results. For higher concentration of Mn band gap may increase on the basis of virtual crystal approximation [94] because of the formation of MnS. Consequently the decrease of band gap at lower concentration due to the Mn doping has been ascribed due to the exchange interaction between transition metal ions (Mn) and the s and p electron of the host band [95].

5.3.2 TEM and EDX analysis of both pure and Mn doped ZnS NCs

The particle sizes and chemical analysis of both pure and doped NCs were done by TEM followed by EDX measurements. In the following figures, TEM images of different NCs are reported.

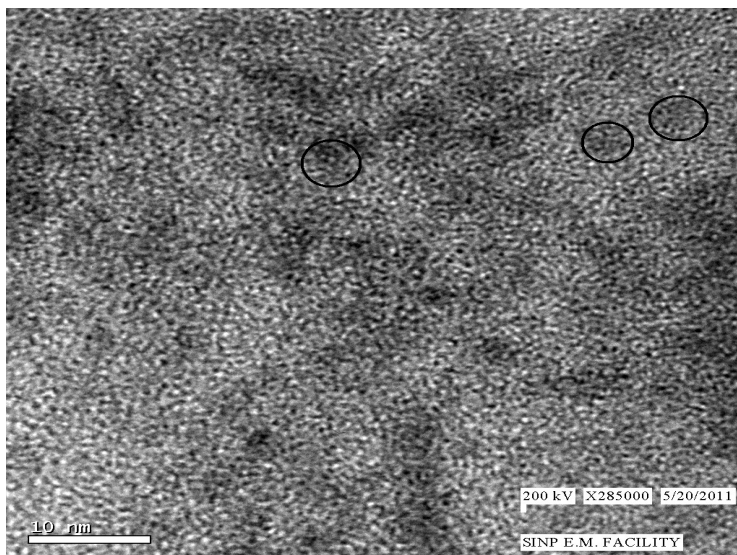


Figure 5.7: TEM image of pure ZnS NCs

TEM image of of pure ZnS NCs is shown in the Figure 5.7. The NCs are not clearly observed in this image. This sample is not a good quality for TEM observation because of some other chemical elements might be present in the sample due to improper cleaning of this NC sample after synthesis. For better clarification the NCs are encircled and in these spots the EDX analysis was done.

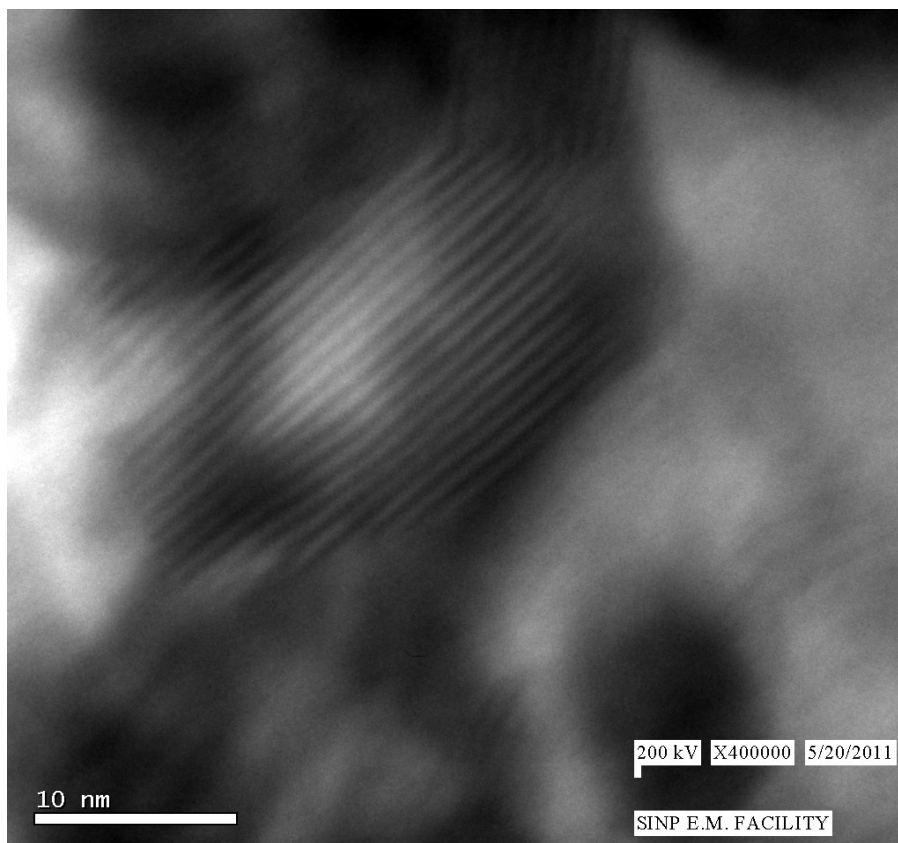


Figure 5.8: TEM image of 4% Mn doped ZnS NCs

The TEM image of 4% Mn doped ZnS NCs is demonstrated in Figure 5.8. It is observed that the NCs are agglomerated and clearly seen the lattice spacing of 0.45nm. But it is impossible to determine the size of the NCs. Figure 5.9 exhibits the TEM analysis of ZnS NCs doped with 10% Mn. Here it is also observed the NCs are agglomerated and HRTEM image of this type of NCs is shown in the inset of Figure 5.9. The lattice fringes are observed in the inset image. The sizes of the NCs are $4\text{nm} \pm 0.5 \text{ nm}$. In Figure 5.10, same consideration is appropriate for ZnS NCs doped with 14% Mn.

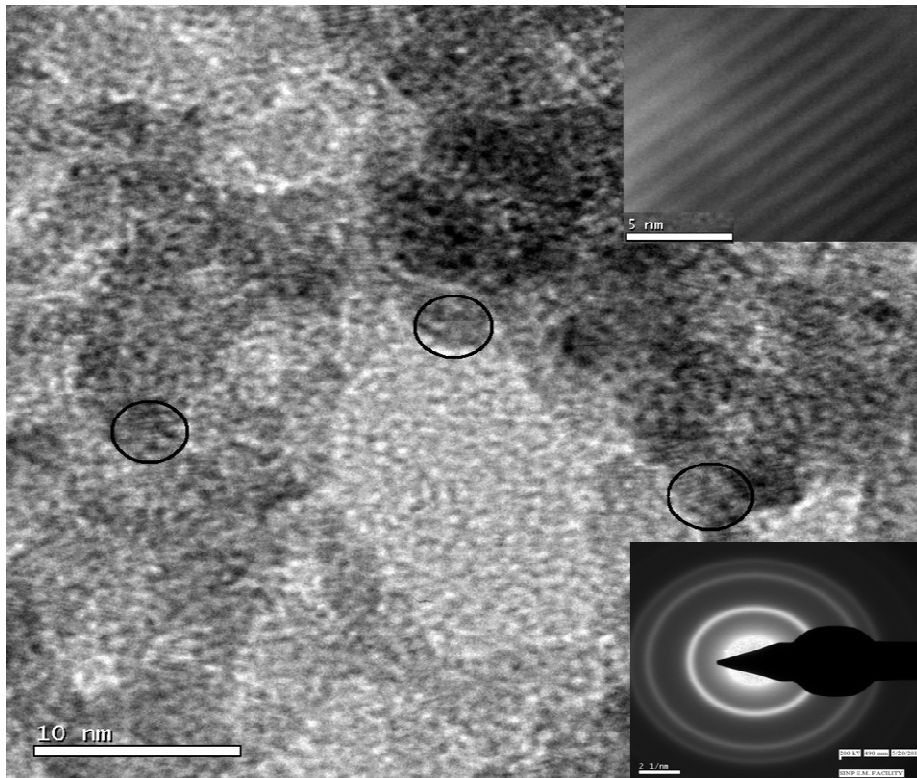


Figure 5.9: TEM image of 10 % Mn doped ZnS NCs

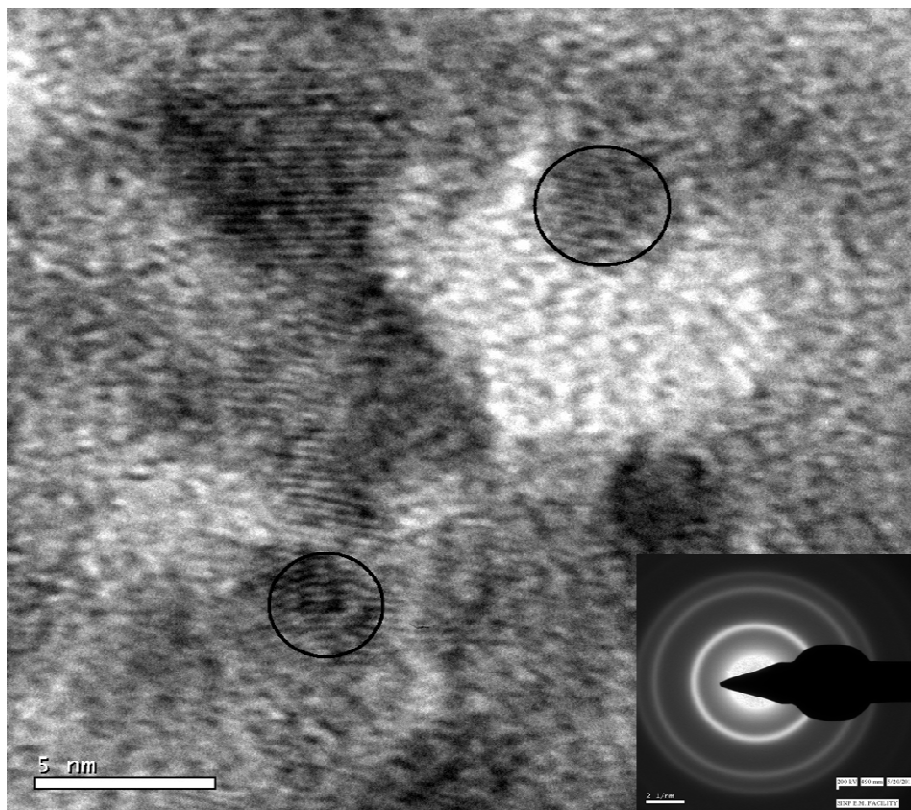


Figure 5.10: TEM image of 14% Mn doped ZnS NCs

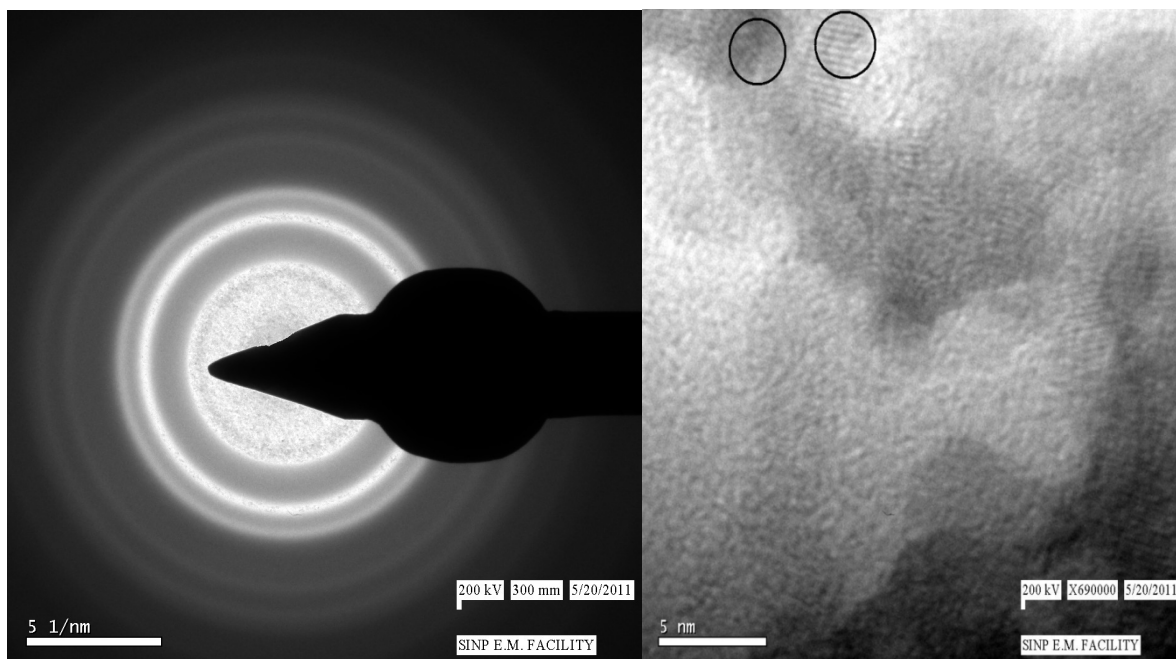


Figure 5.11: SAED pattern of doped ZnS NCs

The Selected Area Electron Diffraction (SAED) pattern was measured for the sample C as shown in Figure 5.11. The brighter three rings corresponding to the electron diffraction from the three planes (111), (2 2 0), and (311) as mentioned in the literature [96]

The EDX measurements of the four types of NC are shown the following figures (from Figure 5.12(a) to Figure 5.12(d)). It can be observed that for all types of NC there is an excess of sulphur present in the NC's surfaces. The excess sulphur comes from organic encapsulate which surrounded the NCs prepared in the above mentioned synthesis process.

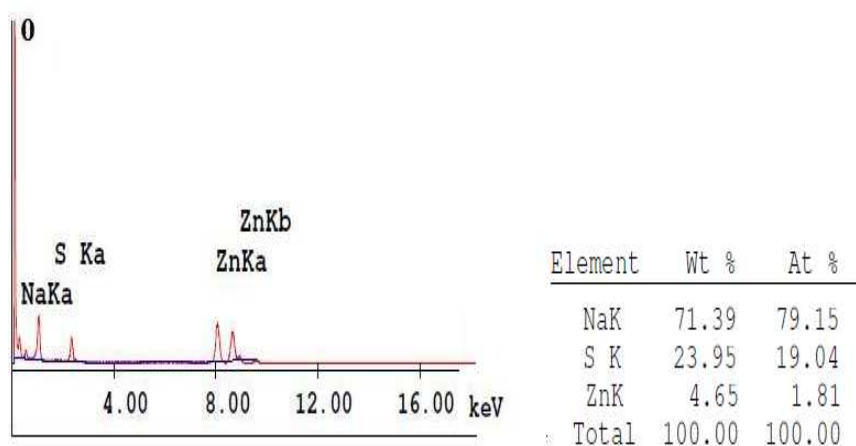


Figure 5.12(a): EDX analysis of pure ZnS

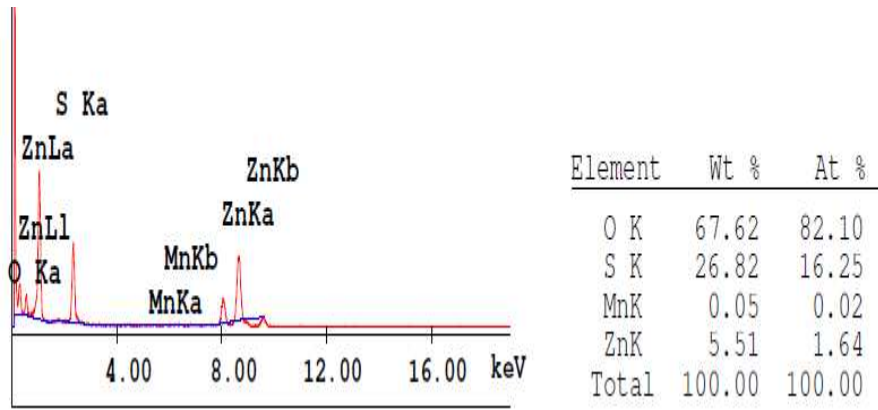


Figure 5.12-b: EDX analysis of Zn(Mn:4%)S

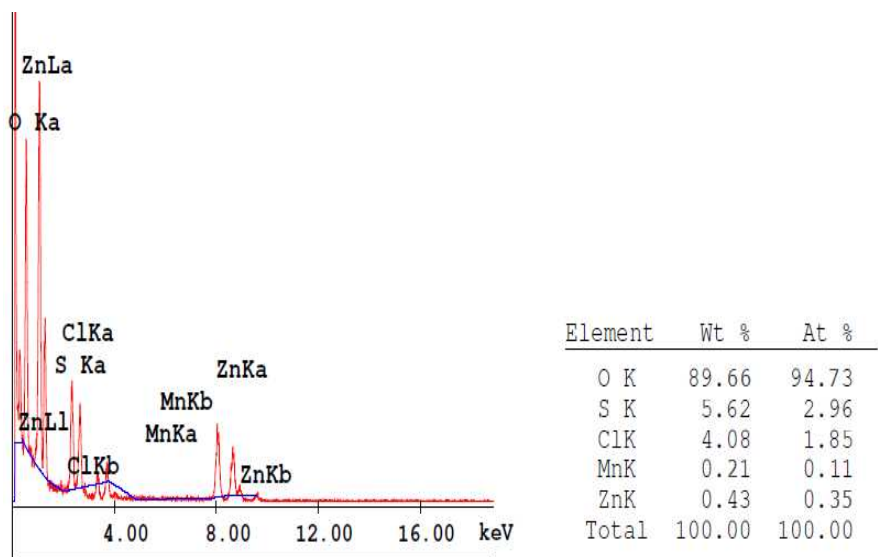


Figure 5.12-c: EDX analysis of Zn(Mn:10%)S

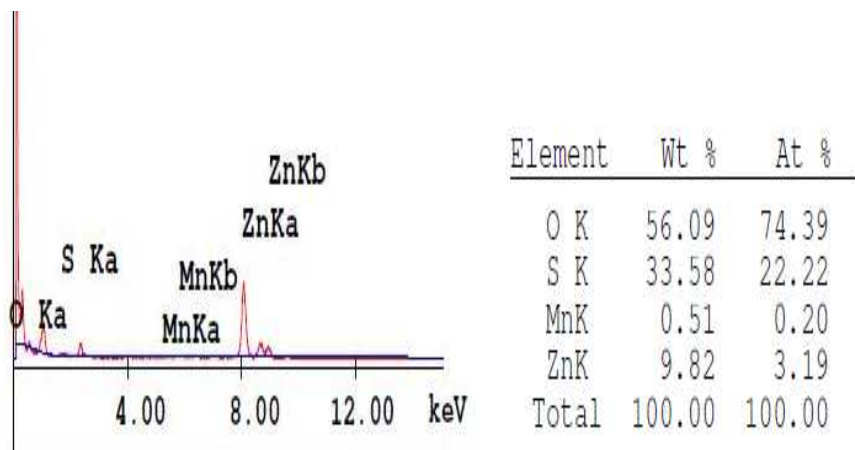


Figure 5.12-d: EDX analysis of Zn(Mn:14%)S

The proposed [92] mechanism of Mercapto Ethanol capped ZnS NC is depicted in Figure 5.13. In all EDX analysis shown above, there is no peak due to Mn observed and it is probably due to the

out of detection limit (1%) of EDX. Also it can be noticed in all elemental analysis that Mn content is less than 1% for all the doped samples. In synthesis process, we used more than 1% Mn for all the samples. But it is observed that Mn is less than 1%. This can be explained by considering the difficulties of substitution of Mn^{2+} into the interstitial sites of ZnS. Since ionic radius of Mn^{2+} is 10% larger than that of Zn^{2+} [85].

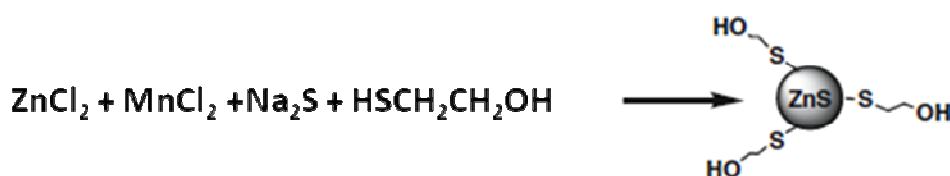


Figure 5.13: Chemical reaction of Mn doped ZnS NCs formation

The large oxygen peak could be possible of ME capped ZnS NCs and these excess oxygen comes from ME as shown in Figure 5.13. Higher amount of oxygen can also be attributed due to adsorption on the NCs prepared in air medium.

5.3.3 Photoluminescence analysis of both pure and Mn doped ZnS NCs

(a) Photoluminescence of pure ZnS

The room temperature PL spectra of the ZnS and Mn doped ZnS NCs are depicted in the following section. Figure 5.14 shows the typical PL emission spectra of pure ZnS NCs. The spectrum was recorded at the excitation wavelength of 320 nm with an emission in the range of 350-620 nm. For all the samples, the blue emission ranging from 400 -500 nm can be ascribed to defects states of ZnS NCs. The asymmetric curve implies superposition of multiple emission bands. Gaussian curve fitting applied to de-convolute the emission band suggests the presence of three emission bands with peak positions at 402, 431 and 464 nm of pure ZnS NCs shown in the inset of Figure 5.14. In undoped NCs, the possible emission centers are related to either surface/lattice defects or native impurities [97]. With low concentration of sulphide ions during precipitation, ZnS formed will have larger number of sulphur vacancies (V_S) which can act as doubly ionized donor centres. Possibly, V_S acts as common electron trap below the conduction band (CB) edge and the hole traps such as cation vacancies (V_{Zn}), surface states (SS), impurity centers [97] (e.g. Zn), etc., are different for different emissions as schematically shown in inset of Figure 5.14. The e-h recombination at the acceptor centers leads to V_S -related multiple emissions in ZnS NCs [98].

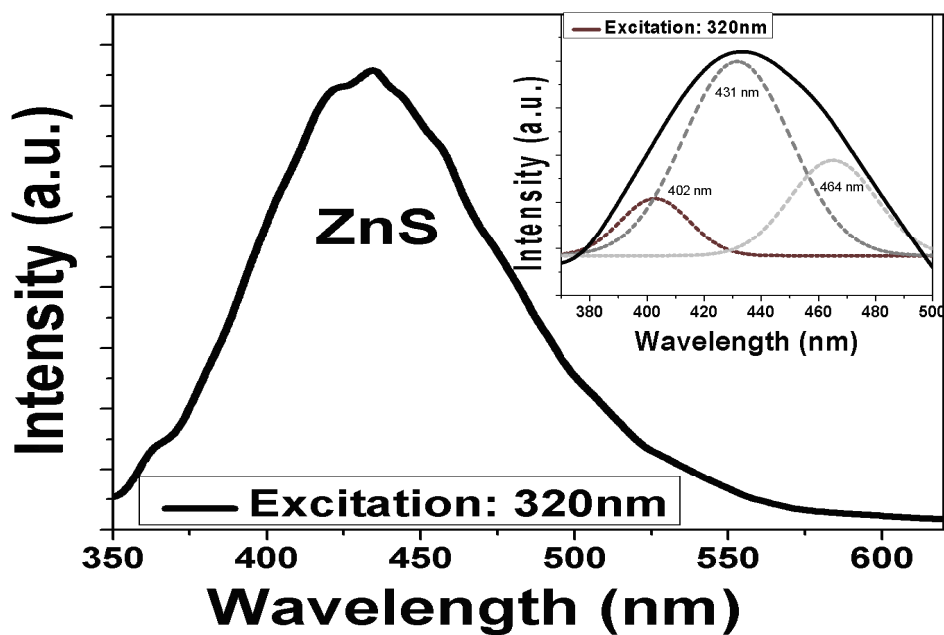


Figure 5.14: Photoluminescence of pure ZnS NCs and in the inset deconvolution of blue emission plot with different emission peaks (the peaks are due to Zn vacancies, surface states and background impurity center)

(b) Photoluminescence of Mn doped ZnS NCs (or Role of Mn on the emission property)

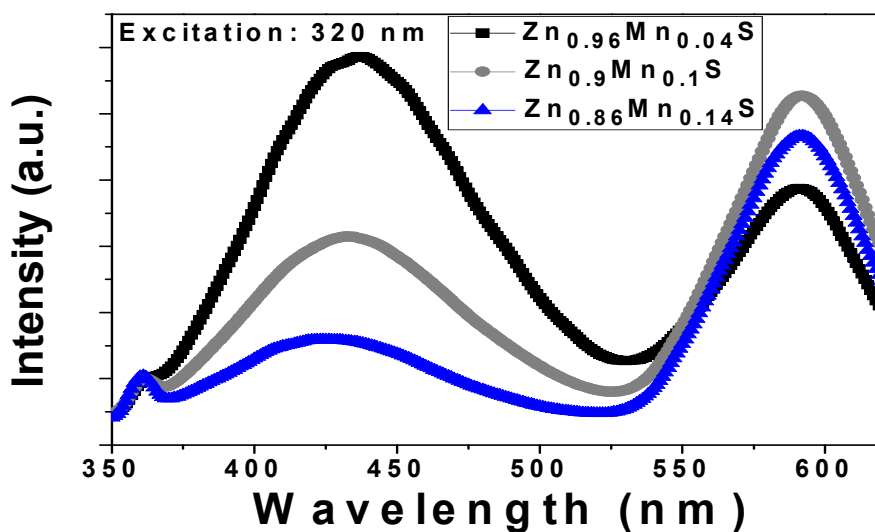


Figure 5.15: PL spectra under the 320 nm excitation wavelength for the ZnS NCs doped with different Mn dopant concentrations

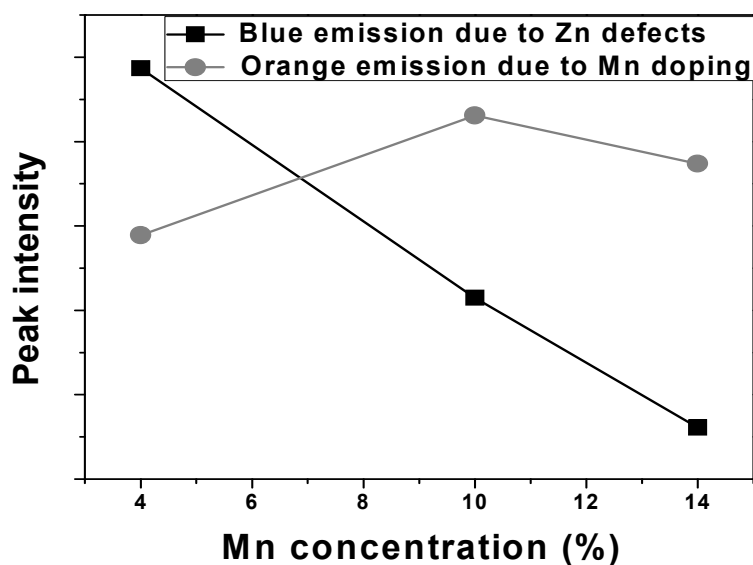


Figure 5.16: Emission intensity as a function of Mn concentration

The emission spectra of doped ZnS NCs with different doping concentration are demonstrated in Figure 5.15. The yellow orange emission, centered 592 nm can be observed in Figure 5.15 which is associated with the ${}^4T_1-{}^6A_1$ transition within 3d shell of Mn^{2+} . The yellow orange emission can be due to efficient energy transfer from the ZnS host to Mn^{2+} ions facilitated by the mixed electronic states. When Mn^{2+} ions are incorporated into ZnS lattice and substitute for the cation sites, there is a mixing between the s-p electrons of the host ZnS and the d electrons of Mn^{2+} occurs resulting the transition between ${}^4T_1-{}^6A_1$ [85]. The maximum peak intensity of the blue and orange band emissions is plotted as a function of the manganese amount shown in Figure 5.16. The sample without Mn^{2+} shows only blue photoluminescence. As soon as Mn^{2+} is incorporated into the ZnS NCs, the intensity of the blue emission decreases and the Mn^{2+} emission comes up, since the energy transfer between ZnS host and Mn^{2+} impurity is very efficient. At lower concentration of Mn^{2+} , the blue emission peak dominates over the orange emission peak and it gradually decreases with the increase of Mn^{2+} concentration. The luminescence intensity of the orange band increases with Mn^{2+} concentration and then decreases. The slight decrease of orange emission peak may be caused by the Mn-Mn interaction [85]. The maximum of intensity value is reached at about 10% Mn^{2+} optimum ratio between the number of the emission centers and the quenching ones. The blue band intensity decreases continuously with the increase of Mn^{2+} amount, due to the decrease of the numbers of self activated centers related with the lattice defects of the zinc. Also there is blue shift of the blue emission peak attributed with the increase of Mn concentration. The energy level of doped ZnS is shown in Figure 5.17.

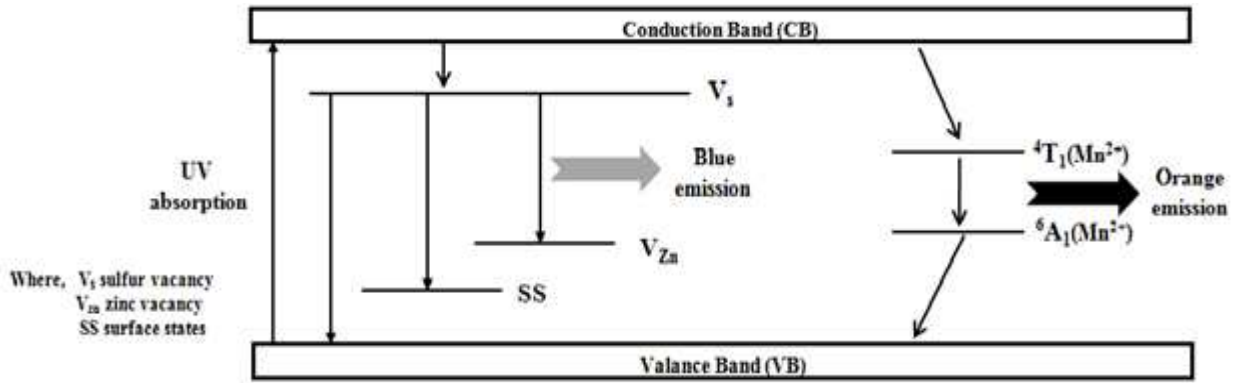


Figure 5.17: Schematic for the decay of electrons via different channels in Mn doped ZnS NCs

Based on the PL analysis, ZnS NCs with 10% Mn doped shows maximum orange emission intensity compare with that of other NCs. Hence we choose these types of NCs for further investigation on the Si solar cells.

5.3.4 Spectral response analysis of NCs coated Si solar cell

The operation [68] of NCs on the Si solar cell is following. Firstly, the incident UV photons are strongly absorbed by the NCs, generating electron-hole pairs in the NCs. These photogenerated carriers then relax to lower energy states (e.g. through photon interactions) and recombine radiatively at lower photon energy with high quantum efficiency. Most of these photons are then emitted at longer wavelengths (by the NCs) where Si is most efficient to absorb these emitted photons those are not absorb by the NCs themselves and thus arrive at the front surface of Si solar cell platform. As a result, these photons are then strongly absorbed by the Si solar cell to contribute to the solar energy conversion. Therefore, the deposited NCs on the Si solar cell allows the incident UV photons effectively to be converted to visible photons (down shifting of energy) to generate electrical energy at the Si solar cell where UV photons were unused.

In the measurement of device performance, the enhancement of photocurrent arises due to the absorption and emission properties of the doped NCs. The incident UV light which cannot be used for wavelengths bellow 350 nm directly by the Si solar cell, is converted to the visible light (at the emission wavelength of the NCs around 592 nm), which is much useful for the Si solar cell. We consider the enhancement of solar cell performance is due to only the emission of ZnS due to Mn doping.

In our experiments we used few drops of the aqueous solution of NCs on cells. Before using the NCs on the device surface we diluted the freshly prepared NCs solution by water maintained the

concentration of 10% (by volume). So after drying air it is expected few spots with high density of NCs on the cell's surface. The spectral response curve of Mn doped ZnS NCs coated Si solar cell is shown in Figure 5.18. From this diagram it is clearly observed that there is a slight decrease of EQE bellow 350 nm and a strong decrease of EQE throughout the visible to IR region. Loss of EQE bellow 350 nm is regarding the luminescence quenching effect due to high concentration of NCs on the cell surface. This quenching effect can arise due to the interaction of organic ligand (mercapto ethanol which is surrounded on the NCs as shown in Figure 5.13) and NCs. In literature [51], there is same kind of decrease of EQE observed in UV region due to concentration quenching effects of Eu^{3+} complexes used in same type of solar cells. Also decrease of EQE in visible to IR region could be due to transmission losses by the ME capped NCs and the transmission losses is expected due to the spots with high density of NCs. Further investigations of EQE of the cell with decreasing the concentration of NCs are needed.

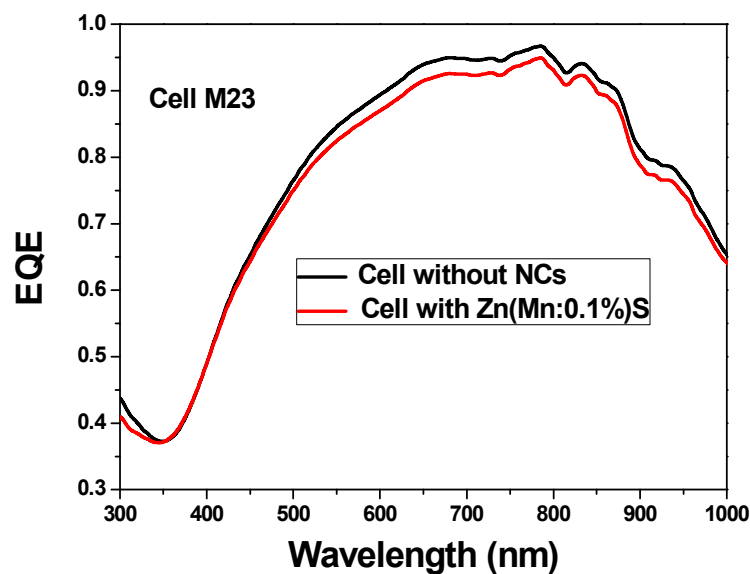


Figure 5.18: Spectral response of cell uncoated and coated with concentrated NCs. We measured the ten spectral responses on different positions on whole cell surface before and after deposition of NCs.

The spectral response curve of cell with lower concentration (half of the initial concentration i.e. 5%) of NCs is depicted in Figure 5.19-a. It is ascribed that there is increase of EQE in below 350nm which is our region of interest. There is also additional improvement of EQE in the red region shown in Figure 5.19-a. Maximum relative enhancement of EQE is plotted in Figure 5.19-b. The maximum enhancement ascribed bellow 400 nm where the maximum of UV light absorption by NCs is observed and these NCs emit yellow orange light at 592 where Si solar cell has better

spectral response. Also some cell shows a small EQE enhancement also in IR region depicted in Figure 5.20. This could be due to the experimental error in this region. Lowering the concentration of NCs might be acting as an additional antireflection coating on standard Si solar cell. This might be due to increased surface roughness of cell surface after integrating doped ZnS NCs [99]. Therefore, enhancement of EQE in both UV and longer wavelength (close to the band gap of Si) region attributes better light trapping into Si cell possible by doped ZnS NCs.

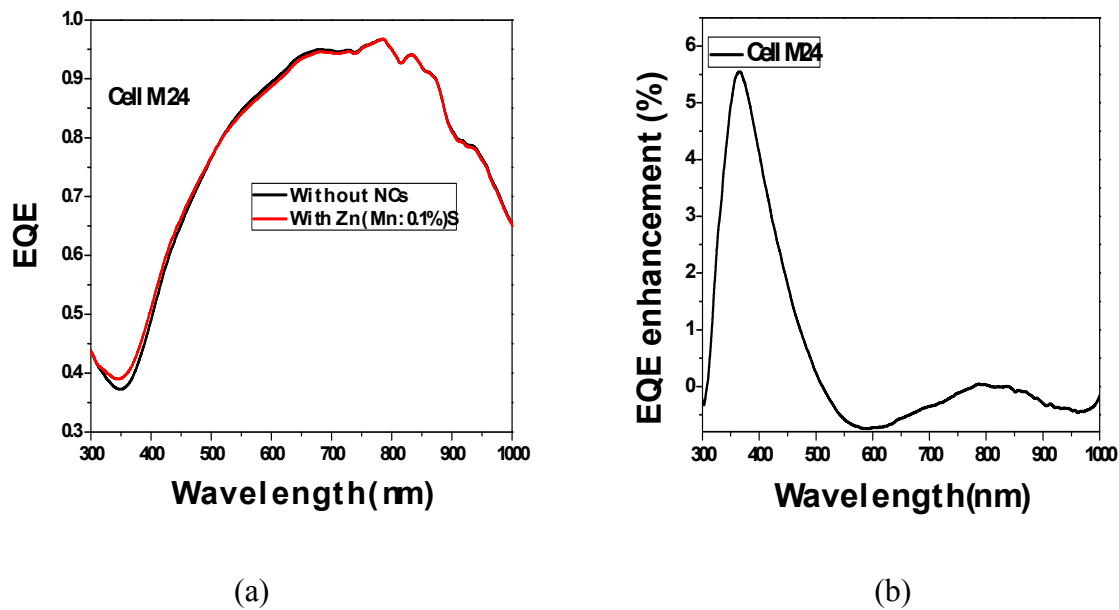


Figure 5.19: (a) spectral response of cell coated with lower concentration of NCs (b) enhancement of EQE of the same cell (For each sample, at least ten EQE measurements were performed by varying the spot position on the front surface of the cell. The value of the measurement error is 1.25% in the range between 300 and 450nm and this value is lower than the maximum enhancement obtained in this region.)

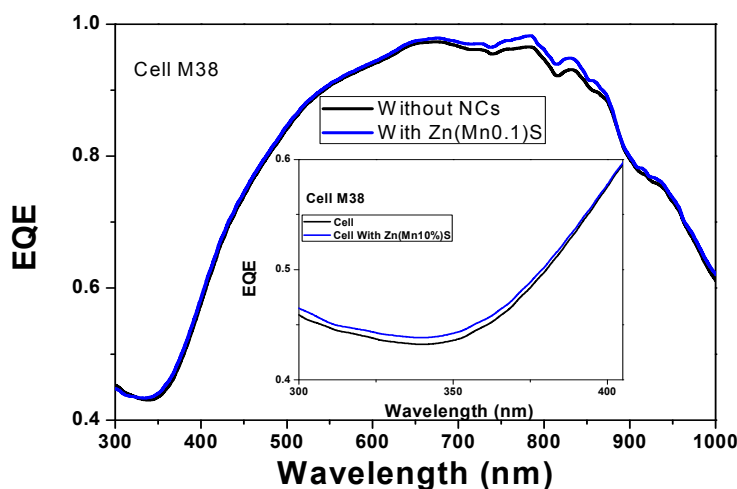


Figure 5.20: Enhancement of EQE in both UV and near IR region due to lower concentration of NCs

5.3.5 I-V measurements of NCs coated Si solar cell

The I-V measurement of different cells is shown in Table 5.1 bellow. Maximum relative enhancement of P_{max} is 1.2%. Different cells show different results. It might be due to problem of controlling the NCs distribution on cell surfaces by putting some drops of aqueous solution.

Table 5.1: I-V measurements of different cells coated with Zn(Mn:10%)S NCs

Sample M24						
	Efficiency		Relative Enhancement (%)	Max delivered power (P_{max})		Relative Enhancement (%)
	Without NCs	With NCs		Without NCs	With NCs	
Mean	13	13.2	1.5±0.3	117.5	118.8	1.2±0.3
Sample M38						
	Efficiency		Relative Enhancement (%)	Max delivered power (P_{max})		Relative Enhancement (%)
	Without NCs	With NCs		Without NCs	With NCs	
Mean	12.6	12.7	0.8±0.3	113.6	114.2	0.6±0.3

After some preliminary investigation, it is clearly attributed that there is enhancement even if small (from both spectral response and I-V measurements) of solar cell performance due to the Mn doped ZnS NCs on top of the Si solar cell. It is better implication to obtain better performance of Si solar cell coated with NCs doped inside the polymeric matrix. Also it is expected of homogeneous distribution of NCs in polymeric matrix. For these purpose the chosen materials were indeed many, with the most frequent categories being polymers are PMMA, or Poly-Vinyl Acetate (PVA) and copolymers like EVA [51, 100]. We have used polymer PMMA and copolymer EVA which are mostly use for the realization of Si solar cell module. But EVA is mostly used for commercial Si solar cell module fabrication [51]. Henceforth Si solar cell coated with EVA doped NCs could be an additional benefits for commercial application.

Before starting any experimental measurements on Si solar cell with NCs-polymer film, we tested the spectral response measurements on the Si solar cell coated with pure PMMA film prepared by spin coating.

5.3.6 Spectral response analysis of Si solar cell with pure PMMA film on top

Spectral response were done on PMMA coated Si solar cell in order to analyse the clear effect of it. We tested various thickness of PMMA on the cell.

Spectral response of PMMA coated Si solar cell is shown in Figure 5.21. It ascribed that there is large enhancement EQE between 300 nm to 550 nm whereas there is slight decrease of EQE between 550 to 900 nm.

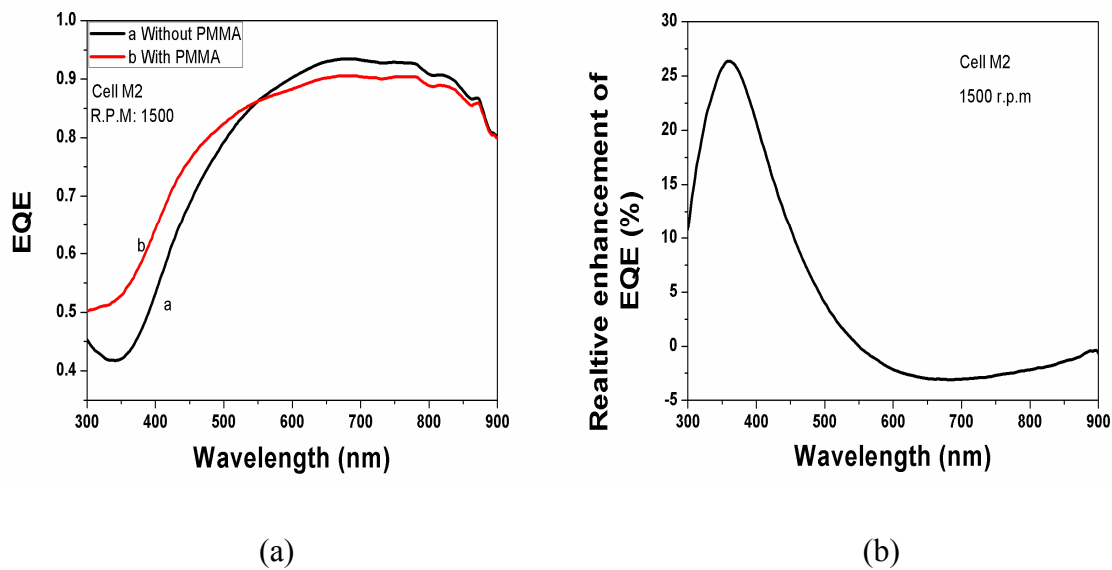


Figure 5.21: (a) Spectral response of PMMA (one layer) coated laboratory based standard Si solar cell (b) Relative enhancement of EQE of same cell coated with PMMA

Transmittance of plots of different layers of PMMA on quartz substrate is shown in Figure 5.22. From the transmittance plot it is clear that there is increase of transmittance (decrease of reflectance) on the cell surface due to 1 layer PMMA coating. Also multilayer deposition (same concentration of PMMA and same r.p.m used for spin coating) was tested on the same sample in order to investigate the thickness effect. In Figure 5.22, it is confirmed that transmittance reaches maximum with increasing thickness of PMMA layer. In our experiment two layer of PMMA shows maximum transmittance (minimum reflectance). Also relative enhancement of EQE reaches maximum due to two layer PMMA coating as shown in Figure 5.23.

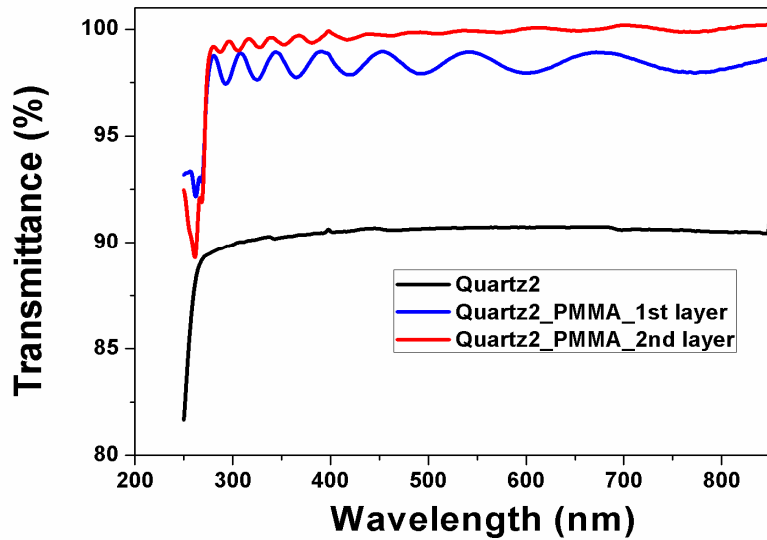


Figure 5.22: Transmittance plot of multilayer PMMA on quartz substrate

From the transmittance measurement of Figure 5.22, there is no indication about the variation of transmittance (variation of reflectance) in different wavelength. But Figure 5.21 shows some decrease of EQE from 550 nm to 900 nm. It could be due to inhomogeneous thickness of PMMA film on the cell surface.

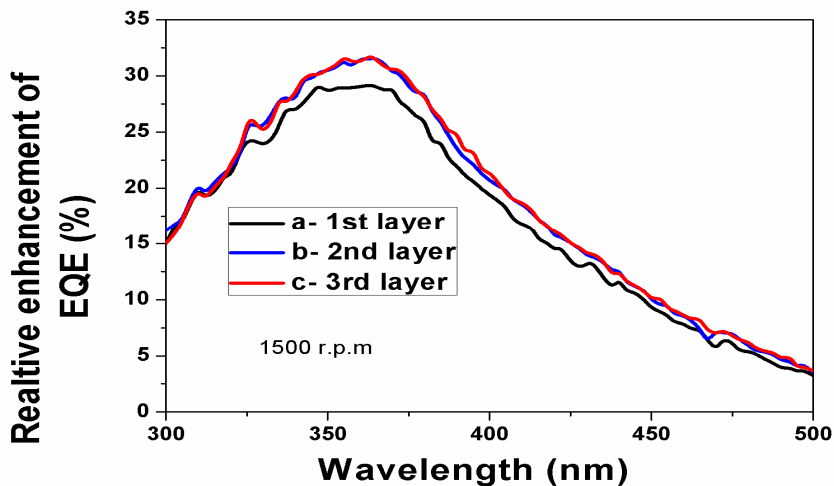


Figure 5.23: Relative enhancement of EQE with increasing number of PMMA layer

5.3.7 Spectral response of Si solar cell with NCs doped PMMA and EVA film on top

Before experimental observation on the effect of NCs, spectral response of same Si solar cell with top of quartz substrate coated both with pure PMMA and EVA was studied (structure is the same as

depicted in Figure 5.3). It should be remarked that the concentration of both PMMA and EVA was used as 1.5% (wt). The spectral response of these two is shown in Figure 5.24 and Figure 5.25.

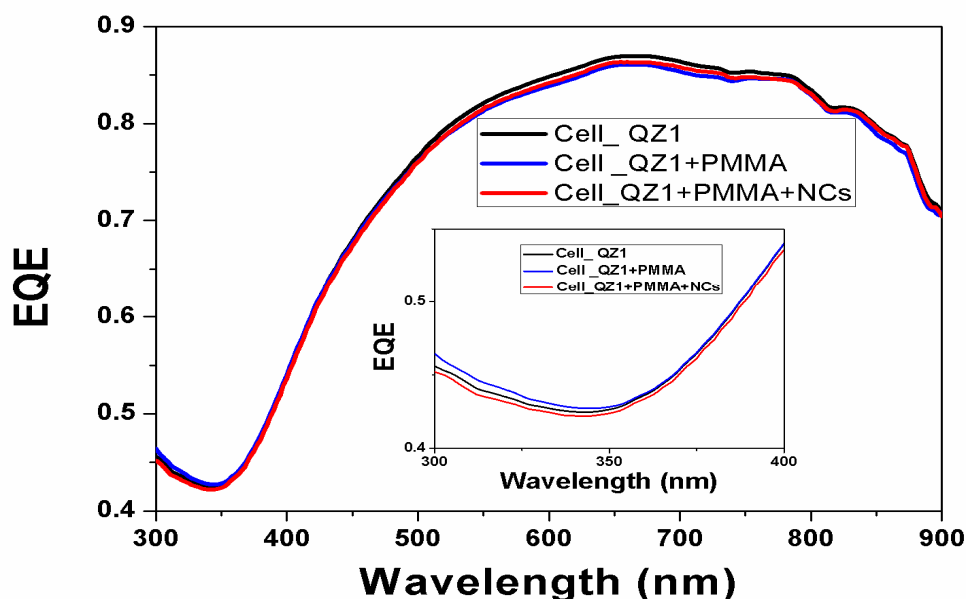


Figure 5.24: Spectral response of NCs doped and undoped PMMA film on Si solar cell (inset Figure shown for clear observation)

There is increase of EQE in UV region (inset of Figure 5.24) as well as decrease of EQE in visible to IR region observed is due to pure PMMA on Si solar cells. Further investigation of PMMA on Si solar cell will be described later. But NCs doped PMMA film on Si solar cell shows some decrease of EQE below 350 nm as shown in Figure 5.24. However there is no change of EQE at visible region of the same cell coated with NCs doped PMMA. Also slight decrease of EQE in UV region is observed due to EVA on cell surface (as inset Figure 5.25). This decrease below 350 nm is associated with the UV light absorption by the EVA film. Furthermore a strong decrease of EQE is observed below 350 nm for NCs doped EVA film on the cell as depicted in Figure 5.25. The decrease of EQE due to NCs doped both with PMMA and EVA is observed. The concentration of powder NCs used in both PMMA and EVA solution is 0.26% (mg/ml). It is expected that, there is some agglomeration of NCs in powder form. The decrease of EQE in UV region might be due to agglomerated NCs which can act as luminescence quencher on the cell surface. During preparation of NCs- polymer solution, it was observed that there is a dissipation of NCs in solvent. That's why it is difficult to suspend all the NCs homogeneously both in PMMA and EVA. For better suspension of NCs in solvent for some time, it is required of high ultrasonication. That's why few NCs could be expected on substrate.

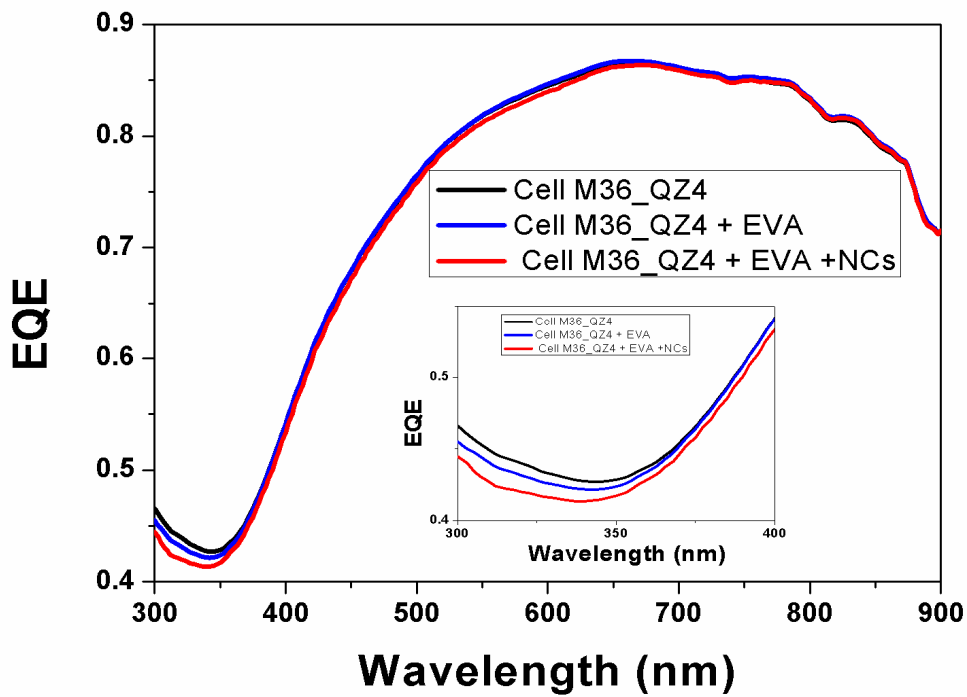


Figure 5.25: Spectral response of NCs doped EVA film on Si solar cell

The key point for preparing high performance NCs-polymer hybrids is how to produce good PL materials, along with excellent transparency (transmittance~100%). So, direct polymerization of aqueous NCs via free radical polymerization [8] could be better way to enhance optical performance of NCs.

Chapter 6

Conclusion, Critical Issues and Future Work

Two light harvesting methods have been studied in the thesis. A summary of the results of each method are described separately in the following.

Surface Plasmon technique

Before starting discussion of critical points it should be clear the various parameters that can affect the light harvesting method by surface plasmon technique. These are (i) choice of metal NPs (ii) sizes and shapes of NPs (iii) distribution of NPs on substrate (iv) position of metal NPs with respect to the active device surface (v) oxidation of metal NPs. Two main basic mechanisms have been proposed to explain photocurrent enhancement by metal particles incorporated into or on solar cell: near field concentration and light scattering. We are mostly concentrated on light scattering effect due to the size of the particles prepared by the reported synthesis procedure.

The effect of PLS due to metal NPs (both silver and gold) on both Si and CIGS thin film solar cell has been studied. PLS related to such colloidal synthesized NPs has been studied as a result improving the efficiency of mc-Si solar cells both with (ARC) and without ARC (NOARC). Since silver is the best choice for light scattering among other metal NPs, we tried different process for silver NPs synthesis. We controlled the particle size using surfactant and also distribution of the particle on the substrate. First of all, silver NPs synthesized using SDS surfactant did not induce a spectral response enhancement on Si solar cell. The best results were obtained instead for silver NPs coated embedded in PDDA. However, it was difficult to control the particle size in PDDA and the distribution of particles on substrate by dip coating or putting some drops on the substrates. The effect of PLS (due to silver NPs) on SR has been reported, showing EQE enhancements both in visible to near-infrared range and confirming that light can couple more efficiently into NOARC cell than ARC cell. The same EQE enhancement due to both NPs was observed also in the case of CIGS cells, the results being consistent with those obtained for Si cells. Although we know silver is best choice in the PLS process among the other metal NPs due to its higher scattering efficiency, the possible oxidation of silver NPs could affect the enhancement of PV properties. Since we have no experimental evidences to support such hypothesis on the oxidation effect, we repeated the same experiments with noble metal NPs like gold and compared them with silver NPs results obtained. Therefore we synthesized gold NPs by colloidal method followed by the deposition of such colloidal NPs on both MC-Si cells and CIGS cells. EQE enhancement observed on both Si and CIGS cells due to gold NPs is close to the enhancement due to silver NPs, even if silver showed the best scattering efficiency. So most probably some oxidation of silver NPs occurs and thus limiting the EQE enhancement on both Si & CIGS cells coated with them. It should therefore be concluded

that EQE enhancement can be further improved by the silver NPs prepared in inert atmosphere and possibly submitted to encapsulation.

All that considered, the possible ways for further enhancements of device performance due to colloidal metal NPs are still open. Firstly, varying the size and shapes of NPs using another surfactant might be a way to investigate the better device performance. It will be a superior implication to design a solar cell module fabricated with a thin polymeric matrix doped with such NPs. Also it is expected of homogeneous distribution of NPs inside the polymeric matrix. For these purpose the chosen materials were indeed many, with the most frequent categories being polymers are PMMA, or Poly-Vinyl Acetate (PVA) and copolymers like EVA which is mostly used for commercial Si solar cell module fabrication. Therefore Si solar cell coated with EVA doped NPs could be an additional benefits for commercial application. It should be a critical issue to find a proper solvent system for synthesis of NPs also to dissolve the NPs inside the polymeric matrix. Also concentration of NPs inside the polymeric film might play an important role for light scattering. Future works will also be devoted to the application of such procedure to silicon based thin film solar cells.

Down- shifting by semiconductor NCs

We have studied the down shifting concept by the NCs on Si solar cell. There are many highly luminescent NCs commercially available. Many of them are CdSe, CdSe-ZnS core shell which are toxic and hazardous. So it will be more safety to find a nontoxic material which can be easily handled. That's why we used ZnS NCs as a non toxic material.

We reported first time demonstration of Mn doped ZnS NCs integrated on Si solar cells for the enhancement of photovoltaic parameters including EQE, solar conversion efficiency and maximum delivered power. For this we successfully synthesized ME (organic ligand) capped ZnS NCs with various doping concentration of Mn. We also observed the band gap variation of NCs and enhancement of PL intensity with optimum doping concentration of Mn. We investigated the concentration (NCs) dependent improvement of EQE in UV region where Si cells has poor spectral response. Higher concentration of NCs shows a luminescence quenching effect on Si solar cell. So there is a decrease of EQE in same UV region observed. To obtain the superior device performance it is mandatory to obtain high quality NCs with high intense visible emission (preferentially red wavelength region), optically highly transmittance and homogeneous distribution on the device surface. The NCs were deposited by putting some drops on the cells; therefore it is difficult to maintain homogeneous distribution of the NCs on Si solar cells. Since ME capped NCs are not fully

dispersed in the aqueous solvent, it is also required high ultrasonication to obtain highly dispersion of NCs into the solvent. There is another critical issue that presently we don't have any information about the removal of capping ligand. We also tried to fabricate NCs (powder) doped polymer layer on the cells. But we faced the same problem with dispersion of the NCs in different organic solvent those were used for the preparation polymer-NCs composite. Therefore it was difficult to obtain a high quality NCs-polymer film on the substrates. NCs concentration (inside polymeric film) dependent SR improvement in UV region needs to be further investigation.

Henceforth it will be the best way to functionalize the aqueous ZnS NCs and fabrication NCs-polymer nanocomposite hybrids via free radical polymerization in situ. In this case, there should not problem with dispersion of NCs in the solvent. Also synthesis of these NCs with different capping ligand will be another opportunity to obtain further high quality NCs. Finally it should be better to find an estimation of the cost for the c-Si solar cell module encapsulation with EVA doped layer for commercial purpose.

We believe that, also in this case the enhancement can be further improved by homogeneous distribution of NCs on the device surface. So this approach seems very promising for first generation photovoltaic devices will be devoted in future work.

References

- [1] "Basic research needs for solar energy utilization," Report of the BASIC Energy Sciences Workshop on Solar Energy Utilization, Ed. by N.S. Lewis, G.W. Crabtree (US Department of Energy Office of Basic Energy Sciences, (2005)
- [2] "Handbook of Photovoltaic Science and Engineering", Ed. by Antonio Luque & Steven Hegedus, John Wiley & Sons Ltd (2003)
- [3] G. W. Crabtree and N. S. Lewis, *Solar Energy Conversion*, Physics Today, Vol. 60: 7, (2007)
- [4] T. Key, "Solar photovoltaics: Expanding electric generation options", A technical report, Electric Power Research Institute, (2007)
- [5] S. O'Rourke, P. Kim, and H. Polavarapu. *Solar photovoltaics, technology and economics: thin films and crystalline silicon. Technical report*, Deutsche Bank, (2007)
- [6] E. K. Brown and C. Jigarjian. *Alternative energy: coverage initiated on the solar PV industry. Technical report*, Bank of America, (2007)
- [7] W. Shockley and H. J. Queisser, Journal of Applied Physics, Vol. 32(3): 510, (1961)
- [8] G. B. Haxel, J. B. Hedrick, and G. J. Orris. *Rare earth elements - critical resources for high technology: US Geological Survey fact sheet 087-02*. Technical report, US Geological Survey, (2002)
- [9] M. A. Green, K. Emery, Y. Hishikawa, and W. Warta, Progress in Photovoltaics: Research and Applications, Vol. 16(5): 435, (2008)
- [10] R. M. Swanson, Conference record of the Thirty-first IEEE Photovoltaic Specialists Conference, Vol. 1: 889, (2005)
- [11] T. Markvart, *Solar Electricity*, Second Edition, John Wiley & Sons, (2000)
- [12] M. A. Green. Solar Energy, Vol. 76: 3, (2004)
- [13] A .V. Shah, H. Schade, M. Vanecek, J. Meier, E. Vallat-Sauvain, N. Wyrsh, U. Kroll, C. Droz and J. Bailat, Progress in Photovoltaics: Reserch and Applications, Vol. 12: 113, (2004)
- [14] M. A. Green, K. Emery, Y. Hishikawa, and W. Warta, Progress in Photovoltaics: Reserch and Applications, Vol. 16: 61, (2008)
- [15] *Reported timeline of solar cell energy conversion efficiencies* (from National Renewable Energy Laboratory (USA), March (2011)
- [16] Peter Brenner, *Metalization Solutions for C-Si Next Solution Technology*, 25 EU PVSEC, (2010)
- [17] M. A. Green, Physica E: Low-dimensional Systems and Nanostructures, Vol. 14: 65, (2002)

- [18] Photovoltaics World, Vol. 2010, Issue 6, (2010)
- [19] L. Tsakalakos, Material Science and Engineering R, Vol. 62: 175, (2008)
- [20] R. R. King, D.C. Law, K.M. Edmondson, C. M. Fetzer, G. S. Kinsey, H. Yoon, R. A. Sheri, and N. H. Karam, Appl. Phys. Lett., Vol. 90: 183516, (2007)
- [21] W. Wang, A. S. Lin, and J. D. Phillips, Appl. Phys. Lett., Vol. 95: 011103, (2009)
- [22] M. A. Green, *Third Generation Photovoltaics: Advanced Solar Energy Conversion*, Springer series in Photonics, Vol. 12, (2003)
- [23] Tomas Markvart, *Solar Electricity*, Second Edition, John Wiley & Sons, 2000
- [24] S.Pillai, K. R. Catchpole, T. Trupke, and M.A.Green, Journal of Applied Physics, Vol. 101: 093105, (2007)
- [25] C. Strumpel, M. M. Cann, G. Beaucarne, V. Arkhipov, A. Slaoui, V. Svrcek, C. Canzio, and I. Tobias, Solar Energy Materials and Solar Cells, Vol. 91: 238, (2007)
- [26] M. C. Beard and R. J. Ellingson, Laser & Photon. Rev., Vol. 2(5): 377, (2008)
- [27] D. M. Schaadt, B. Feng, and E. T. Yu, Applied Physics Letters, Vol. 86: 063106, (2005)
- [28] D. Derkacs, S. H. Lim, P. Mathieu, and E. T. Yu, Applied Physics Letters, Vol. 89: 093103, (2006)
- [29] S. Pillai, K. R. Catchpole, T. Trupke, G. Zhang, J. Zhao, and M. A. Green, Applied Physics Letters, Vol. 88: 161102, (2006)
- [30] W. Yanshuo, C. Nuofu, Z. Xingwang, Y. Xiaoli, B. Yiming, C. Min, W. Yu, C. Xiaofeng, and H. Tianmao, Journal of Semiconductors, Vol. 30 (7): 072005, (2009)
- [31] K. R. Catchpole and A. Polman, Optics Express, Vol. 16(26): 21793, (2008)
- [32] K. R. Catchpole and A. Polman, Applied Physics Letters, Vol. 93: 191113 (2008)
- [33] H. R. Stuart and D.G. Hall, Applied Physics Letters, Vol. 73(26): 3815, (1998)
- [34] S. Pillai and M. A. Green, Solar Energy Materials & Solar Cells Vol. 94: 1481, (2010)
- [35] M. Kirkengen, J. Bergli, and Y. M. Galperin, Journal of Applied Physics, Vol. 102: 093713, (2007)
- [36] H. R. Stuart and D. G. Hall, Applied Physics Letters, Vol. 69 (16): 2327, (1996)
- [37] H. R. Stuart and D. G. Hall, Applied Physics Letters, Vol. 73 (26): 3815, (1998)
- [38] K. R. Catchpole and A. Polman, Applied Physics Letters, Vol. 93: 191113, (2008)
- [39] R. G. Grainger, J. Lucas, G. E.Thomas, and G. B. L. Ewen, Applied Optics 43 (28): 5386, (2004)
- [40] Y. Xia, G. Gu, , Z. Hu, Y. Guo, X. Fu, and J. Song, MRS Bulletin, Vol. 30: 338, (2005)
- [41] T. Trupke and M. A. Green, Journal of Applied Physics, Vol. 92 (3): 1668, (2002)

- [42] A. Goetzberger and W. Gruebel, *Appl. Phys.* Vol. 14 (2): 123, (1977)
- [43] P.S. Friedman and C.R. Parent, *Luminescent Solar Concentrator Development Final Report*, SERI subcontract no. XE-2-02145-01, 193, (1987)
- [44] B.S. Richards, A. Shalav, and R.P. Corkish, 19th European Conference on Photovoltaic and Solar Energy Conversion, Paris, 113, (2004)
- [45] T. Maruyama, A. Enomoto, and K. Shirasawa, *Solar Energy Materials & Solar Cells*, Vol. 64: 269, (2000)
- [46] B.S. Richards, *Solar Energy Materials & Solar Cells*, Vol. 90: 1189, (2006)
- [47] R.G. Curry, W.P. Gillin, *Appl. Phys. Lett.*, Vol. 77: 2271, (2000)
- [48] Y. Kawamura, Y. Wada, and S. Yanagida, *Jpn. J. Appl. Phys.*, Vol. 40: 350, (2001)
- [49] S. Marchionna, F. Meinardi, M. Acciarri, S. Binetti, A. Papagni, S. Pizzini, V. Malatesta, and R. Tubino, *Journal of Luminescence*, Vol. 118: 325, (2006)
- [50] K. R. McIntosh, G. Lau, J. N. Cotsell, K. Hanton, D.L. Batzner, F. Bettiol, and B.S. Richards, *Progress in Photovoltaic: Research Application*, Vol. 17:191, (2009)
- [51] A. L. Donne, M. Acciarri, D. Narducci, S. Marchionna and S. Binetti, *Prog. Photovolt: Res. Appl.* Vol. 17: 519, (2009)
- [52] A. L. Donne, M. Dilda, M. Crippa, M. Acciarri and S. Binetti, *Optical Materials* Vol. 33: 1012, (2011)
- [53] M. F. Joubert, *Opt. Mater.* Vol. 11: 181, (1999)
- [54] T. Trupke and M. A. Green, *Journal of Applied Physics*, Vol. 92(7): 4117, (2002)
- [55] T. Trupke, A. Shalav, B.S. Richards, P. Würfel, and M.A. Green, *Solar Energy Materials & Solar Cells* Vol. 90: 3327, (2006)
- [56] M. C. Hanna and A. J. Nozik, *J. Appl. Phys.* Vol. 100: 074510, (2006)
- [57] Center for advance solar photo physics, <http://casp.lanl.gov/science.shtml>.
- [58] M. Nirmal, B. O. Dabbousi, M. G. Bawendi, J. J. Macklin, J. K. Trautman, T. D. Harris, and L. E. Brus, *Nature* , Vol. 383: 802, (1996)
- [59] A. L. Efros and M. Rosen, *Phys. Rev. Lett.*, Vol.78: 1110, (1997)
- [60] A. J. Nozik, *Physica E* Vol 14: 115, (2002)
- [61] R. Schaller and V. Klimov, *Phys. Rev. Lett.*, Vol. 92: 186601, (2004)
- [62] R. J. Ellingson, M. C. Beard, J. C. Johnson, P. Yu, O. I. Micic, A. J. Nozik, A. Shabaev, and A. L. Efros, *Nano Lett.*, Vol. 5: 865, (2005)
- [63] J. E. Murphy, M. C. Beard, A. G. Norman, S. P. Ahrenkiel, J. C. Johnson, P. Yu, O. I. Micic, R. J. Ellingson, and A. J. Nozik, *J. Am. Chem. Soc.*, Vol. 128: 3241, (2006)
- [64] R. D. Schaller, M. Sykora, J. M. Pietryga, and V. I. Klimov, *Nano Lett.*, Vol. 6: 424, (2006)

- [65] W. G. J. H. M. Van Sark, A. Meijerink, R. E.I. Schropp, J.A.M. van Roosmalen, and E. H. Lysen, *Solar Energy Materials & Solar Cells*, Vol. 87: 395, (2005)
- [66] T. Maruyama and J. Bandai, *Journal Electrochem. Soc.*, Vol. 146: 4406, (1999)
- [67] J. Lee, V.C. Sundar, J.R. Heine, M.G. Bawendi, K.F. Jensen, *Adv. Mater.*, Vol.12: 1102 (2000)
- [68] E. Mutlugun, I. M. Soganci, and H. V. Demir, *Optics Express*, Vol. 16 (6): 3537, (2008)
- [69] J. Zhang, X. Li, K. Liu, Z. Cui, G. Zhang, B. Zhao, and B. Yang, *Journal of Colloid and Interface Science*, Vol. 255: 115, (2002)
- [70] F. J. Beck, A. Polman, and K. R. Catchpole, *Journal of Applied Physics*, Vol. 105: 114310, (2009)
- [71] X. Hu and Shaojun Dong, *Journal of Materials Chemistry*, Vol. 18: 1279, (2008)
- [72] C. Burda, X. Chen, and R. Narayanan, M. A. El-Sayed, *Chem. Rev.*, Vol 105: 1025, (2005)
- [73] L. M. L. Marzán, *Langmuir*, Vol. 22 : 32, (2006)
- [74] <http://www.elmhurst.edu/~chm/vchembook/558micelle.html>
- [75] P. C. Lee and D. Meisel, *Journal of Physical Chemistry*, Vol. 86: 3391, (1982)
- [76] A. Herguth, G. Schubert, M. Kaes, and G. Hahn, *Prog. Photovolt: Res. Appl.* Vol. 16: 135, (2008)
- [77] S. Sterk, K. Munzer, and S. Glunz, 14th European PVSEC Proceeding, Barcelona: 85, (1997)
- [78] K. C. Song, S. M. Lee, T. S. Park, and B. S. Lee, *Korean J. Chem. Eng.*, Vol. 26(1): 153, (2009)
- [79] A. B. R. Mayer, S. H. Hausner, and J. E. Mark, *Polymer Journal*, Vol. 32(1): 15, (2000)
- [80] K. H. Su, Q. H. Wei, X. Zhang J. J Mock, D. R Smith, and S. Schultz, *Nano Letters*, Vol. 8 (3): 1087, (2003)
- [81] B. J. Soller and D. G. Hall, *J. Opt. Soc. Am. A*, Vol. 18(10): 2577, (2001)
- [82] Yu Lu, Gang L. Liu and Luke P. Lee, *Nano Letters*, Vol. 5: 5, (2005)
- [83] K. Ramanathan, M. A. Contreas, C. L. Perkins, S. Asher, F. S. Hasoon, J. Keane, D. Young, M. Romero, W. Metzger, R. Noufi, J. Ward, and A. Duda, *Prog. Photovolt: Res. Appl.*, Vol. 11: 225, (2003)

- [84] M. Acciarri, A. Le Donne, M. Morgano, L. Caccamo, L. Miglio, S. Marchionna, R. Moneta, M. Meschia & S. Binetti, *Energy procedia* (in press), (2011)
- [85] J. Cao, J. Yang, Y. Zhang, L. Yang, Y. Wang, M. Wei, Y. Liu, M. Gao, X. Liu, and Z. Xie, *Journal of Alloys and Compounds*, Vol. 486: 890, (2009)
- [86] A. A. Green and M.C. Hersam, *Nano Lett.*, Vol. 8: 1417, (2008)
- [87] Z. Wang, L. Daemen, Y. Zhao, and C.S. Zha, *Nat. Mater.*, Vol. 4: 922, (2005)
- [88] K. Manzoor, S. R. Vadera, T. R. N. Kutty and N. Kumar, *Materials Chemistry and Physics*, Vol. 82: 718, (2003)
- [89] S. Sapra, A. Prakash, A. Ghangrekar, N. Periasamy, and D. D. Sarma, *J. Phys. Chem. B*, Vol. 109: 1663, (2005)
- [90] C. W. Malm, J.O. Zwiller, V. Wallenberg, and R. Bovin, *J. Appl. Phys.*, Vol. 8: 2671, (2001)
- [91] H. Chander, *Proc. of ASID*, 8-12 Oct (2006), New Delhi
- [92] L. Guo, S. Chen and L. Chen, *Colloid Polym Sci*, Vol. 285: 1593, (2007)
- [93] S. Senthilkumar, K. Rajendran, S. Banerjee, T. K. Chini and V. Sengodan, *Materials Science in Semiconductor Processing*, Vol. 11: 6, (2008)
- [94] S. V. Bhat and F.L. Deepak, *Solid State Communication*, Vol. 135: 345, (2005)
- [95] T. T. Q. Hoa, N. D. The, S. M. Vitie, N. H. Nam, L. V. Vu, T. D. Canh and N. N. Long, *Optical Materials*, Vol. 33: 308, (2011)
- [96] R. Sarkar, C. S. Tiwary, P. Kumbhakar, S. Basu, and A. K. Mitra, *Physica E*, Vol. 40: 3115, (2008)
- [97] K. Manzoor, S. R. Vadera, N. Kumar, and T. R. N. Kutty, *Materials Chemistry and Physics*, Vol. 82: 718, (2003)
- [98] H. Chander, *Materials Science and Engineering R*, Vol. 49: 113, (2005)
- [99] C. Y. Huang, D.Y. Wang, C. H. Wang, Y. T. Chen, Y. T. Wang, Y. T. Jiang, Y.J. Yang, C. C. Chen, and Y. F. Chen, *ACS NANO*, Vol. 4 (10): 5849, (2010)
- [100] E. Klampaftis, D. Ross, K. R. McIntosh, and B. S. Richards, *Solar Energy Materials & Solar Cells*, Vol. 93: 1182, (2009)

List of publications:

(i) Sourav Kanti Jana, Alessia Le Donne, and Simona Binetti, Journal Physics and Chemistry of Solids (2011) in press